Concept Demonstrator for MeerKAT Operation from 14.5 to 20 GHz

Sitwala Mundia

Supervisor: Prof. Riana Geschke

Faculty of Engineering and the Built Environment
University of Cape Town

This dissertation is submitted for the degree of
Master of Science (Engineering)

Department of Electrical Engineering May 2019

I would like to dedicate this dissertation to my amazing siblings: Mushaukwa, Mutumboi, Mwiya and Inonge.

Declaration

I know the meaning of plagiarism and declare that all the work in the document, save for that which is properly acknowledged, is my own. This thesis/dissertation has been submitted to the Turnitin module (or equivalent similarity and originality checking software) and I confirm that my supervisor has seen my report and any concerns revealed by such have been resolved with my supervisor.

Signature: ..... Signed by candidate

Sitwala Mundia
February 2019

Acknowledgements

- I wish to thank Prof Riana Geschke, my supervisor, for her invaluable support and guidance during my research. You set high standards I will aspire to on my path to becoming a researcher.
- Sias Malan, my co-supervisor, thank you for the mentorship and support during the research. Having an industry advisor for my research was very beneficial.
- I wish to thank Rishad Ebrahim and Luyanda Boyana from SARAO for the support during the project. Rishad, thank you for the assistance during system measurements. Luyanda, thank you for the mechanical design support for the project.
- Thank you to Anneke Bester from Stellenbosch University for assistance with antenna measurements.
- Thank you to my good friend Ngoy Mutonkole for introducing me to the SKA project and all the general advice on the antenna modelling and simulation.
- Thank you to Tauriq Latief for the excellent work done on the image reject filter design for his final year project. The receiver wouldn't be complete without the filter.
- I wish to thank my family and my partner, Shiba for all the support during my studies. Your support and encouragement kept me going.
- I acknowledge the Centre for High Performance Computing (CHPC) for use of the Lengau cluster for electromagnetic simulations.
- This research was supported by the South African Radio Astronomy Observatory, which is a facility of the National Research Foundation, an agency of the Department of Science and Technology

Abstract

In this thesis, a proof of concept receiver system operating from 14.5 to 20 GHz for the MeerKAT Radio Telescope is presented. MeerKAT is a 64 element telescope antenna array consisting of offset-fed Gregorian reflector antennas with a 13.5 m main reflector and 3.8 m sub-reflector. Currently, the MeerKAT is planned to operate up to 14.5 GHz. However, the reflector surface accuracy of 0.6 mm RMS achieved for the MeerKAT potentially allows it to operate at much higher frequencies.

The system design consists of a feed horn antenna and front-end down conversion receiver ready for integration with back-end digital signal processing. The antenna design was carried out using electromagnetic simulation software and system level simulation software was used for the front-end receiver. A single polarization wide-axially corrugated horn with low side-lobes and cross-polarization has been designed for the proof of concept with a predicted aperture efficiency of 60% including surface accuracy loss when illuminating the MeerKAT reflector. The measured results for the antenna show a return loss better than 15 dB in the operational band and boresight gain of 12 dB. The measured E- and H-plane cross-polarization for the antenna is lower than -40 dB. The measured edge taper at the half-subtended angle of the sub-reflector is between -11.8 dB and -13.2 dB.

The front-end receiver was designed to use a single down-conversion stage to a 4.5 GHz IF with an instantaneous bandwidth of 2.5 GHz to be bandpass sampled at 6 Giga-samples per second (GSPS). The receiver was designed using off-the-shelf connectorized modules and custom designed microstrip filters for image rejection and anti-aliasing. Laboratory measurements of the receiver show a maximum gain of 76 dB, 40 dB image rejection and 27 dB spurious free dynamic range (SFDR). The simulated noise figure of the system using the measured noise figure of the LNA is 1.74 dB. The measured gain flatness of the receiver is $\pm$7 dB due to poor performance of one of the amplifier modules used in the system.

Table of contents

List of figures

List of tables

List of Acronyms

ADC	Analog to Digital Converter
ATA	Allen Telescope Array
AUT	Antenna Under Test
AUT	Device Under Test
AVN	African Very Long Base Line Interferometry
CMB	Cosmic Microwave Background
CNC	Computer Numerical Control
CO	Co-Polarization
CSIRO	The Commonwealth Scientific and Industrial Research Organisation
EM	ElectroMagnetics
HPBW	Half-Power Beamwidth
IF	Intermediate Frequency
LNA	Low Noise Amplifier
LO	Local Oscillator
MOM	Methods of Moments
NF	Noise Figure
QRFH	Quadridged Flared Horn

RF Radio Frequency

SARAO South African Radio Astronomy Observatory

SEFD System Equivalent Flux Density

SETI Search for Extraterrestrial Intelligence

SKA Square Kilometre Array

SKA-mid Square kilometre Array Mid-Frequency Component

SKA1 Square Kilometre Array Phase 1

SNR Signal-to-noise Ratio

SWE Spherical Wave Expansion

VNA Vector Network Analyser

XP Cross-Polarization

Chapter 1

Introduction

Much like military technology, radio astronomy instrumentation is at the forefront of radio antenna and receiver design research as the sensitivity of radio telescopes is pushed to its limits to make new discoveries. Achieving this high sensitivity becomes particularly challenging above 10 GHz as atmospheric attenuation and radio noise due to water vapour and oxygen increases exponentially. The high frequency and wide processing bandwidths required for these applications requires sophisticated front-end signal conditioning for a high system sensitivity. The science drive for new discoveries has led to the development of large telescope array projects such as the Square Kilometre Array [1] which is arguably one of the most exciting large scale scientific projects of our time and a demonstration of effective international collaboration. In the 1950's, the first telescope arrays were used for measurements using interferometry pioneered by Mike Ryle who published high resolution images of Cassiopeia-A and Cygnus-A using the Cambridge One-Mile Telescope [2]. Radio interferometry using an array of relatively smaller telescopes is used to achieve high angular resolution as opposed to using a single dish with a larger aperture.

1.1 SKA Project and MeerKAT

The SKA is an international effort to build the world's largest and most sensitive Radio Telescope array with a combined collective area of one square kilometre. The first phase of the project (SKA1) comprises of the mid-frequency telescope (SKA1-mid) hosted in South Africa and the low-frequency (SKA1-low) to be hosted in Australia. Eight other African countries will host telescopes as part of the African Very Long Base Line Interferometry (AVN). The project is expected to be online in 2020, however, precursor telescopes are already online and under development to demonstrate the science capabilities of SKA.

Fig. 1.1 Aerial photograph of part of MeerKAT array in the Northern Cape of South Africa. *Image by SARAO.*

MeerKAT is an array of 64 interlinked telescopes hosted in the Karoo region of the Northern Cape [3]. MeerKAT is a precursor to the SKA and will eventually be part of the mid-frequency component. Each MeerKAT antenna consists of a offset-fed Gregorian reflector antenna with a 13.5 m main reflector and 3.8 m sub-reflector. Currently, MeerKAT is planned to operate up to a frequency of 14.5 GHz. The telescope is planned to have four receivers: UHF, L, S and X Band. The L-Band receiver for the telescope has been developed and is currently online. The planned frequency bands for MeerKAT are shown in Table 1.1.

Table 1.1 MeerKAT Frequency Bands.

Band	**Frequency Range**
UHF-Band	580 MHz – 1015 MHz
L-Band	900 MHz – 1670 MHz
S-Band	1750 MHz – 3500 MHz
X-Band	8000 MHz – 14500 MHz

1.2 Aim for This Project

The reflector surface accuracy achieved for MeerKAT (0.6 mm RMS) allows it to operate at frequencies much higher than the planned 14.5 GHz, the aim of this project is to design a concept receiver operating from 14.5 to 20 GHz to make full use of this surface accuracy. The receiver system design consists of a corrugated feed antenna and front-end signal conditioning electronics using off-the-shelf connectorized modules and custom-made filters. The front-end

receiver down-converts the input frequency to an intermediate frequency (IF) of 4.5 GHz. An ambient LNA and single polarized feed antenna is used for this system.

1.2.1 Ruze Loss

The upper frequency limit of operation of a reflector antenna is determined by the accuracy of its surface. An important figure of merit for a reflector antenna's performance is the aperture efficiency of the antenna η_{ap}, which is a normalisation of the antenna's gain with respect to its physical area as shown by:

$$\eta_{ap} = \frac{A_e}{A_{phy}}, \tag{1.1}$$

where A_e is the effective area and A_{phy} is the physical area of the antenna. The aperture efficiency can be broken down into several sub-efficiencies to be discussed in detail in the next chapter. One of the main contributing factors to the aperture efficiency is the reflector surface efficiency η_{surf} which is defined as the ratio of the gain of a reflector to that of a perfect paraboloidal reflector [4]. The random surface errors lead to a reduction in the gain of the antenna. Ruze [5] presented a method to calculate η_{surf} using the RMS surface error of the reflector and wavelength:

$$\eta_{surf} = exp\left[-\left(\frac{4\pi\sigma}{\lambda}\right)^2\right], \tag{1.2}$$

where σ is the RMS surface error and λ is the wavelength of operation. Fig. 1.2 shows the surface efficiency for 0.6 mm RMS error as a function of frequency. A traditional rule-of-thumb states that the surface efficiency should typically be above 0.54 [4]. Using (1.2) for MeerKAT with the achieved RMS surface accuracy of 0.6 mm gives a surface efficiency of 0.78 at 20 GHz, for S and X-band the surface efficiency is 0.98 and 0.87 respectively. The ultimate goal for SKA mid frequency instrument is to have an upper frequency limit of 24 GHz [6].

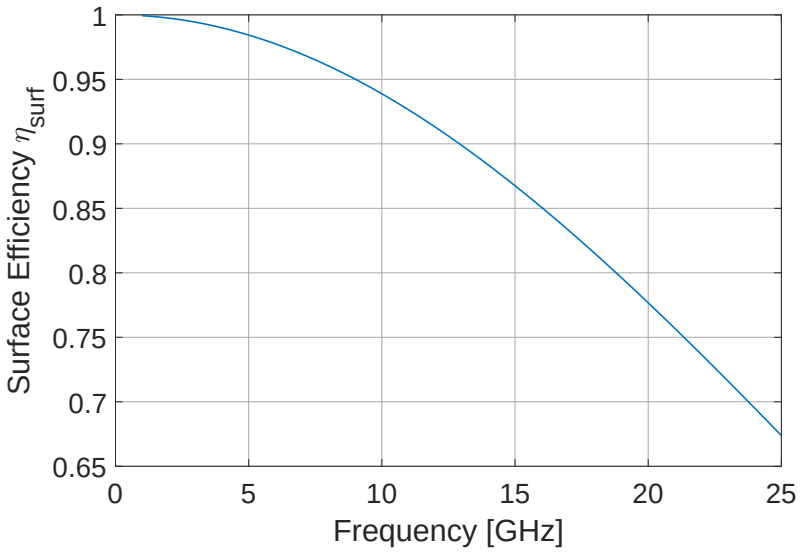

Fig. 1.2 Surface Efficiency against Frequency for 0.6 mm RMS surface accuracy.

1.3 Project Overview

1.3.1 Antenna Design

A wide-axially conical corrugated horn antenna was designed for the system. The antenna's full electromagnetic simulations and optimization was carried out in FEKO [7]. The corrugated horn antenna uses two corrugations and is fed by a single linear polarization using a tapered circular to square waveguide transition. The performance of the feed on the full reflector system is estimated using a model of a dual offset-Gregorian antenna in FEKO using MeerKAT geometric parameters.

1.3.2 Front-End Receiver Design

A single down-coversion heterodyne receiver was designed. An IF of 4.5 GHz and bandwidth of 2.5 GHz was chosen for the system. The 4.5 GHz IF is planned to be bandpass sampled at 6 Giga-samples per second (GSPS) in the second Nyquist zone. The system uses connectorized modules for the mixer and all the amplifiers. System simulation and analysis was performed using National Instrument's AWR Visual System Simulator (AWR VSS) [8]. Both the image reject filter [1] and anti-aliasing filter were realised using microstrip distributed bandpass filters designed in CST Microwave Studio [10].

[1] Image reject filter was designed as a final year student project by Tauriq Latief [9].

1.4 Thesis Outline

Chapter 2 gives a brief introduction to radio astronomy and discusses the figure of merit for radio telescopes. An overview of reflector antenna theory with focus on dual offset-fed Gregorian antennas is presented. The chapter concludes by presenting a theoretical analysis of the expected aperture efficiency of MeerKAT at the extended frequency range using its geometric parameters.

With the figure of merit presented, Chapter 3 looks at the design and analysis of the feed horn antenna. Specific design theory and a parameter study of wide-axially corrugated horns is covered in this chapter. The procedure for the estimation of the feed performance as a feed for the reflector using Electromagnetic (EM) Simulation software is also given. The measurement results for the manufactured antenna are presented in Chapter 4.

Chapter 5 presents the design of the front-end super-heterodyne receiver system. Design considerations such as the implications of the choice of the IF and spurious analysis of the receiver chain are detailed in this section. Chapter 6 presents the measurement results for the receiver front-end. With the antenna and receiver front-end design complete, an estimate of the full system sensitivity is presented in the chapter. Conclusions and recommendations are given in Chapter 7.

Chapter 2

Introduction to Radio Astronomy and Telescopes

Radio Astronomy is the study of natural radio emission from celestial sources [4]. It can be dated back to the 1930s when Grote Reber made the first radio telescope after the discovery of cosmic waves by Bell Laboratory engineer Karl Jansky. Radio astronomy takes advantage of the transparency of the earth's atmosphere to radio waves. The transparent window for ground based radio astronomy on the EM spectrum is illustrated in Fig. 2.1. This chapter gives a brief introduction to radio astronomy and the basics of radio telescope measurements. Reflector antenna theory with focus on the offset-fed Gregorian antenna and theoretical estimation on the aperture efficiency using MeerKAT geometric parameters is presented.

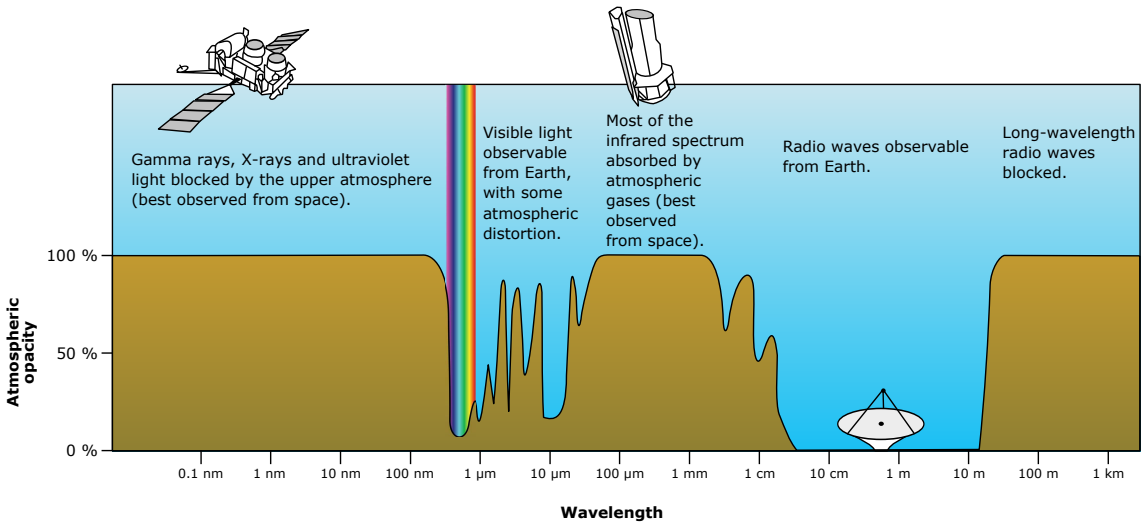

Fig. 2.1 EM spectrum and atmospheric opacity showing ground observable window. *Original Image by NASA.*

2.1 Cosmic Radio Emission

Cosmic sources emit EM radiation through the acceleration of charged particles due to both thermal and non-thermal mechanisms. Cosmic emissions can be divided into spectral line and continuum emissions detailed below.

2.1.1 Spectral Line Emissions

Spectral lines are emissions over a narrow range of frequency caused by energy transitions in atoms or molecules. As the rest frequencies of these sources are well known, astronomers can determine physical characteristics of the sources and use the Doppler shift in spectral lines to calculate the relative motion of sources, referred to as redshift when the frequency is down shifted (source moving away). The redshift can also be used to measure the cosmological distance of sources. Some important spectral lines used by astronomers are shown in Table 2.1. The 21 cm neutral Hydrogen (HI) line falling within the L-band is one of the most abundant and observed lines.

Table 2.1 Some Astronomical Spectral lines [11].

Substance	**Rest Frequency (MHz)**
Deuterium (DI)	327.384
Hydrogen (HI)	1420.406
Methyladyne (CH)	3335.481
Methanol (CH_2OH)	6668.518
Ionized Helium Isotope (l^3HeII)	8665.650
Methanol (CH_3OH)	12178
Formaldehyde (H_2CO)	14488
Cyclopropenylidene (C_3H_2)	18343
Water Vapour (H_2O)	22235

2.1.2 Continuum Emissions

These are emissions that show a wideband response due to charged particles moving with a wide range of frequency [12]. Continuum emissions can be both non-thermal and thermal. Thermal (blackbody) emissions are caused by sources whose particles exhibit energy transitions due to their temperature. An example of a common source of continuum radiation is that of cosmic dust which is important for studies on the solar system formation. Non-thermal radiation is also observed when charged particles rotate around a magnetic field thereby

creating electromagnetic propagation. Through this emission mechanism, astronomers can observe broadband spectra from Pulsars [1].

2.2 Radio Source Detection and Sensitivity

Radio astronomers measure the intensity of received radiation from astronomical sources in terms of the brightness or intensity B_v in units $\mathrm{Wm^{-2}\,Hz^{-1}\,sr^{-1}}$ where v, denotes the frequency. It can be defined as the measure of radiated energy flow per unit area, per unit time, per unit frequency bandwidth, and per unit solid angle $d\Omega$ [2]. An illustration of the two dimensional measurement is shown in Fig. 2.2 for the power flowing within the solid angle $d\Omega$ and area $d\sigma$. From Planck's law of black body radiation, B_v is calculated by:

$$B_v(v,T) = \frac{2hv^3}{c^2}\frac{1}{e^{hv/kT}-1} \quad [\mathrm{Wm^{-2}\,Hz^{-1}\,sr^{-1}}], \tag{2.1}$$

where h is Planck's constant $= 6.626 \times 10^{-34}$ [Js], k is Boltzmann's constant $= 1.38 \times 10^{-23}$ [$\mathrm{JK^{-1}}$], c is the speed of light $= 3 \times 10^8$ [$\mathrm{ms^{-1}}$], v is the frequency [Hz] and T is the physical temperature of the black body [K]. From Rayleigh-Jeans limit for black body radiation, B_v is approximated as:

$$B_v(v,T) = \frac{2v^2kT}{c^2} \quad [\mathrm{Wm^{-2}\,Hz^{-1}\,sr^{-1}}]. \tag{2.2}$$

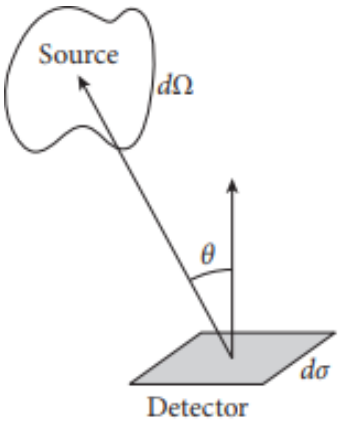

Fig. 2.2 Illustration of intensity measured by detector at an angle θ. $d\Omega$ and $d\sigma$ are the observed solid angle of the source and detector area respectively[4].

[1] Pulsars are magnetized neutron stars that appear to emit periodic short pulses of radio radiation with periods between 1.4 ms and 8.5 s [4].

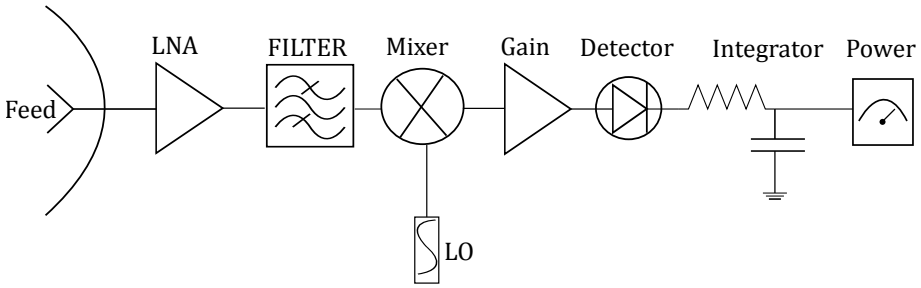

Fig. 2.3 Simple radio astronomy radiometer system.

The radio telescope measures the flux density S_v of a source which is the integral of the spectral brightness B_v integrated over the source's subtended solid angle $d\Omega$ measured in $\mathrm{Wm^{-2}\,Hz^{-1}}$:

$$S_v = \iint\limits_{source} B_v(\theta,\phi)\, d\Omega \quad [\mathrm{Wm^{-2}\,Hz^{-1}}], \tag{2.3}$$

However, the power density received from astronomical sources is so small that astronomers introduced a unit called the "Jansky" where $1\,\mathrm{Jansky(Jy)} = 10^{-26}\,\mathrm{Wm^{-2}\,Hz^{-1}}$. An illustration of a simple radiometer system for making these measurements is shown in Fig. 2.3. The power measured by the receiver is a sum of different components that make up the system equivalent noise temperature (T_{sys}). T_{sys} consists of the brightness temperature of the source being measured T_{source}, the cosmic microwave background T_{cmb}, atmospheric noise T_{atm}, spillover temperature T_{spill} and the receiver temperature T_{Rx}:

$$T_{sys} = T_{source} + T_{cmb} + T_{atm} + T_{spill} + T_{Rx} \quad [K]. \tag{2.4}$$

The total power P received by the radio telescope for a given bandwidth Δv and for a single polarization is then expressed as

$$P = \frac{1}{2} S_v A_e \Delta v \quad [W], \tag{2.5}$$

where A_e is the effective collecting area of the antenna. An important figure of merit for a radio telescope system is the **System Equivalent Flux Density (SEFD)** defined as the flux density of a point source that would cause the noise power in the receiver to be twice that of the system noise when the telescope is not pointed at the source [2]. Replacing P with $KT_{sys}\Delta v$ in (2.5):

$$SEFD = \frac{2kT_{sys}}{A_e} \times 10^{26} \quad [\mathrm{Jy}]. \tag{2.6}$$

The sensitivity of the telescope can be represented as the RMS variation in the flux density $S_{v_{rms}}$ calculated as:

$$S_{v_{rms}} = \frac{2kT_{sys}}{A_e\sqrt{\tau\Delta v}} \times 10^{26} \quad [\text{Jy}], \tag{2.7}$$

where τ is the integration time and Δv is the sampled bandwidth.

2.3 Reflector Antennas

Reflector antennas are commonly used in radio astronomy and satellite communication systems due to their high directivity. Their use is said to be traced as far back as the third century when Archimedes used a parabolic reflector to direct sun rays towards Roman ships to burn them[13]. However, their first non-optical use came in 1888 when Heinrich Hertz demonstrated the existence of radio waves. Their general theory of operation consists of one or more reflectors that are designed to collimate incident waves to a focal point by reflection and transmission [14]. Their high gain and pencil beam pattern achieved makes them particularly attractive for radio astronomy applications.

Different types of reflector antennas are used depending on the application, the most common curved reflectors being a prime-focus reflector which consists of a parabola and a feed located at its focal point. Dual reflectors such as the Cassegrain and the Offset Gregorian, which is the focus of discussion here are also used for improved performance. The general geometry of the antennas are illustrated in Fig. 2.4. The corner reflector (Fig. 2.4a) uses simple reflection to direct waves whilst the parabolic antennas make use of Geometric Optics theory. For a parabolic surface, incident waves are focused onto its focal point, reciprocity also applies in that if a transmitting feed is placed at the focal point, the waves will emerge as a parallel beam [15] as shown in the prime-focus (Fig. 2.4b) arrangement. Placing the feed at the focal point has some physical disadvantages such as the need to use longer feed lines, difficult accessibility for maintenance and the blockage caused by the feed mount. A solution for this is placing another reflector at the focal point so that waves are focused to a more convenient feed point as in the Cassegrain (Fig. 2.4c) and Gregorian (Fig. 2.4d) antennas.

2.3.1 Offset Gregorian Dual-Reflector

The offset Gregorian antenna is a popular choice in radio astronomy because of the ability to improve performance using the shaping of the sub-reflector and the more convenient location of the feed. Furthermore, there is no losses due to feed blockage as the feed is not in the aperture of the main reflector. The dual reflector geometry is derived from its optical

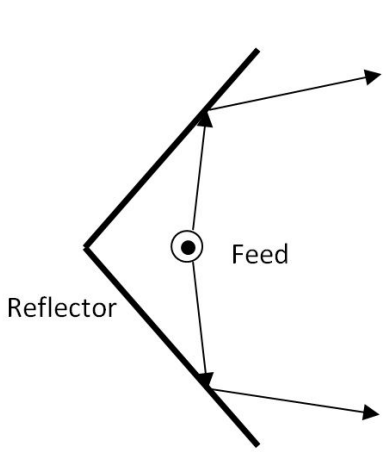

(a) Corner

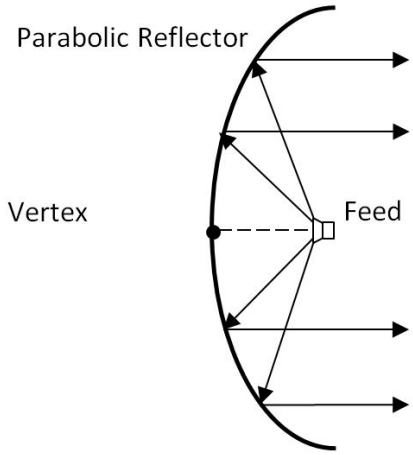

(b) Prime-focus

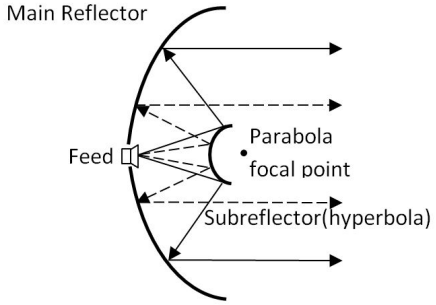

(c) Cassegrain

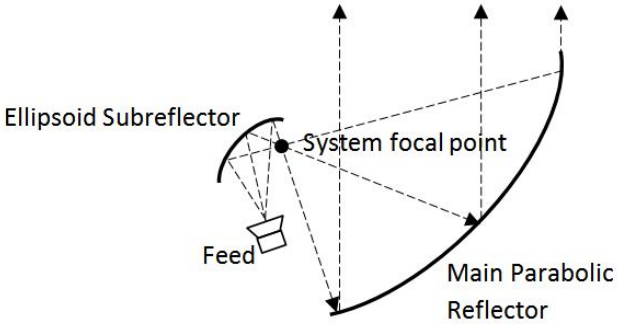

(d) Dual Offset Gregorian

Fig. 2.4 Some common reflector antenna types. *Illustration adapted from [15].*

telescope counterpart where the effective focal length of the system is increased [16]. An elliptical sub-reflector is placed in such a way that one of its foci coincides with the focal point of the paraboloidal main-reflector whilst the other one coincides with the feed location.

The detailed geometry of the offset Gregorian is illustrated in Fig. 2.5 showing the main design parameters, with geometry parameters described in able .2.2. Any design can be represented by defining a set of five input parameters as long as they satisfy Mizugutch condition [2] [17]. Cross-polarization performance of the reflector can be improved by rotation of the sub-reflector axis. Design equations and procedure as presented by Granet [18] can be used to design different geometries using only five input parameters.

[2] A geometric optics condition for low sidelobes and cancelling cross-polarization component caused by asymmetrical configuration in dual reflectors.

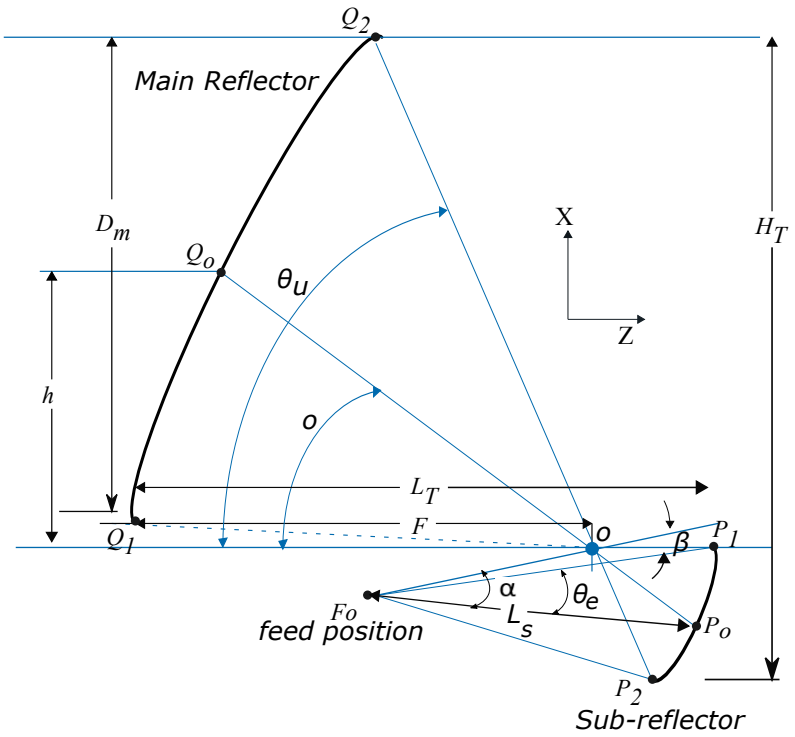

Fig. 2.5 Offset Gregorian Geometry

Table 2.2 Offset Gregorian Design Parameters

Parameter	Description
D_m	Diameter of the main reflector in the xy plane
F	Main reflector focal length
h	Main reflector offset height
θ_o	Main reflector offset angle
θ_u	Offset angle of top of the main reflector
θ_L	Offset angle of the bottom of the main reflector
β	Sub-reflector tilt angle
θ_e	Half-angle subtended by the sub-reflector from the feed point F_o
α	Tilt angle between sub-reflector and feed
e	Sub-reflector ellipse eccentricity
a	Sub-reflector surface parameter
c	Sub-reflector half interfocal distance ($c = ae$)
L_s	Distance between the feed and the sub-reflector
L_m	Distance of the main-reflector from the sub-reflector
L_t	Maximum distance of the two reflector combination (z axis)
H_t	Maximum vertical length of the two reflector combination (y axis)

The radiation pattern of the geometry is mainly determined by the effective focus to diameter (F/D) ratio of the reflector and the half subtended feed angle θ_e. The feed is designed

to illuminate the sub-reflector at the centre with minimal energy spillover and efficient taper at the edge of the sub-reflector. Feeds are normally designed to have -10 dB to -12 dB taper at the half subtended angle for an efficient illumination. MeerKAT telescope design can be described using the following five input parameters [19]: $D_m = 13.5\,\text{m}, \theta_e = 48.89°, \beta = 45.47°, \theta_o = -63.20°$ and $Ł_s = 2.419\,\text{m}$. Radiation pattern simulated using GRASP [20] with the design parameters and a theoretical Gaussian feed pattern is shown in Fig. 2.6 at 1 GHz (Fig. 2.6a), 5 GHz (Fig. 2.6b), 10 GHz (Fig. 2.6c) and 22 GHz (Fig. 2.6d). The directivity of the reflector increases with the frequency as the reflector becomes electrically larger at smaller wavelengths.

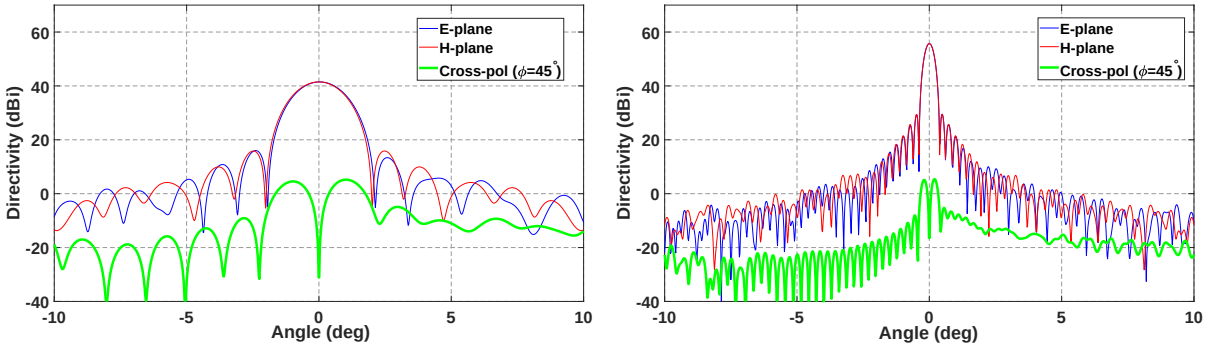

(a) 1 GHz

(b) 5 GHz

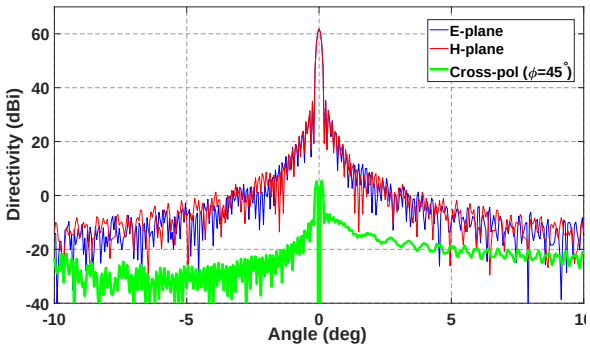

(c) 10 GHz

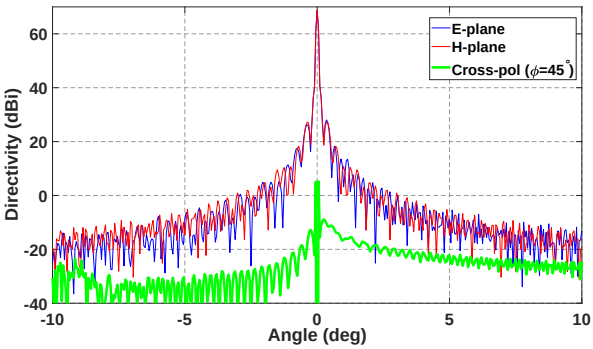

(d) 22 GHz

Fig. 2.6 Radiation pattern of offset Gregorian with meerkat design parameter using a theoretical Gaussian pattern with a -10 dB taper edge taper.

2.4 Telescope Figure of Merit

2.4.1 Aperture Efficiency of Reflector

Performance of aperture antennas such as reflector antennas is measured by the aperture efficiency. It relates the actual directivity of an antenna to the maximum directivity achievable for a given physical area i.e the ratio of an antenna's effective area to the physical area:

$$\eta_{ap} = \frac{A_e}{A_{phy}}. \tag{2.8}$$

The aperture efficiency can be described by (2.8) as discussed in Chapter 1. As it relies on the performance of the feed, it is sometimes referred to as the feed efficiency and can be factorized into its sub-efficiencies [21] to understand the contributing factors to the total efficiency. Assuming an idealized rotationally symmetric feed antenna pattern, the feed efficiency is given by:

$$\eta_f = 2\cot^2(\theta_e/2)\frac{|\int_0^{\theta_e} CO(\theta)\tan(\theta/2)d\theta|^2}{\int_0^{\pi}[|CO(\theta)|^2+|XP(\theta)|^2]\sin\theta d\theta}, \tag{2.9}$$

where θ_e is the subtended half angle of the paraboloid in the case of a prime-focus and half-angle of sub-reflector in the case of a Cassegrain or dual Gregorian antenna. $CO(\theta)$ and $XP(\theta)$ are the co and cross-polar radiation patterns respectively. The efficiency is factorized into sub-efficiencies:

$$\eta_f = \eta_{sp}\eta_{pol}\eta_{ill}\eta_{\phi}. \tag{2.10}$$

Spillover Efficiency η_{sp}

The spillover is the ratio of the total power within the half subtended angle θ_e to the total power radiated by the feed. The total power considers both co and cross-polarizations. The spillover is critical as a low efficiency means more antenna noise temperature affecting the gain to temperature performance:

$$\eta_{sp} = \frac{\int_0^{\theta_e}[|CO(\theta)|^2+|XP(\theta)|^2]\sin\theta d\theta}{\int_0^{\pi}[|CO(\theta)|^2+|XP(\theta)|^2]\sin\theta d\theta}. \tag{2.11}$$

Polarization Efficiency η_{pol}

The polarization efficiency represents the ratio of power received in a specified polarization to the power that would be received when the polarization is adjusted for maximum power. For a circularly polarized feed it is given by the following expression:

$$\eta_{pol} = \frac{\int_0^{\theta_e} |CO(\theta)|^2 \sin\theta d\theta}{\int_0^{\theta_e} [|CO(\theta)|^2 + |XP(\theta)|^2] \sin\theta d\theta}. \tag{2.12}$$

The efficiency is a measure of the symmetry of the far field pattern (symmetrical E and H plane). For feeds such as corrugated horns this efficiency is normally very high >98% [14]. For a linear polarization efficiency η_x, the following relationship is used:

$$(1-\eta_{pol}) = 2(1-\eta_x). \tag{2.13}$$

Illumination Efficiency η_{ill}

The illumination efficiency is a measure of loss due to non-uniform illumination of the aperture plane. Therefore, a trade-off needs to be reached between the spillover and illumination by designing the optimum taper of the feed pattern at the edge of the reflector:

$$\eta_{ill} = 2\cot^2(\theta_e/2) \frac{[\int_0^{\theta_e} |CO(\theta)| \tan(\theta/2) d\theta]^2}{\int_0^{\theta_e} [|CO(\theta)|^2 \sin\theta d\theta}. \tag{2.14}$$

Phase Efficiency η_ϕ

The phase efficiency represents losses due to phase errors caused by the feed phase centre location relative to the focal point of the reflector:

$$\eta_\phi = \frac{|\int_0^{\theta_e} CO(\theta) \tan(\theta/2) d\theta|^2}{[\int_0^{\theta_e} CO(\theta) \tan(\theta/2) d\theta]^2}. \tag{2.15}$$

2.5 Theoretical Estimation of the Efficiency

A theoretical cosine feed of the form $\cos^n(\theta/2)$ can be used to approximate the efficiency of a paraboloidal reflector as the integrals above can be solved analytically [15, 14]. The feed pattern is assumed to be:

$$CO(\theta) = (n+1)\cos^{2n}(\theta/2),\ XP(\theta) = 0, \tag{2.16}$$

where n is chosen such that the feed pattern produces the required edge taper at the half-subtended angle θ_e. With the phase and polarization assumed to be perfect, the feed efficiency in (2.11) reduces to:

$$\eta_f = 4\cot^2(\theta_e/2)[1-\cos^n(\theta_e/2)]^2(n+1)/n^2. \tag{2.17}$$

Further losses are due to sub-reflector edge diffraction and surface tolerance efficiency as described by (1.2). The diffraction efficiency η_{diff} for an offset-Gregorian (see Fig. 2.5) with the feed pattern described above can be calculated by [22, 23]:

$$\eta_{diff} = \left|1+\frac{n\sin^2(\theta_e/2)\cos^n(\theta_e/2)}{1-\cos^n(\theta_e/2)}\frac{(j-1)}{2\pi}\frac{\triangle p}{D_m}\right|^2, \tag{2.18}$$

where $\triangle p$ is a wavelength dependant parameter used to describe the transition region for the theory introduced in [24], for an offset Gregorian, it's dependant on the position of the sub-reflector and main reflector positions. The average value is calculated for the central ray through the system focal point o in Fig. 2.5 as:

$$\triangle p = \sqrt{\frac{\lambda((o\text{-}QO)+(o\text{-}PO)}{\pi}\left|\frac{(o\text{-}QO)}{(o\text{-}PO)}\right|}, \tag{2.19}$$

where λ is the wavelength, o-QO and o-PO are the central ray distances from the focal point to the main reflector and sub-reflector respectively. With the diffraction efficiency and surface efficiency terms included, the total estimated efficiency can be expressed as:

$$\eta_{ap} = \eta_f \eta_{diff} \eta_{surf}. \tag{2.20}$$

An estimate of MeerKAT's efficiency using a cosine feed pattern on a dual-reflector with half subtended angle $\theta_e = 48.89°$ and feed edge taper -10 dB (n=13) was calculated. The efficiency of as a function of illumination taper calculated using (2.17) is shown in Fig. 2.7. It can be seen from the graph that the optimum feed illumination taper for this configuration for maximum efficiency is approximately 10 dB. Fig. 2.8 shows the different sub-efficiencies and the total efficiency compared to the efficiency calculated from the directivity simulated in GRASP for different frequencies (shown in black dots). The aperture efficiency η_g in GRASP is calculated using:

$$\eta_g = \frac{D_{max}\lambda^2\eta_{surf}}{4\pi A_{phy}}, \tag{2.21}$$

where λ represents wavelength, D_{max} is the maximum directivity simulated in GRASP and A_{phy} is the physical area of the antenna. It can be seen from the graph that as frequency increases, diffraction at edges of the reflector becomes less significant whilst the surface efficiency reduces exponentially significantly degrading the overall efficiency of the system.

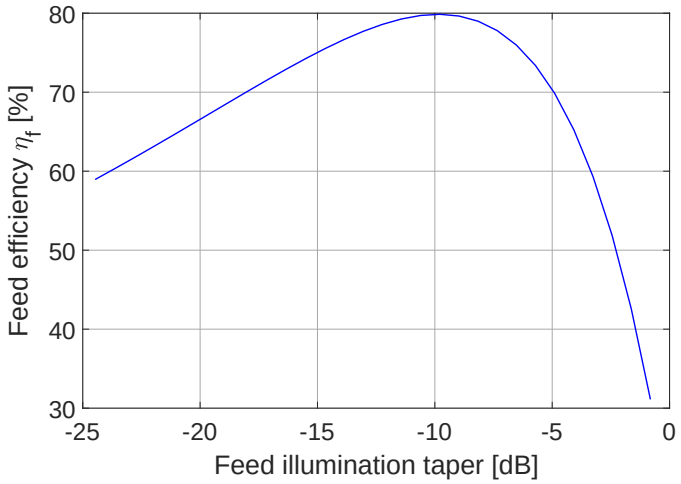

Fig. 2.7 Offset Gregorian calculated efficiency against illumination taper for $\theta_e = 48.89°$

.

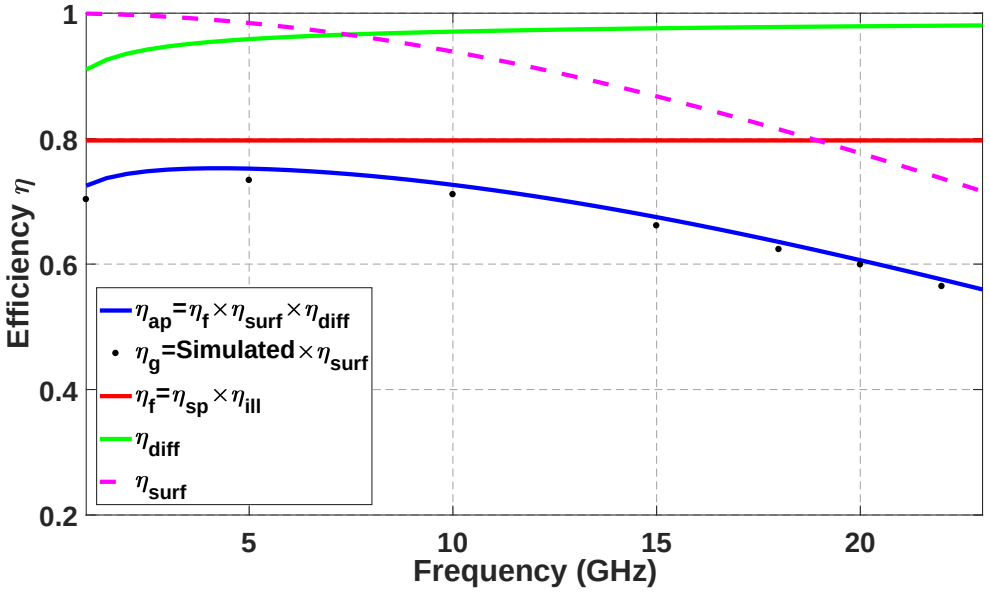

Fig. 2.8 Offset Gregorian estimated efficiency with cosine feed pattern for $\theta_e = 48.89°$. η_g is the simulated aperture efficiency in GRASP with surface efficiency η_{surf} factored; η_f- feed efficiency; η_{sp}- spillover efficiency ;η_{ill} illumination efficiency.

2.6 Conclusion

In this Chapter a basic introduction to radio astronomy and radio telescopes has been given. The key parameters that affect the sensitivity of a radio telescope were presented; the main considerations for radio telescope system design are the aperture efficiency of the antenna and the receiver system temperature. An overview of reflector antennas with focus on the offset Gregorian were also discussed. The key parameters of the antenna geometry that can be used for analysis of the antenna were introduced. With the feed sub-efficiencies detailed in the chapter, an initial calculation of the achievable antenna and feed performance can be made before rigorous EM simulations in the initial system design stage. In the next chapter the feed design considerations and the design of a corrugated feed horn will be discussed.

Chapter 3

Design and Analysis of Feed Antenna

The need for high efficiency feeds in satellite communication and radio astronomy applications saw the development of corrugated horn feeds because of their low cross-polarization and symmetrical radiation patterns. These features make them especially attractive for radio astronomy applications. Radio astronomy feeds emphasise on both a large collecting area (high aperture efficiency) and low system temperature (T_{sys}) hence the need for highly efficient feeds. Kay[25] discovered in the 1960s that antenna pattern efficiency was improved when quarter wave corrugations were added to the aperture of the antenna. Extensive research was also done by other researchers from ERA Technology and CSIRO (The Commonwealth Scientific and Industrial Research Organisation) in Australia. In the 1970s, work on corrugated horn designs advanced due to the high demand from the satellite communication market [26].

This chapter presents the design and simulation results for a wide axially conical corrugated horn operating from 14.5 to 20 GHz with a single linear polarized feed. A brief overview of reflector feeds for radio astronomy and performance requirements are introduced in the first section. A brief overview of some state-of-the-art feeds for reflector antennas and their main characteristics is given in the first section. The second part discusses the design and analysis of a wide axially conical corrugated horn feed antenna including its main parameters and how these affect performance. The last part presents the simulation results of the final build of the antenna.

3.1 Reflector Antenna Feed Characteristics

The performance of reflector antenna systems in both radio astronomy and satellite communication is greatly affected by the feed and receiver system. The feed efficiency and subsequent sub-efficiencies have been discussed in Section 2.4. An efficient feed for a reflector antenna

has a Gaussian like symmetrical radiation pattern, low side-lobes and low cross-polarization. It is also necessary for the feed pattern beamwidth to remain constant over the frequency of operation with an easy to change illumination taper. The feed design involves illuminating the surface of the reflector evenly whilst under-illuminating the edge of the reflector to avoid spillover noise from the ground. Fig. 3.1 shows an illustration of the feed illumination on a reflector antenna showing the spillover region and illumination taper.

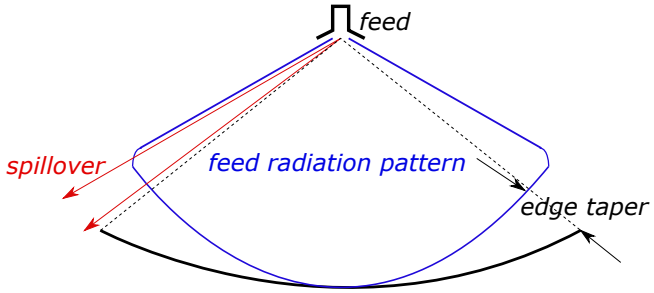

Fig. 3.1 Illustration of feed illumination on reflector antenna [14].

.

The required characteristics of a radio astronomy reflector feed exhibited by corrugated horns can be summarised as follows:

1. Symmetric radiation pattern over the operation bandwidth.
2. Easily controllable and constant beamwidth.
3. Low side-lobes and cross-polarization.
4. Constant phase centre position over operation bandwidth.

For horn design and measurements, it is also essential to clarify the meaning of co-polarization and cross-polarization as defined by Ludwig's third definition [27]. It states that the co-polar field is that of a Huygens' source (electric and magnetic dipoles with orthogonal axes lying in the aperture plane with equal fields in phase along the z-axis). The cross-pol field is that obtained by a 90° rotation of the reference source. Mathematically, the definition of the co-pol field $E_{co(\theta,\phi)}$ and the cross-polar fields $E_{XP(\theta,\phi)}$ are:

$$\begin{aligned} E_{co(\theta,\phi)} &= E_{(\theta,\phi)}(\sin\phi\,\hat{\theta} + \cos\phi\,\hat{\phi}) \\ E_{XP(\theta,\phi)} &= E_{(\theta,\phi)}(\cos\phi\,\hat{\theta} - \sin\phi\,\hat{\phi}), \end{aligned} \tag{3.1}$$

where $\hat{\phi}$ and $\hat{\theta}$ are the well known spherical unit vectors.

3.1.1 Corrugated Horn Balanced Hybrid-Mode

Conventional feeds achieve aperture efficiencies of 50-60% whilst corrugated horn feeds can achieve aperture efficiencies of the order 75-80%. This is due to the high spillover efficiency and low cross-polarization losses [15]. Smooth walled horns exhibit diffraction in the aperture and cross-polar sidelobes in the 45° plane corresponding to the difference in the E- and H-plane radiation pattern [14]. Diffraction is significant in the edges perpendicular to the E-field at the horn aperture as illustrated in Fig. 3.2.

Corrugations in the surface introduce identical boundary condition in each plane. In the E-plane, quarter wavelength deep corrugations present a magnetic conducting surface. In the H-plane, the E-field is parallel to the ridges and if the grooves are narrower than half a wavelength, the E-field cannot penetrate the corrugations as the parallel waveguide formed by the walls of the corrugations is below cut-off. In order to satisfy this boundary condition, the propagating mode in the antenna consists of both TE_{10} and TM_{10} hence referred to as the balanced hybrid mode HE_{11}. Fig. 3.3 shows the electric field distribution at the aperture of the horn, the fields are nearly linear at the aperture of the horn. As the farfield can be predicted by taking the Fourier Transform of the aperture field, the farfield pattern of the horn will also exhibit a linear distribution.

(a) Smooth E-Plane horn Diffraction. (b) Smooth conical Horn Diffraction.

Fig. 3.2 E-field edge diffraction In Smooth Walled Horns [28]

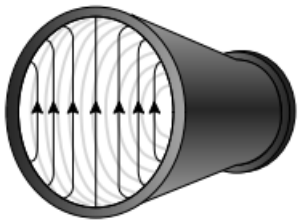

Fig. 3.3 Electric field in HE_{11} of a corrugated horn antenna at aperture [29].

As presented in [26], the hybrid mode conditions can be analysed by considering the field in a corrugated waveguide assuming a small flare angle horn, as shown in Figure 3.4. p

is the pitch, w is the corrugation width and s is the slot depth. Taking the x direction as the co-polarization and the y direction as the cross-polarization with unit vector $\hat{i}$, the aperture field E is:

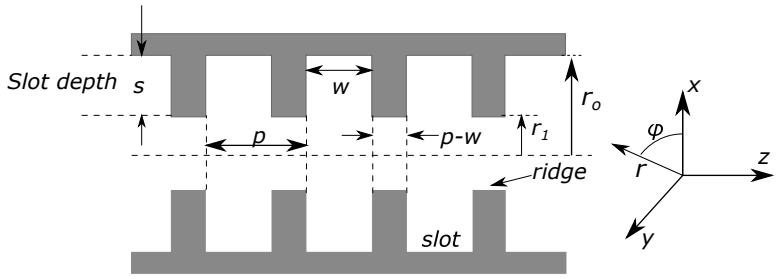

Fig. 3.4 Inside wall of a typical corrugated waveguide

$$E = AJ_o(Kr)\hat{i}_x - \left(\frac{X-Y}{4}\right)\frac{U_o^2}{kr_1}J_2(Kr)(\cos 2\phi \hat{i}_x + \sin 2\phi \hat{i}_y), \tag{3.2}$$

where r is the radius, $\hat{i}_{x,y}$ are unit vectors in the x and y direction, $J_n(\mathrm{Kr})$, $n = 0,2$ is a Bessel function of the first kind and order n, A is an amplitude coefficient, U_o is a normalised transverse wavenumber, k and K are free-space and transverse wavenumbers respectively. X and Y are the normalised reactance and admittance of the waveguide boundary at $r = r_1$:

$$X = -j\frac{E_\phi}{H_z}Y_F \tag{3.3}$$

$$Y = -j\frac{H_\phi}{E_z}Z_F, \tag{3.4}$$

$Z_F = 1/Y_F$ is the free-space impedance. It can be seen from (3.2) that zero cross polarization is achieved when the X-Y=0. It is also important to note that at this condition the aperture field will also be independent of ϕ, hence a linear field distribution. The condition is satisfied when X and Y are finite and equal or they are both equal to zero. The balanced hybrid-mode in corrugated horns is as a result of the latter. $X = 0\,(E_\phi = 0)$ is achieved by having a sufficient number of corrugations per wavelength. $Y = 0\,(H_\phi = 0)$ is achieved by having the corrugation depth a quarter wavelength.

Different types of corrugated horns can be realised, some of the types are summarized in Table. 3.1. The choice of corrugated horn will depend on several factors such as the required beamwidth, bandwidth, aperture efficiency, size requirements and available manufacturing or cost.

Horn Type	**Illustration** [26]	**Advantages**	**Disadvantages**
Large Aperture, Narrow flare angle (D>4λ,θ<15°)	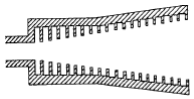	• Constant Phase Centre • Easy analysis (waveguide approximation)	• High attenuation • Narrow beamwidth limits application
Small Aperture, Narrow flare angle (D<4λ,θ<15°)	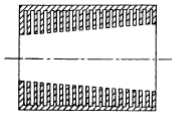	• Easier throat section matching than large aperture horns	• Narrow bandwidth • Horn flange affects cross-polarization
Wide flare angle, (θ>15°)	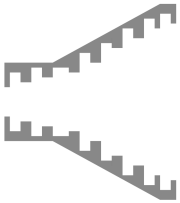	• Can have slots axially corrugated • Phase centre constant at apex	• Difficult throat section matching • Lower aperture efficiency • Beamwidth is not constant at max directivity flare angle
Profiled Horn	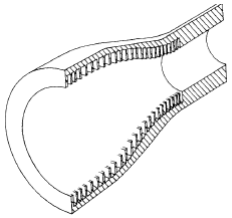	• Compact size	• Higher order mode and sidelobes excitation risk • Difficult to manufacture

Table 3.1 Corrugated Horn Types

3.1.2 Other State-of-the-Art Reflector Antenna Feeds

Several feed designs have been developed for high efficiency applications in radio astronomy. Extensive study of the different feeds and their performance is given in [30]. A brief summary of the feeds is given here:

- **The Allen Telescope Array (ATA) Feed** is a log-periodic based feed design designed for the Allen Telescope Array [31]. The ATA is an array of offset Gregorian antennas covering 500 MHz to 10 GHz frequency range built by the SETI Institute. The feed consists of four log periodic arms that form a pyramid as shown in Fig. 3.5a. Its main motivation is the ability to place the LNA directly at the terminals of the antenna for improved sensitivity [32]. The log-periodic design allows wide bandwidth operation and the ohmic losses associated with such antennas is compensated for by attaching the cryogenic electronics directly to the feed terminals. The antenna achieves a directivity of 12 dBi, cross-pol level of -10 dB, the average -10 dB half-beamwidth is consistent at about 42 ° over the band and the feed achieves an aperture efficiency of about 60% [33]. Its main drawback is the variation of its phase centre which affects efficiency, relatively poor cross-pol performance and its large size.

- **The Eleven Feed** is another log-periodic antenna developed at Chalmers University of Technology based on two parallel dipoles configured for a symmetrical radiation pattern (see Fig. 3.5b). It's so called eleven feed because of its parallel dipoles, more than 10:1 bandwidth and 11 dBi directivity [34]. Its main advantage is the almost constant phase centre over the frequency range, its relatively compact size and planar structure. The antenna achieves an aperture efficiency of 66% for a subtended half angle of 53° and a relative cross-pol level better than -10 dB as demonstrated in [34, 35].

- **Quad-ridged Flared Horn (QRFH)** is a good alternative to corrugated horns as it similarly has the flexibility in changing the beamwidth using the flare angle and a good input return loss. The antenna consists of a profiled horn with four symmetrically located ridges as shown in Fig. 3.5c. It's more broadband (7:1) than corrugated horns but efficiency and cross-polarization are inferior. The ridges and profiles flare produce a constant beamwidth and good return loss over a wide frequency range. In [36] a horn implemented with chokes designed for SKA achieves an aperture efficiency above 70%.

- **Sinuous Feed** is an impressive ultra-wideband option which also belongs to the log-periodic family of antennas. It consists of two sets of spiral arms for two orthogonal

polarizations (see Fig. 3.5d). Detailed studies of the antenna as a feed for the SKA have been carried out in [37, 38]. It has been shown to achieve 3:1 bandwidths and aperture efficiency of over 60%. However, its main drawback is its mediocre cross-polarization and tough to change beamwidth [39].

The feeds discussed above have impressive performance desired for ultra wide band systems as they eliminate the need for using multiple feeds to cover a wide frequency range. However, due to its flexible beamwidth design, symmetrical and low cross-pol radiation pattern, fairly easy to manufacture structure and 50 Ω input impedance, the wide-axially corrugated horn was selected as the feed choice for this application.

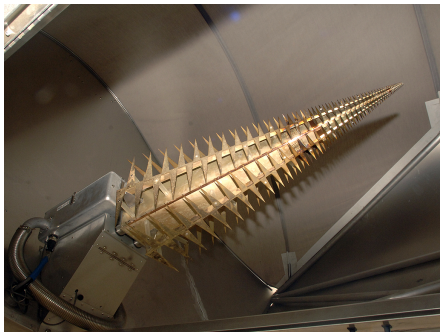

(a) Allen Telescope Array (ATA) Feed [40].

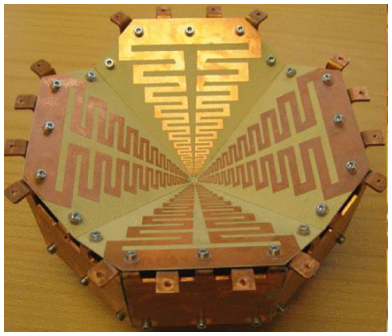

(b) Eleven Feed [41].

(c) Quad-ridged Flared Horn (QRFH) [39].

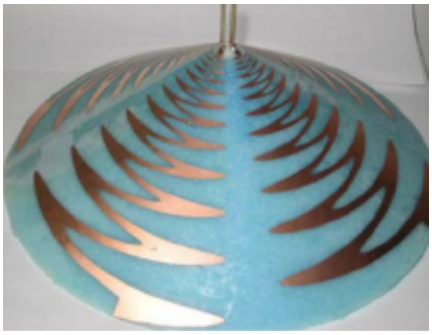

(d) Sinuous Feed [42].

Fig. 3.5 Some state-of-the-art feeds for reflector antennas.

3.2 Wide Axially Corrugated Horn Design and Analysis

This section discusses the design of a wide-axially corrugated horn feed for operation from 14.5 to 20 GHz. Simulations for the horn were performed in electromagnetic software FEKO [7] using its Method of Moments (MoM) solver. The design specifications for the horn are shown in Table 3.2. The main parameters for a wide-axially corrugated horn are shown in Fig.

3.6: α is the half flare angle, r_i input radius, w corrugation width, p pitch, s slot depth and r_o is the aperture radius. The horn consists of a circular waveguide section and corrugations in the direction of the aperture with a flare angle $\alpha \geq 15^\circ$. Design guidelines given in [26, 43] are used for the design process in this section.

Table 3.2 Feed Horn Design Goals

Parameter	Design Goal
Frequency range	f_{min}=14.5 GHz f_{max}=20 GHz
Co-pol pattern beamwidth	≈12 dB taper at 48.89°
Side-lobe level	≤ -25 dB
Cross-pol level	≤ -30 dB
Input return loss	≤ -15 dB

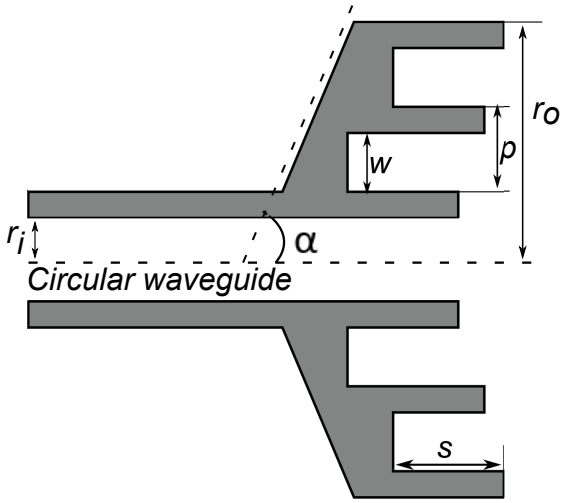

Fig. 3.6 Cross section view of geometric parameters of wide flare angle axially corrugated horn.

3.2.1 Circular Waveguide Section

The circular waveguide section radius r_i is calculated for the fundamental TE_{11} cut-off as:

$$r_i = \frac{3\lambda_c}{2\pi}, \tag{3.5}$$

where λ_c is the wavelength at the centre frequency f_c (17.03 GHz). This ensures a good return loss over the whole operating band with the TE_{11} cut-off at 10.47 GHz.

3.2.2 Horn Flare Angle

For the wide axially corrugated horns, the flare angle α controls the beamwidth of the horn. Design charts from [26] (see Appendix A.1) are used for initial values for the flare-angle. A flare angle is chosen depending on the required half-beamwidth. Fig. 3.7 shows the varying beamwidth for an axially corrugated horn simulated at 17.25 GHz. The increase in the beamwidth of the radiation pattern is observed as the flare angle is increased in Fig. 3.7a. Furthermore, an improvement in the cross-pol level towards the larger flare angle in Fig. 3.7b is observed.

The required co-polar pattern restricts the flare angle that can be used as there will be a constraint on the aperture diameter. The flare section design will mainly determine the physical size of the horn, the phase centre location and generation of higher modes which increases with a high rate of change of the flare angle. The ideal situation is for a long horn with very small flare angle, such that the horn behaves like an open ended corrugated waveguide. However, in most applications beamwidths and size requirements require a wide flare horn to be used. For the same aperture diameter, the directivity of the antenna increases as the flare angle is reduced.

3.2.3 Corrugation Depth

The design of the corrugations will determine the cross-polarization performance of the horn. The nominal slot depth for the balanced hybrid condition is a quarter wavelength. However, the geometry is not planar and in certain instances the optimal slot depth is found to be less than a quarter wavelength. Moreover, the slot depth will need to be designed for the whole bandwidth of operation. Fig. 3.8 shows the effect of varying the corrugation depth s at 17.25 GHz, it can be seen that the corrugation depth affects the side-lobe levels in Fig. 3.8a and the optimal slot depth is at a quarter of a wavelength (0.25λ) where cross polarization is minimum in Fig. 3.9b.

3.2.4 Number of Corrugations

As the number of corrugations are increased for a constant flare angle, the beam becomes flatter and the roll-off after the -10 dB point improves as can be seen in Fig. 3.9a.This improves the noise performance of the horn without inhibiting how efficiently the reflector is being illuminated by the horn. In Fig. 3.9b we see that there is no significant change in the level of cross-polarization as the number of corrugations are increased. As the number of corrugations are increased, the aperture diameter of the horn is effectively being increased

and directivity of the horn improves. However as can be seen from the corrugated horn design curves in Appendix A.2, the improvement in directivity becomes minimal at a certain aperture size and the horn's efficiency begins to reduce as we increase the aperture diameter.

3.2.5 Number of Corrugations per wavelength

The number of corrugations per wavelength will mainly have a significant effect on the cross-polarization performance. It's recommended that ridge-width w and the pitch p are chosen such that $\frac{\lambda}{10} \leq p \leq \frac{\lambda}{5}$ and the pitch to width ratio w/p is such that $0.7 \leq p/w \leq 0.9$. Fig. 3.10a shows the radiation patterns when the number of corrugations per wavelength are varied by changing p whilst the pitch to width ratio w/p is kept constant at 0.8. It can be seen from Fig. 3.10b that the peak cross-polarization level reduces as the equivalent number of corrugations per wavelength are increased: Note the significant difference with Fig. 3.9b where the number of corrugations are increased without altering the pitch width p. The limit of how many corrugations per wavelength can be achieved for the horn antenna will depend on the available manufacturing capabilities.

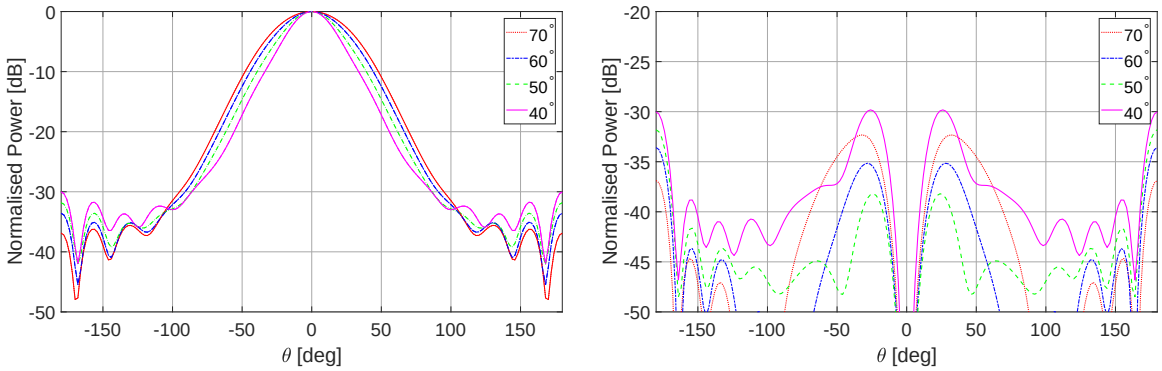

(a) E-Plane co-polar pattern.

(b) 45° plane cross-polar pattern.

Fig. 3.7 Simulated Radiation Patterns for varying flare-angle α at 17.25 GHz.

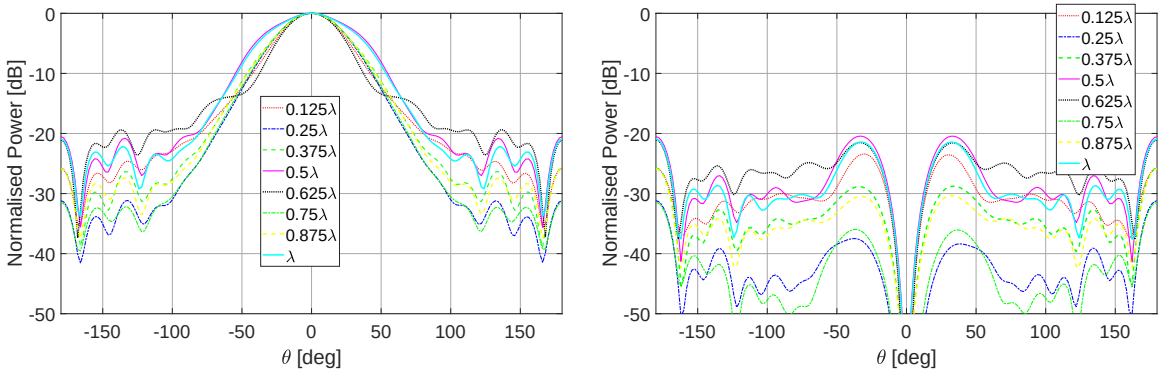

(a) E-Plane co-polar Pattern. (b) 45° plane cross-polar pattern.

Fig. 3.8 Simulated Radiation Patterns for varying corrugation depth s at 17.25 GHz.

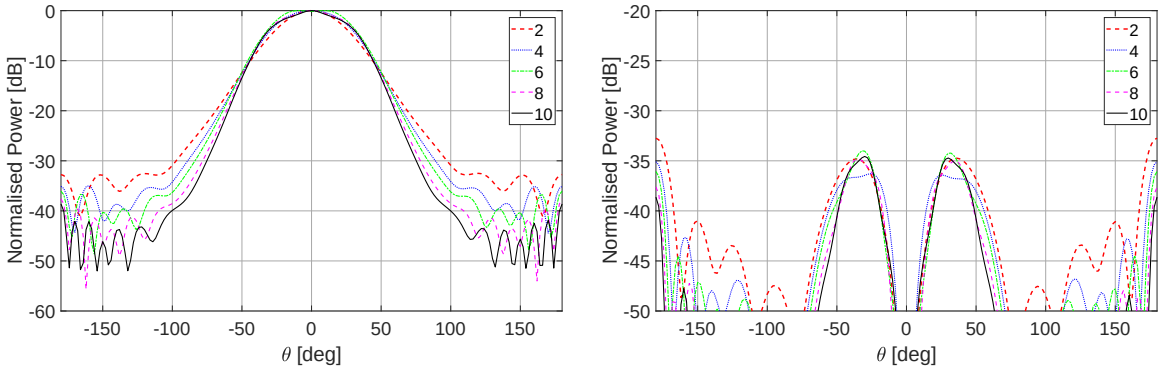

(a) E-Plane co-polar Pattern. (b) 45° plane cross-polar pattern.

Fig. 3.9 Simulated Radiation Patterns for varying number of corrugations at 17.25 GHz.

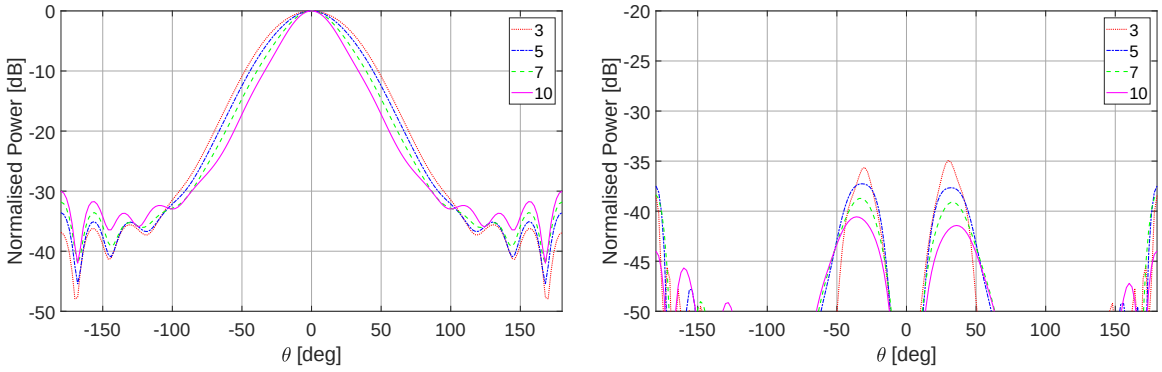

(a) E-Plane co-polar Pattern. (b) 45° plane cross-polar pattern.

Fig. 3.10 Simulated Radiation Patterns for varying number corrugation per wavelength at 17.25 GHz.

3.3 Final Design Simulation Results

3.3.1 Final Design Parameters

A wide-axially corrugated horn was designed for the specification shown in Table.3.2 using the parameter study discussed above. The main focus of the design were to achieve the lowest possible cross-polarization and the required beamwidth for the radiation pattern within the manufacturing constraints. After the required beamwidth is achieved, the corrugation parameters s and w were optimized using the internal optimizer in FEKO for cross-polarization according to Ludwig's third definition in the diagonal plane ($\phi = 45^\circ$) where cross-polarization is worst. The tooth width for antenna corrugations was constrained to a minimum of 2 mm by the manufacturer [1], which means the number of corrugations that can be achieved per wavelength is limited especially at the higher frequency limit. With a pitch p of 5.5 mm and a ridge width w of 3.5 mm, this corresponds to 2.7 corrugations per wavelength at 20 GHz. Only two corrugations were used for the design for ease of manufacture and reduced size without significantly degrading the performance of the antenna. The final parameters of the designed antenna are shown in Table. 3.3.

Table 3.3 Final Antenna Parameters

Design Parameter	**Value**
Waveguide radius– r_i	8.4 mm
Horn half-flare angle– α	60°
Corrugation width– w	3.5 mm
Corrugation pitch– p	5.5 mm
Slot depth– s	4.3 mm
Aperture radius– r_o	21.4 mm

3.3.2 Feed Section Design

A single linear polarization was desired for the antenna feed. A typical coaxial to circular waveguide feed pin would not achieve good performance for the bandwidth required for this system. As a rectangular waveguide to coaxial transition achieves wider bandwidths, a tapered circular to rectangular waveguide transition is used to feed the antenna shown in Fig. 3.11. The rectangular section of the waveguide is chosen to fit to industry standard WR-51

[1] Antenna was machined by Kline Engineering in Cape Town, South Africa.

with waveguide dimensions $a = 12.954$ mm and $b = 6.477$ mm. This operates from 14.5 to 22 GHz with a TE_{10} cut-off of 11.6 GHz. The transition converts the circular waveguide TE_{11} mode to the rectangular TE_{10} mode over the length of the transition. Performance of the transition improves as the length L is increased as shown in Fig. 3.12 which shows the input return loss for a varying length. As a trade-off between size and good return loss in the transition, L was chosen to be 30.4 mm for the final design, the simulated return loss and transmission of the feed are shown in Fig. 3.13. The return loss is better than 20 dB in the operational band.

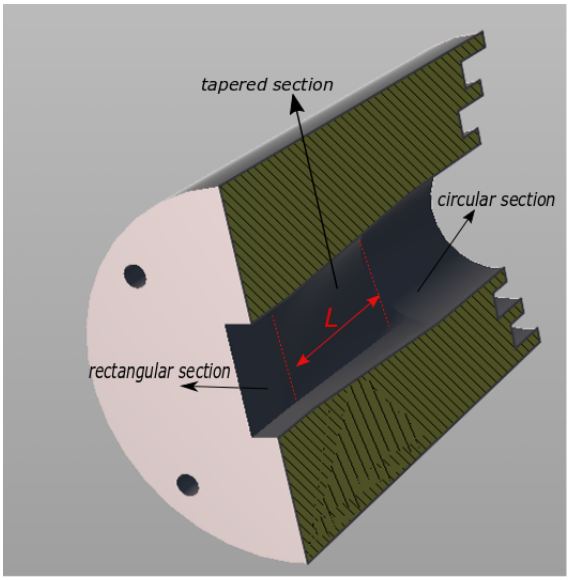

Fig. 3.11 Cross section view of tapered square to circular waveguide transition.

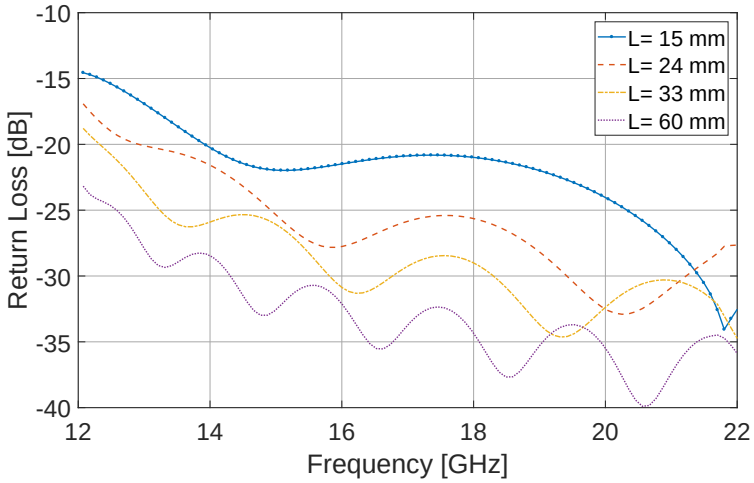

Fig. 3.12 Simulated return loss for different circular to square waveguide transition length L.

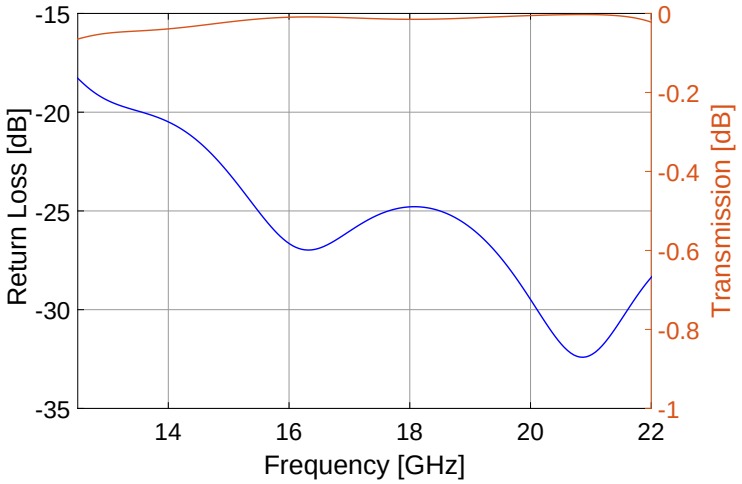

Fig. 3.13 Simulated return loss (black line) and transmission (red line) of tapered circular to square waveguide transition without antenna section.

3.3.3 Simulated Return Loss

Fig. 3.14 shows the simulated TE_{10} return loss of the antenna including the feed section discussed above. The simulated return loss is well below the specified -15 dB, a good return loss at the input of the antenna will be critical for good noise performance of system. With a standard WR-51 waveguide to coaxial adaptor specified to work from 15 to 22 GHz attached, good return loss is still expected at 14.5 GHz.

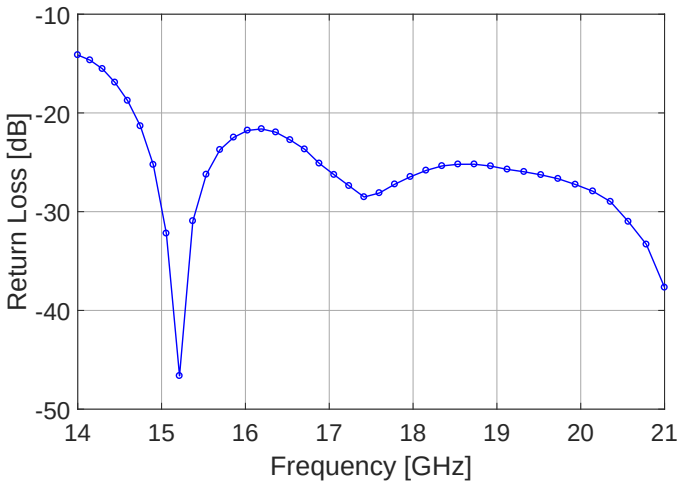

Fig. 3.14 Simulated TE_{10} return loss of antenna including tapered feed section.

3.3.4 Simulated Radiation Patterns

Fig. 3.15 shows the simulated radiation patterns of the antenna at 14.5 GHz (Fig. 3.15a), 17.25 GHz (Fig. 3.15b) and 20 GHz (Fig. 3.15c). The radiation pattern shows a fairly consistent beamwidth, with a 1.6 dB variation in half-power beamwidth. The sidelobe and cross-polarization levels are also below -30 dB. Fig. 3.16 shows a plot of the simulated half-power beamwidth and the edge taper at the half-subtended angle (48.89°). It can be seen that the beamwidth remains consistent over the frequency range and the edge taper increases slightly towards 20 GHz.

3.3.5 Phase Centre Calculation

The radiation phase centre is a point on the axis of the antenna which is the centre of curvature of the phase front [26] or the point where the antenna seems to radiate a spherical wave. For an isotropic radiator, the phase centre would be the the centre of the source. The radiated electric field for most antennas is not spherical so no such point technically exists. However, a point with the minimum change in phase for a plane and solid angle of interest is normally chosen. The apparent phase centre of an antenna will vary with frequency, plane of polarization and azimuth angle. One of the main advantages of a wide-flare angle horn such as this one is that the phase centre remains fairly constant at the apex of the antenna over a wide range of frequency. Although the phase centre location differs in the E and H plane, it will be assumed they are at the same location as the horn pattern has very low cross-polarization (symmetrical E and H plane pattern). It's important that the location of this point on the axis of the horn is known so that it's placed at the focal point of the reflector to maximise the phase efficiency discussed in section 2.4. Analytical methods for calculation of the phase centre for reflector feeds are given in [14]. For a symmetrical radiation pattern an approximate method can be used, for a solid angle region $0 < \theta < \theta_o$ in a particular ϕ-plane ($\phi = \phi_o$) the approximate phase centre location Z_{pc} can be calculated as:

$$\frac{z_{pc}}{\lambda} = \frac{\psi_{co}(0,\phi_o) - \psi_{co}(\theta_o,\phi_o)}{360(1-\cos(\theta_o))}, \tag{3.6}$$

where $\psi_{co}(\theta,\phi)$ is the co-polar field phase in degrees. In addition to the formula above, a phase centre post processing script available for FEKO obtained from Altair Connect [44] used for the estimation of the phase centre of the designed horn. For a given farfield calculation volume, the script calculates a point on the axis of the horn which will give the least deviation in the phase of the radiated field. The reference point or origin of the farfield calculation request was placed at the mouth of the horn as illustrated in Fig. 3.17.

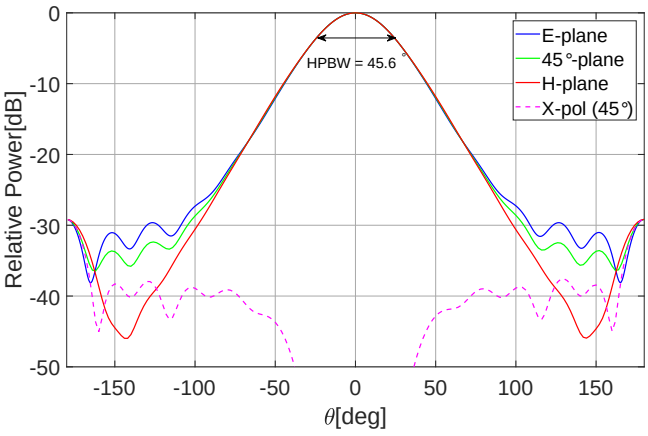

(a) 14.5 GHz

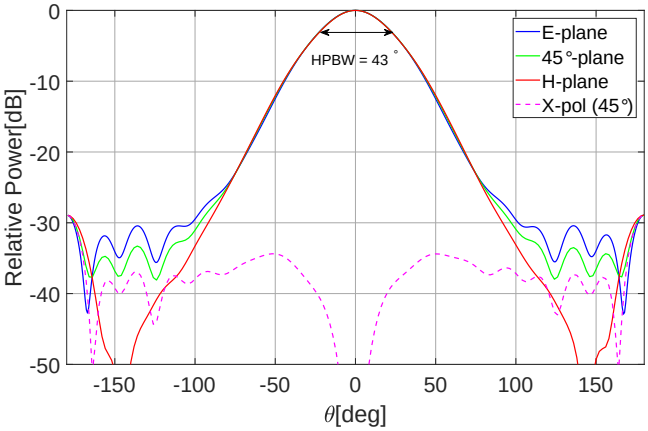

(b) 17.25 GHz

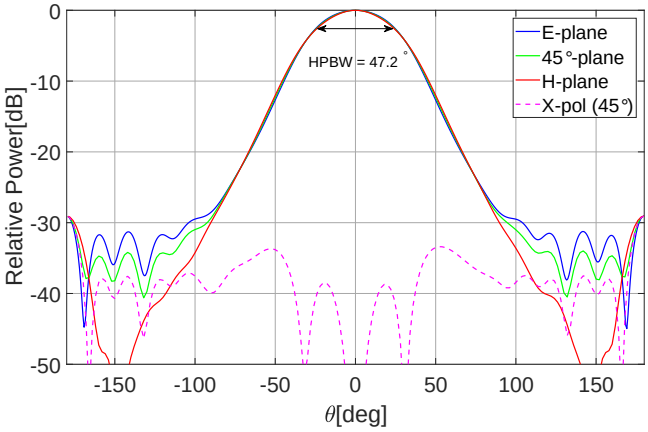

(c) 20 GHz.

Fig. 3.15 Simulated radiation patterns of feed antenna at 14.5 GHz, 17.25 GHz and 20 GHz.

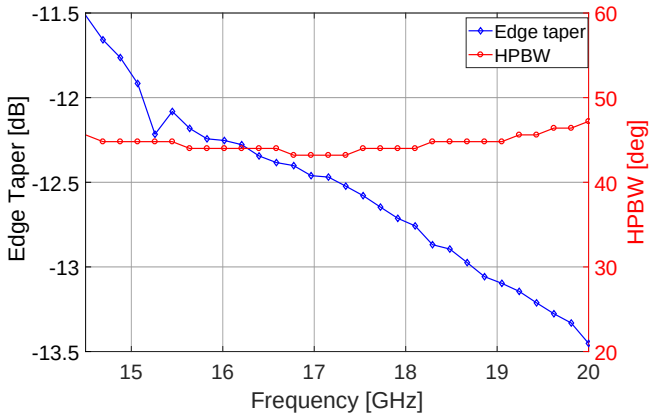

Fig. 3.16 Simulated edge taper at 48.89° and half-power beamwidth (HPBW).

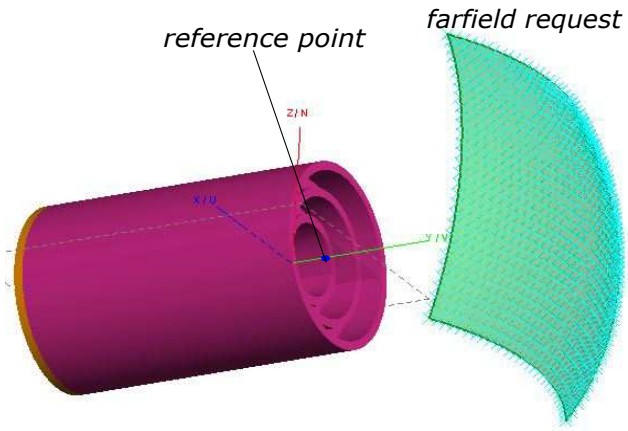

Fig. 3.17 Horn model for phase centre calculation. Farfield reference point is placed at the mouth of the horn.

The phase centre was calculated for the region $0 < \theta < 50°$ at 17.25 GHz which covers the full reflector half subtended angle. Fig. 3.19 shows a comparison of the normalised phase for the original reference point, the FEKO calculated phase centre and the phase centre calculated using (3.6). The desired response is a flat line at 0° normalised phase over the azimuth angle. The graph shows that the phase centre at -1.93 mm calculated using (3.6) gives the least deviation in phase. Fig. 3.19 shows a 3D plot of the electric field phase which gives a view of the phase change for different ϕ values. The calculated phase centre gives a less varying phase over the farfield angle considered for the calculation. The calculated phase centre of the feed can be estimated as -0.11λ, Fig. 3.20 shows the normalised phase variation in the boresight direction at 14.5, 17.25 and 20 GHz. A larger deviation in phase is observed at the lower frequency point.

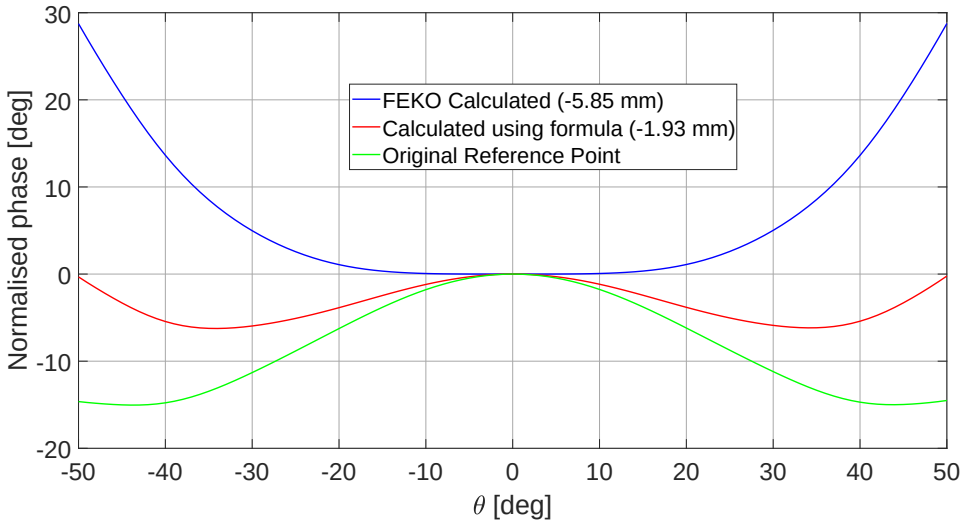

Fig. 3.18 Normalised farfield phase for different reference points in $\phi = 90^\circ$ plane at 17.25 GHz.

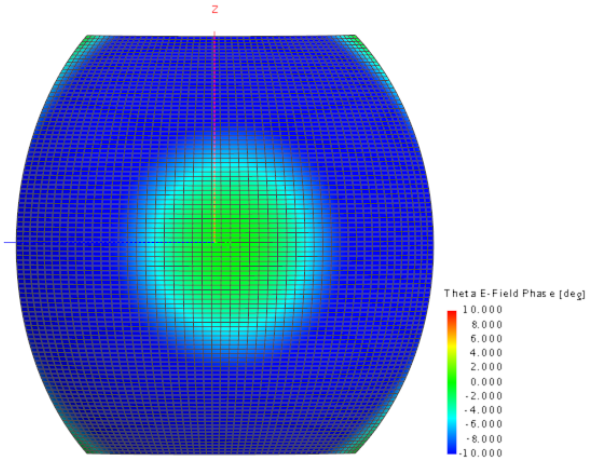

(a) Reference point (0 mm).

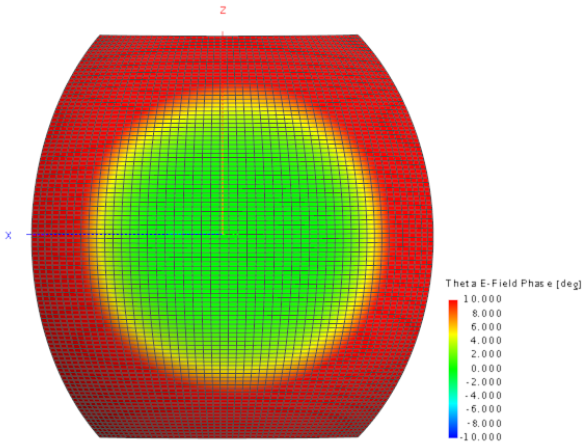

(b) FEKO calculated phase centre (-5.85 mm from reference point) .

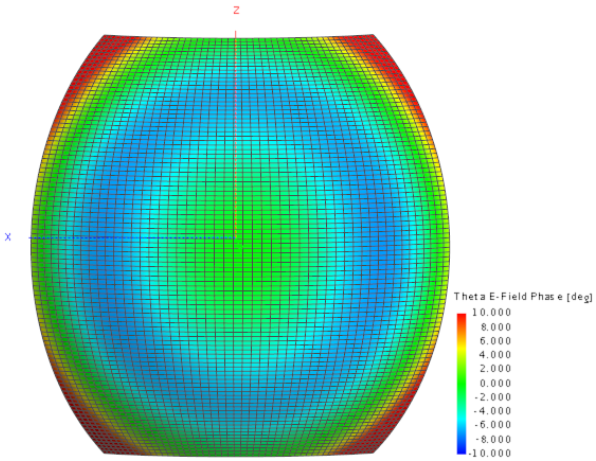

(c) Calculated using equation (3.6) (-1.93 mm from reference point).

Fig. 3.19 3D view of normalised farfield phase variation at different reference points on the horn axis simulated at 17.25 GHz.

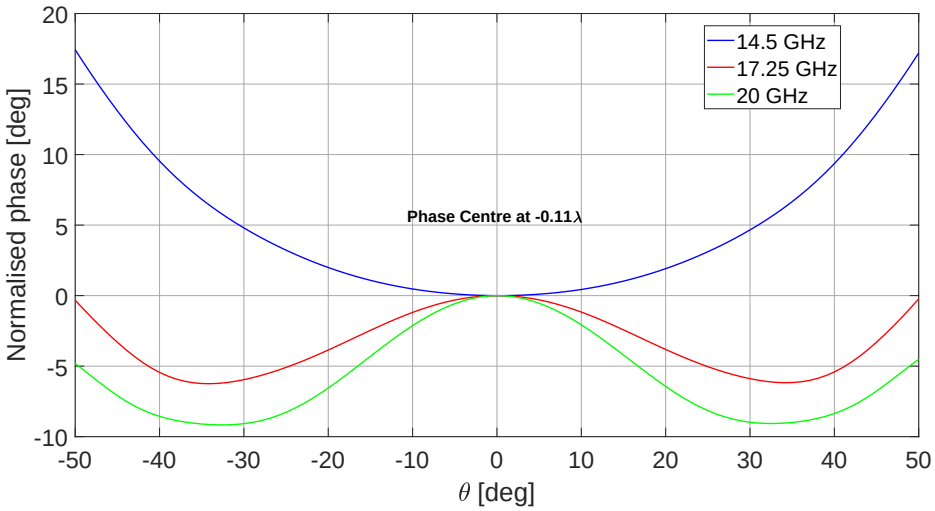

Fig. 3.20 Normalised farfield phase in $\phi = 90°$ plane for calculated phase centre at 14.5, 17.25 and 20 GHz.

3.3.6 Estimation of Aperture Efficiency

The aperture efficiency of the feed was estimated using a MeerKAT like model [2] of the dual-offset Gregorian antenna in FEKO (see Fig. 3.21). With the parameters described in Section 2.3.1, the main reflector is modelled using a parabola and the sub-reflector is modelled using a ellipsoid with the required eccentricity. As both reflectors are electrically very large, the simulation of the sub-reflector and the main reflector were performed separately using the following procedure:

- The horn antenna radiation pattern is calculated using the MoM solver and the spherical wave expansion (SWE) of the feed pattern exported.
- The horn pattern is placed on the first focal point of the sub-reflector as a source to illuminate it and the sub-reflector farfield is exported as a FEKO farfield file (ffe). The sub-reflector field is calculated using the Large Element Physical Optics (LE-PO) solver.
- The sub-reflector pattern is then placed on the second focal point as a source to illuminate the main reflector to obtain the full antenna radiation pattern. The main reflector field is calculated using Ray Launching Geometric Optics (RL-GO) solver.

With the directivity obtained from the simulation, the aperture efficiency η_{ap} can be calculated as:

[2] Not actual model of the MeerKAT used. Model created using parameters described in Section 2.3.1

$$\eta_{ap} = \frac{D_{max}\lambda^2}{4\pi A_{phy}}, \tag{3.7}$$

where D_{max} is the maximum directivity calculated from FEKO and A_{phy} is the physical area of the antenna. The calculated aperture efficiency with surface efficiency factored is shown in Fig. 3.22. The efficiency is over 60% for most of the operating band but drops slightly under 60% at the upper limits due to the much decreased surface efficiency. A full simulation of the full reflector system with a Physical Optics (PO) solver is necessary for validation of the predicted performance. However, this was not possible with the available computer hardware.

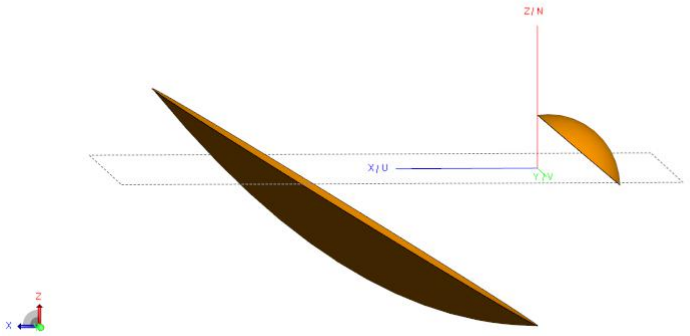

Fig. 3.21 FEKO model of MeerKAT used for aperture efficiency calculation.

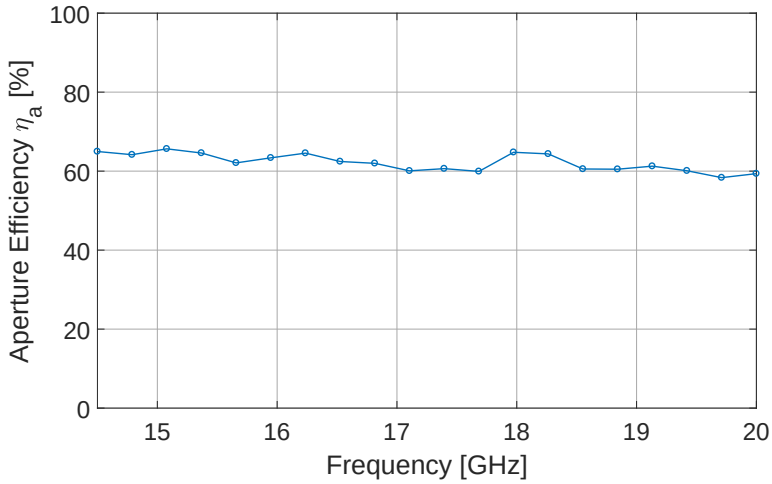

Fig. 3.22 Simulated aperture efficiency of MeerKAT like reflector fed with designed corrugated horn.

3.4 Conclusion

The design and analysis of a wide axially conical corrugated horn operating from 14.5 to 20 GHz has been presented in this Chapter. The parameter study of the antenna given in the chapter shows the dependence of the antenna co-pol pattern on the flare angle and aperture diameter whilst the design of the corrugations will determine its cross-pol performance significantly. Simulated results for the antenna show an achievable aperture efficiency of over 60% over the operational frequency range with the calculated surface efficiency factored. Measured results of the antenna show good agreement with the simulated performance, the antenna has a return loss below -15 dB and the radiation pattern is symmetric with a fairly constant beamwidth over the whole frequency band. The measured E and H-plane cross-pol patterns are also below -40 dB. In the next Chapter the manufacture and measurement results for the designed antenna are presented.

Chapter 4

Manufacture and Measurement of Feed Antenna

In the previous chapter, the design and analysis of the feed antenna was presented, in this chapter the measurement results are presented. A brief discussion on the manufacture of the feed is also given. Gain, return loss and radiation pattern measurement results are presented in the chapter.

4.1 Manufacture

The final 3D model of the antenna was drawn using SOLIDWORKS [45] and machined by Kline Engineering in Cape Town. Fig. 4.1 shows photographs of the machined horn without the WR-51 waveguide to coaxial adaptor. Aluminium was used and the antenna was silver plated for prolonged performance and resistance to corrosion. A CNC machine was used for the manufacture of the horn, the profiled circular to square waveguide transition was achieved using spark machining. Several other manufacturing processes are available for corrugated horns, but as accuracy of corrugations determine the cross-pol performance of the horns, manufacturing accuracy is critical to the design. It is common for different sections of the horn to be made separately and then joined together for large horns. Machining is normally preferred to electroforming as it produces more consistent dimensions throughout the structure, one inaccurate corrugation in the horn can excite higher order modes and completely degrade the performance of the horn [26]. Casting can also be used for low frequency horns with large dimensions for the corrugations.

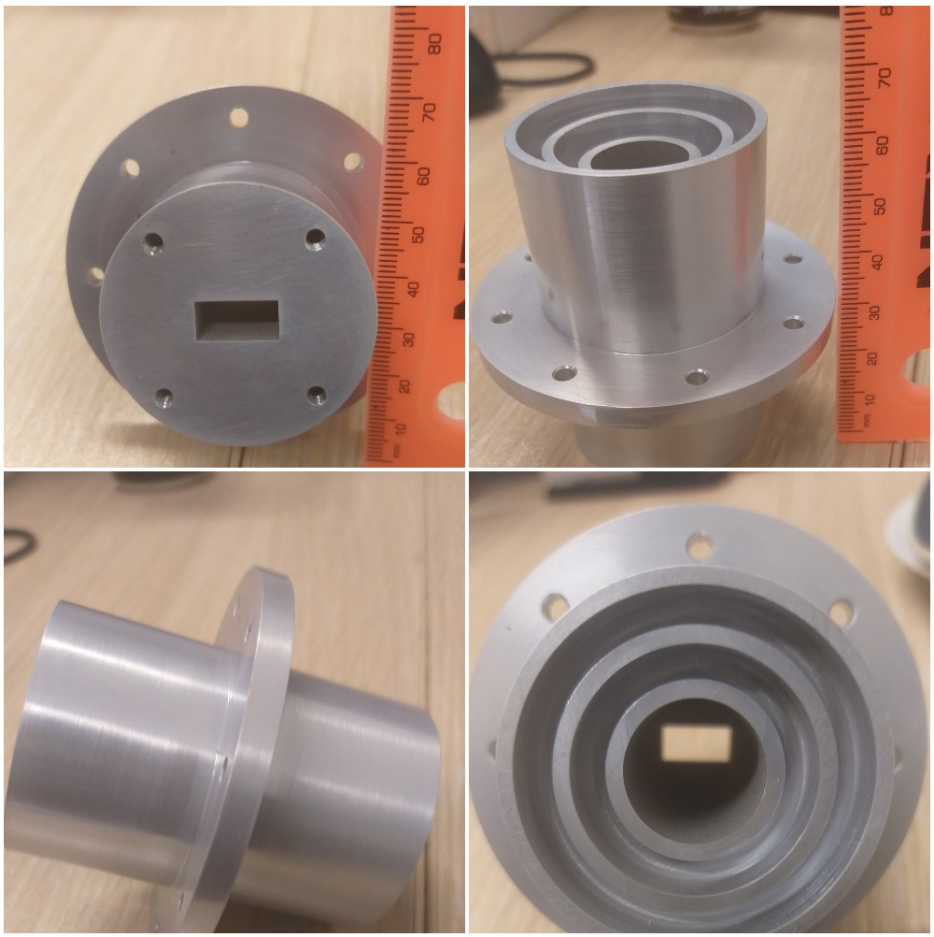

Fig. 4.1 Photographs of manufactured corrugated horn.

4.2 Measurement

4.2.1 Return Loss Measurement

The return loss of the antenna was measured using an Agilent Technologies PNA-X Network Analyzer (NS247A). Fig. 4.2 shows the measured return loss from 14 to 21 GHz with the simulated return loss shown in dotted lines. The measured return loss is below -15 dB over the band of interest from 14.5 to 20 GHz.

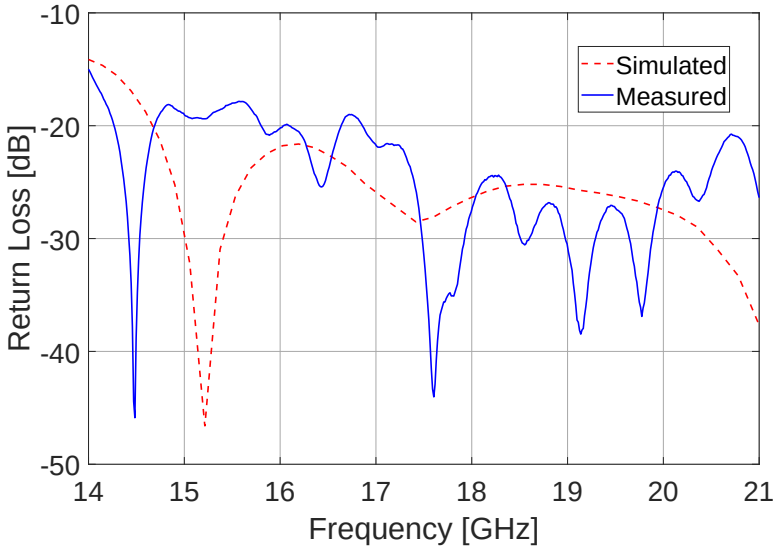

Fig. 4.2 Measured and simulated return loss of the antenna with the WR-51 waveguide adaptor.

4.2.2 Gain Measurement

The boresight gain of the antenna was measured using the three-antenna gain method. In this method, three antennas whose gain are not known are used for the measurement with the setup illustrated in Fig. 4.3:

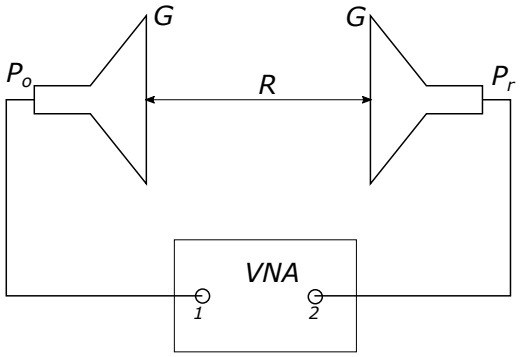

Fig. 4.3 Three antenna gain method measurement setup.

The designed corrugated horn (Axial Horn) and two other horn antennas (Ant_2 and Ant_3) were used for the gain measurement. Using the Friis transmission equation in logarithmic form, the three sets of measurements are given by [46]:

$$(G_1)_{dB} + (G_2)_{dB} = 20\log\left(\frac{4\pi R}{\lambda}\right) + 10\log\left(\frac{P_{r1}}{P_{o2}}\right), \tag{4.1}$$

$$(G_1)_{dB} + (G_3)_{dB} = 20\log\left(\frac{4\pi R}{\lambda}\right) + 10\log\left(\frac{P_{r1}}{P_{o3}}\right), \tag{4.2}$$

$$(G_2)_{dB} + (G_3)_{dB} = 20\log\left(\frac{4\pi R}{\lambda}\right) + 10\log\left(\frac{P_{r2}}{P_{o3}}\right), \tag{4.3}$$

where $G_i(i = 1,2,3)$ is the gain of the ith antenna, P_{r_j} and P_{o_j} are the power transmitted and received respectively at the jth antenna port. The ratio of the transmitted to received power between the two antennas $\frac{P_r}{P_o}$ is taken from the measured S_{21} using the VNA. All three gains of the antennas can then be solved using:

$$\begin{bmatrix} G_1 \\ G_2 \\ G_3 \end{bmatrix} = \begin{bmatrix} 1 & 1 & 0 \\ 1 & 0 & 1 \\ 0 & 1 & 1 \end{bmatrix}^{-1} \begin{bmatrix} G_1 + G_2 \\ G_1 + G_3 \\ G_3 + G_2 \end{bmatrix} \tag{4.4}$$

The calculated gains for the antennas are shown in Fig. 4.4. The AUT measured gain corresponds closely with simulation results with a flat gain of about 12 dB across the operational band. However, the measurement shows ripple after 19 GHz due to mismatch as the antenna chamber is only rated up to 18 GHz.

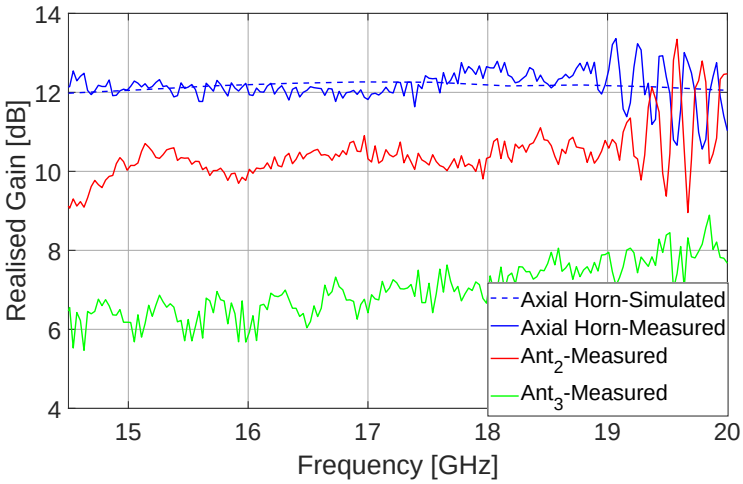

Fig. 4.4 Measured and Simulated gain of antenna using three gain method showing calculated gain of all three antennas including manufactured horn.

4.2.3 Radiation Pattern Measurement

The radiation patterns were measured at Stellenbosch University's indoor antenna testing range in the Department of Electrical and Electronic Engineering. A spherical near-field measurement was taken in the anechoic chamber with the setup shown in Fig. 4.5. The probe used for the measurement is a WR-62 waveguide probe which operates from 12.4 to 18 GHz, the VNA used is a PNA-X 5242A which can operate up to 26.5 GHz. In the measurement setup, the probe is fixed for different polarizations y and x whilst the antenna under test moves for different ϕ and θ points. The E-plane ($\phi = 0°$) and H-plane ($\phi = 90°$) pattern cut measurements were taken. The co-pol pattern scan is taken with the probe polarization oriented in the same plane as the antenna and the cross-pol pattern scan is taken with the probe polarization orthogonal.

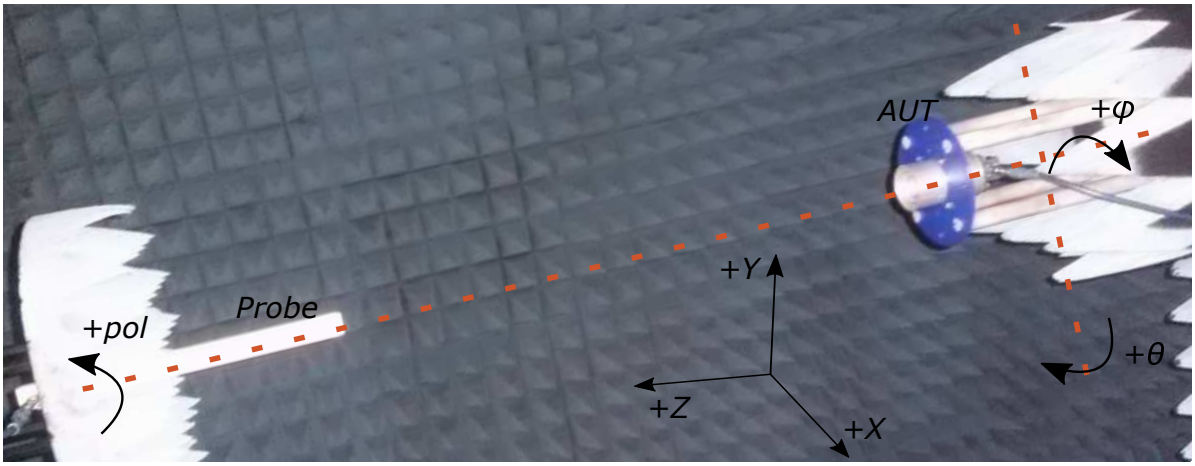

Fig. 4.5 Anechoic chamber coordinate system and measurement setup.

Measurements were carried out at 29 frequency points from 14.4 to 20 GHz, the measured E- and H-plane co-pol patterns are shown in Fig. 4.6. It can be seen from the figures that the measured results closely agree with the simulated radiation patterns showing symmetrical E- and H-Plane at the three frequencies. The HPBW varies from 43° at 14.4 GHz to 52◦ at 20 GHz. The measured against simulated E- and H-plane cross-pol patterns are also shown in Fig. 4.7. The cross-polarization is below -40 dB in both planes as expected.

The measured beamwidth is relatively consistent over the frequency range as can be seen from the measured and simulated HPBW and edge taper shown in Fig. 4.8a and Fig. 4.8b respectively. The measured HPBW varies more than the simulated results particularly at the higher frequency limit. The edge taper varies from -11.8 to -13.2 dB.

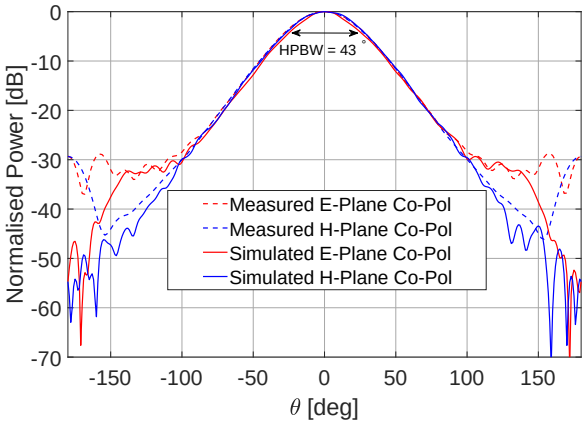

(a) 14.4 GHz

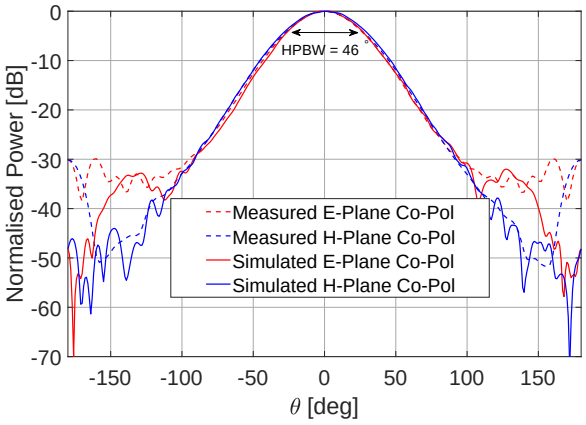

(b) 17.2 GHz

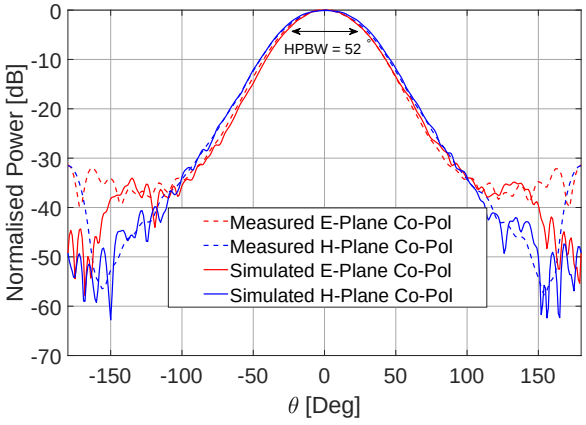

(c) 20 GHz.

Fig. 4.6 Measured E-Plane and H-Plane radiation patterns.

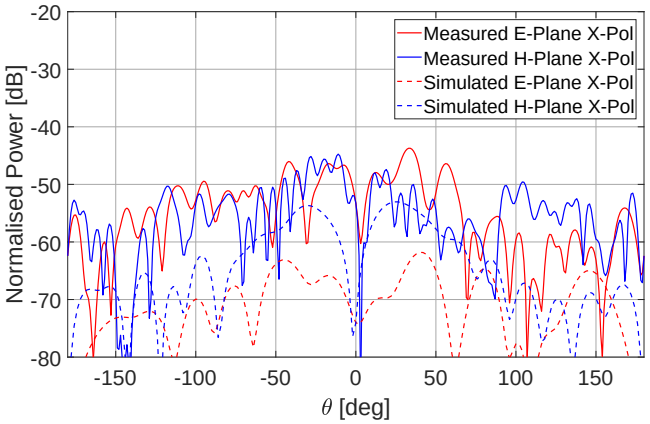

(a) 14.4 GHz

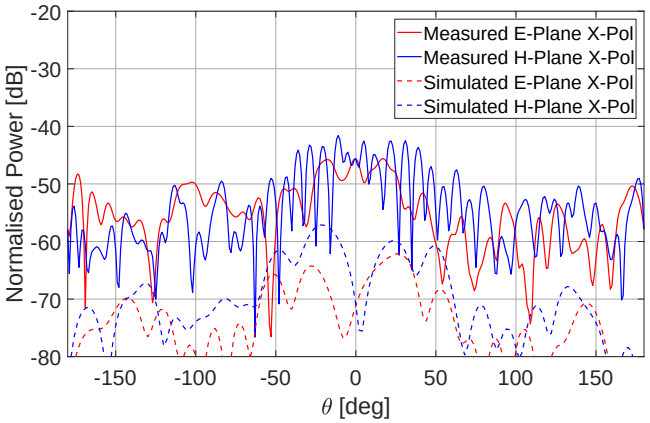

(b) 17.2 GHz

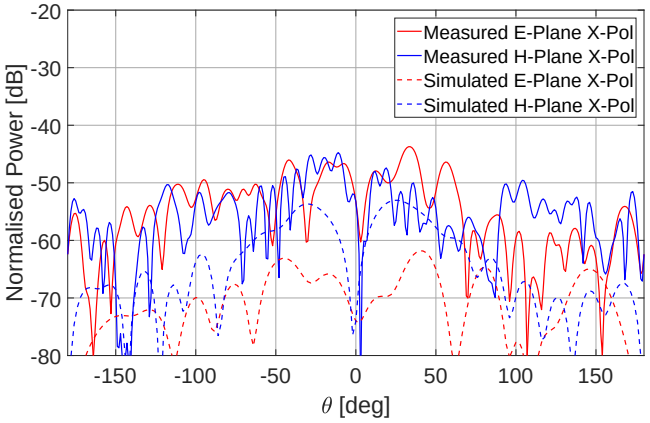

(c) 20 GHz.

Fig. 4.7 Measured and Simulated E-Plane and H-Plane relative Cross-pol radiation patterns.

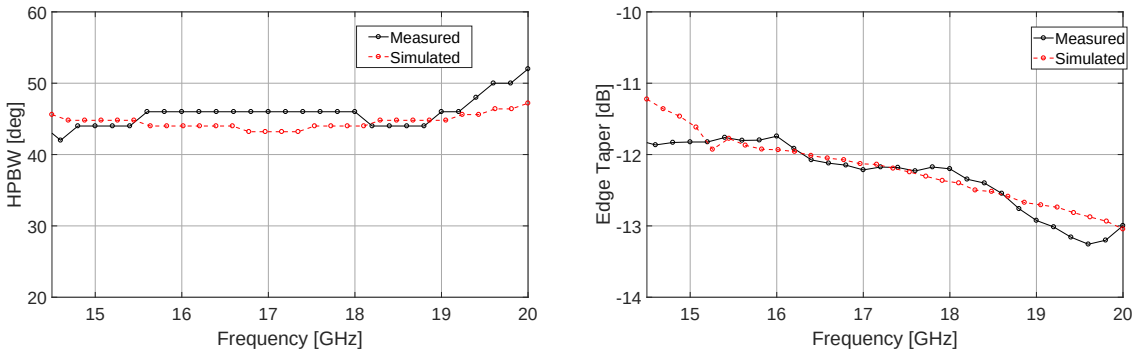

(a) Measured and simulated half-power beamwidth (HPBW).

(b) Measured and Simulated edge taper at half-subtended angle $\theta_e = 48.89°$.

Fig. 4.8 Measured and simulated half-power beamwidth and edge taper.

4.3 Conclusion

The measurements results presented in the chapter show very good agreement with the simulation results. The antenna achieves a return loss better than -15 dB in the operational band (14.5 to 20 GHz) and a gain of 12 dB in the boresight direction. The radiation pattern measurements show a symmetrical E- and H-plane pattern as desired and a low cross-polarization lower than -40 dB in the two planes. The measured edge taper for the antenna is within 2 dB of the targeted -12 dB at the edge of the sub-reflector. In the next chapter, the analysis and design of the RF front-end receiver for the system is discussed.

Chapter 5

Front-end Receiver Design

The front-end receiver of a radio telescope has an important role to play in the system performance of the telescope. The front-end receiver conditions the signals received from the antenna for processing in the system back-end. The receiver amplifies the small signals received from the feed, filters and down-converts the signals to a lower frequency which can be suitably sampled by the ADC. It's necessary for the front-end to perform this function whilst adding minimal noise to the received signal. Analogue signal conditioning hence becomes a critical component in the telescope receiver as the science drive demands wide bandwidths and highly sensitive receivers. The advancement in digital signal processing has helped push the boundaries in terms of eliminating down-converting stages in the receiver chain with the development of high-speed ADCs.

This chapter describes the design of the front-end receiver operating from 14.5 to 20 GHz to be used for the concept demonstrator. A general overview of front-end receivers and some theory will be presented in the first section. The receiver uses one mixing stage to downconvert the RF input to 4.5 GHz IF with an instantaneous bandwidth of 2.5 GHz to be bandpass sampled in the second Nyquist zone. Details of the design and discussion on specific components of the receiver are then presented together with system simulation results.

5.1 Introduction to Receivers

5.1.1 Direct-Sampling Receiver

The basic function of a receiver is to amplify the received RF signal and filter it before digital sampling. A direct-sampling receiver is shown is in Fig. 5.1.

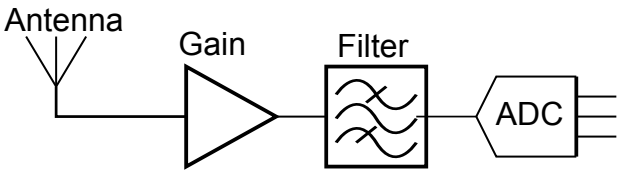

Fig. 5.1 Direct sampling receiver.

In this architecture, the signal is amplified and the filter selects what band signal is being allowed. Several filters can be used in parallel to create a channelised receiver. This topology is however not practical for certain applications as the filters would be unrealisable or the signal frequency may be too high to be sampled by the ADC without aliasing. However, direct-sampling is becoming more popular in modern receiver applications as ADC sampling rates are being improved on. For example, Analogue devices recently introduced an RF ADC (AD9213) that can sample at 10 GSPS [47]. Direct-sampling has the advantage of having less components in the signal path which improves sensitivity and selectivity of the receiver.

5.1.2 Super-heterodyne Receiver

By using a mixer, the RF signal in a receiver can be down-converted to a desired IF signal which can be easily sampled by the ADC as shown in Fig. 5.2. This is called a super-heterodyne receiver.

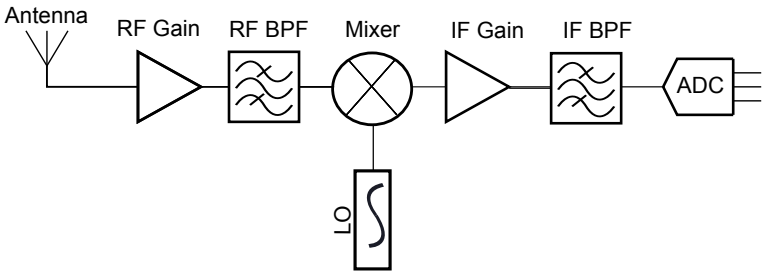

Fig. 5.2 Superheterodyne receiver.

It's often desired for the frequency to be translated to a lower frequency for sampling and cheaper components for filtering and amplification. A mixer is a three-port device that uses a nonlinear or time-varying element to achieve frequency conversion [48]. The mixer ports are LO(local oscillator), RF (radio frequency) normally the input in the receiver and the IF (intermediate frequency) the desired output. An ideal mixer produces the difference and the sum of the input frequencies as illustrated in Fig. 5.3 and Fig. 5.4 for up-conversion and down-conversion respectively.

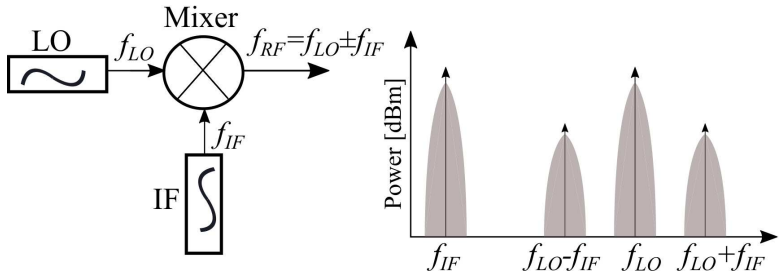

Fig. 5.3 Mixer up-conversion.

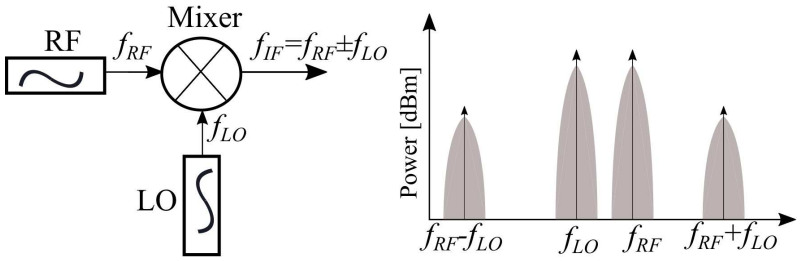

Fig. 5.4 Mixer down-conversion.

The up-conversion case of course typically applies to transmitters so the focus of this discussion will be on the down-conversion application in receivers. The time (t) varying RF input signal v_{RF} can be represented as given in [48]:

$$v_{RF}(t) = \cos 2\pi f_{RF} t. \tag{5.1}$$

The output of the mixer at the IF port when the LO signal $\cos 2\pi f_{LO} t$ is applied is given as

$$v_{IF}(t) = \frac{K}{2}\left[\cos 2\pi (f_{RF} - f_{LO})t + \cos 2\pi (f_{RF} + f_{LO})t\right], \tag{5.2}$$

where K is a constant that represents the conversion loss. For down-conversion the desired IF becomes:

$$f_{IF} = \mid f_{RF} - f_{LO} \mid . \tag{5.3}$$

It can be seen from (5.3) that there are two choices for the LO frequency. It can either be higher or lower than the RF frequency by the IF frequency referred to as **High-Side Tuning** and **Low-Side Tuning** respectively. The choice between the two options will depend on several factors such as cost of the oscillator or spurious performance. Higher frequency oscillators are more expensive.

5.1.3 Image Frequency

Unfortunately, the input to the receiver consists of other frequencies besides the desired RF frequency that may mix down to the same IF. From the mixer equation (5.3), there will be two solutions to f_{RF}:

$$f_{RF} = f_{LO} \pm f_{IF}. \tag{5.4}$$

For the low-side tuning case, the RF signal is the solution higher than the LO i.e $f_{LO} + f_{IF}$. The other solution is the image frequency f_{IM} defined as:

$$\begin{aligned} f_{IM} &= f_{LO} - f_{IF} \\ &= (f_{RF} - f_{IF}) - f_{IF} \\ &= f_{RF} - 2f_{IF}, \end{aligned} \tag{5.5}$$

Fig. 5.19 shows the location of the image frequency for low-side tuning. For high-side tuning the image signal is represented as:

$$f_{IM} = f_{RF} + 2f_{IF}. \tag{5.6}$$

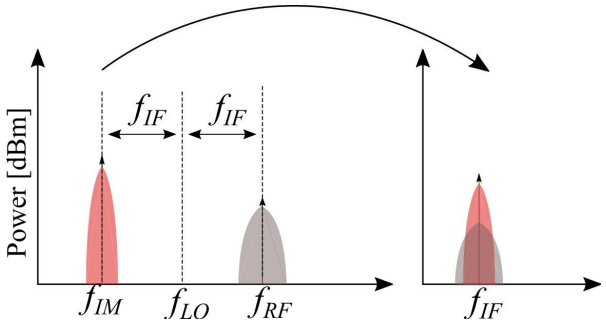

Fig. 5.5 Image frequency.

5.1.4 Selecting the IF

The choice of the IF frequency has significant implications on the design of the receiver particularly the image rejection capability of the system and its selectivity. From (5.5) and (5.6) it was shown that the image frequency is away from the RF signal by $2f_{IF}$ hence a higher IF frequency gives an image frequency further away from the RF frequency. A trade-off needs to be met between having a low enough IF for easy digitization, lower component

costs or high enough IF for easier image rejection as the image frequency is further away from the input RF for the RF filter to attenuate it. Fig. 5.6 and Fig. 5.7 illustrates the low IF and high IF scenario respectively.

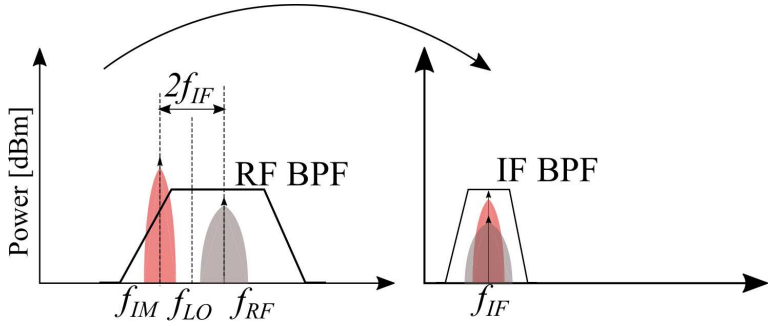

Fig. 5.6 Low IF frequency conversion.

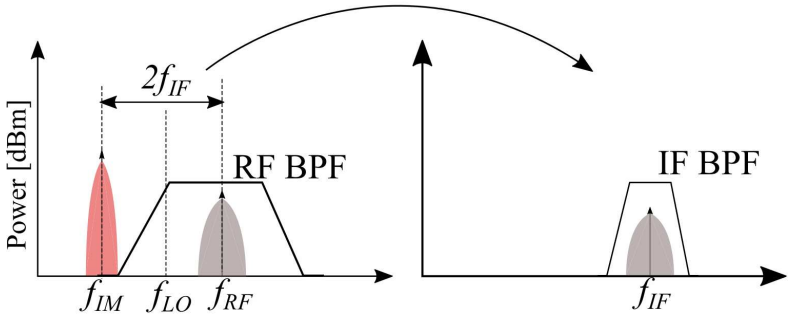

Fig. 5.7 High IF frequency conversion.

It can be seen from Fig. 5.7 that the higher IF will be easier for the image reject filter to attenuate the image frequencies however the higher IF will require a higher sampling rate and a more difficult IF filter realisation with a higher Q-factor [1] than in the low IF case.

5.1.5 Dual Down-Conversion Receiver

A solution to the low and high IF trade-off is the dual-downconversion topology shown in Fig. 5.8. A higher first IF is chosen primarily for image rejection then a second IF stage is used for better selectivity. IF BPF1 will be easier to implement when the first IF stage is high and IF BPF2 can be used for selectivity.

[1] Unloaded Q-factor of a bandpass filter is calculated by the ratio of its centre frequency to the bandwidth $f_c/\Delta f$. Higher Q filters are more expensive and difficult to design.

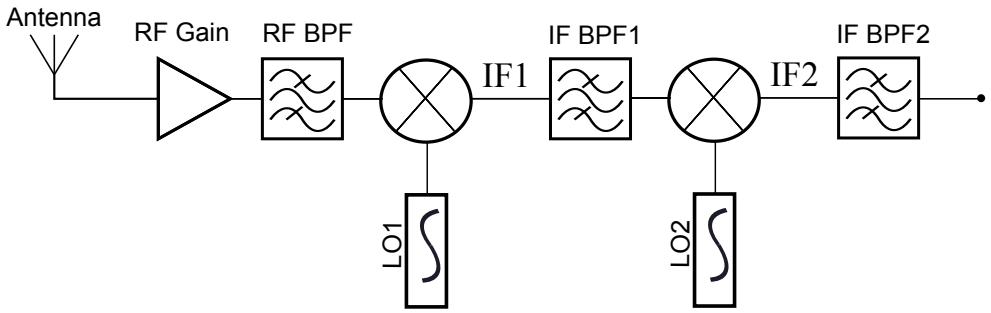

Fig. 5.8 Dual down-conversion receiver.

5.1.6 Homodyne Receiver

Another solution to the image frequency problem is the homodyne architecture which is sometimes called the zero-IF architecture shown in Fig. 5.9. The LO frequency is chosen such that it's equal to the RF frequency thereby mixing down to baseband as illustrated in Fig. 5.10. The main advantage of this simple architecture is there is no need for a bandpass filter as a simple low-pass filter can be used to select the baseband signal.

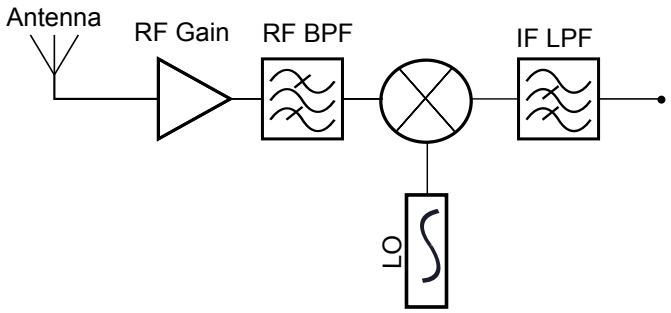

Fig. 5.9 Homodyne receiver.

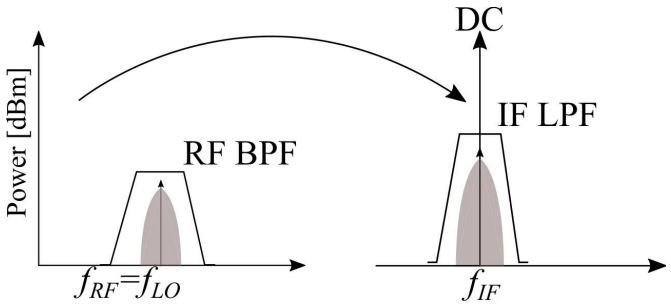

Fig. 5.10 Down-conversion to baseband in homodyne receiver.

Other solutions to image frequency cancellation are the use of Image Reject mixers or preselector filter banks before the mixer. The image reject mixer uses two mixers with two

quadrature hybrids at the input and the output to obtain two IF outputs from the wanted band and the unwanted image band. Another alternative particularly in a wide bandwidth application is to use a bank of preselector filters to channelize the input RF into smaller bandwidths thereby allowing the selection of a lower IF frequency.

5.1.7 Receiver Noise

The minimum signal that can be detected by the receiver will predominantly be determined by the noise performance of the receiver. Sources of noise can be generated internally due to random motion of charges in devices and materials [48] or external sources such as the cosmic microwave background (CMB), wireless devices, thermal noise from the ground and lightning. The noise in the receiver can be represented by considering the random voltage generated by a noisy resistor R. The RMS voltage generated across the noisy resistor can be represented by [48]:

$$V_n = \sqrt{4kTBR}, \tag{5.7}$$

where k is the Boltzmann's constant ($1.38 \times 10^{-23} J/K$), T is the temperature in degrees Kelvin, B is the bandwidth in Hz and R is the resistance in Ω. By considering a load resistor R for maximum power transfer as illustrated in Fig. 5.11, the maximum available noise power P_n at a given bandwidth and temperature is given by (5.8).

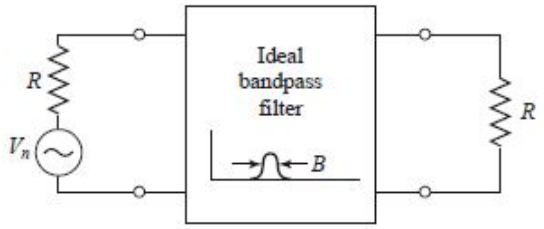

Fig. 5.11 Thevenin equivalent circuit of a thermal noise source [48].

$$P_n = kTB. \tag{5.8}$$

5.1.8 Noise Factor

Noise Factor is a measure of the degradation of the signal-to- noise ratio (SNR). SNR is the ratio of the desired signal to the noise power. A non ideal system such as a receiver will add noise to the input signal thereby degrading the SNR. The Noise Factor F is calculated using:

$$F = \frac{SNR_{in}}{SNR_{out}}, \tag{5.9}$$

where SNR_{in} and SNR_{out} are the input and output SNR respectively. It can equally be specified as **Noise Figure (NF)** in logarithmic form:

$$\text{NF} = SNR_{in_{dB}} - SNR_{out_{dB}}. \tag{5.10}$$

The noise of the receiver can also be specified as an equivalent temperature T_e. From (5.8), the equivalent noise temperature T_e that gives a given noise power P_n can be defined. The equivalent noise temperature can be calculated from the noise factor using:

$$T_e = (F-1)T_o, \tag{5.11}$$

where T_o is the room temperature (290 K).

5.1.9 Cascaded System Noise Factor

If the cascaded system shown in Fig. 5.12 consisting of three amplifiers with different Noise Figures and gains is considered, the cascaded noise factor F_{cas} can be calculated is calculated using (5.12).

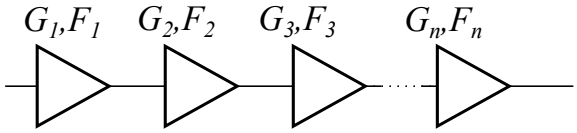

Fig. 5.12 Cascaded System.

$$F_{cas} = F_1 + \frac{F_2 - 1}{G_1} + \frac{F_3 - 1}{G_1 G_2} + ... + \frac{F_n - 1}{G_1 G_2 ... G_n - 1} \tag{5.12}$$

By observing (5.12), it can be seen that for low cascaded noise factor we require the first stage of the system to be low-noise and high gain as it has the most effect on the cascaded noise and reduces the second stage's noise contribution with its gain. In noise sensitive systems such as radio astronomy receivers, it is therefore necessary that the first stage in the front-end is an LNA.

5.2 Receiver Design

5.2.1 Initial Requirements

The initial front-end requirements for the receiver are described in Table 5.1. The instantaneous bandwidth of 2.5 GHz was chosen as this is the specified bandwidth for the SKA1-MID science requirement [49]. The linearity and noise performance of the system were designed for best effort based on readily available components. A single mixing stage was selected for the system to limit number of components in the chain.

Table 5.1 Front-end Receiver Initial Requirements.

Parameter	Specification
Frequency Range	14.5 to 20 GHz
IF	4.5 GHz
Instantaneous Bandwidth	2.5 GHz
Channels	Single

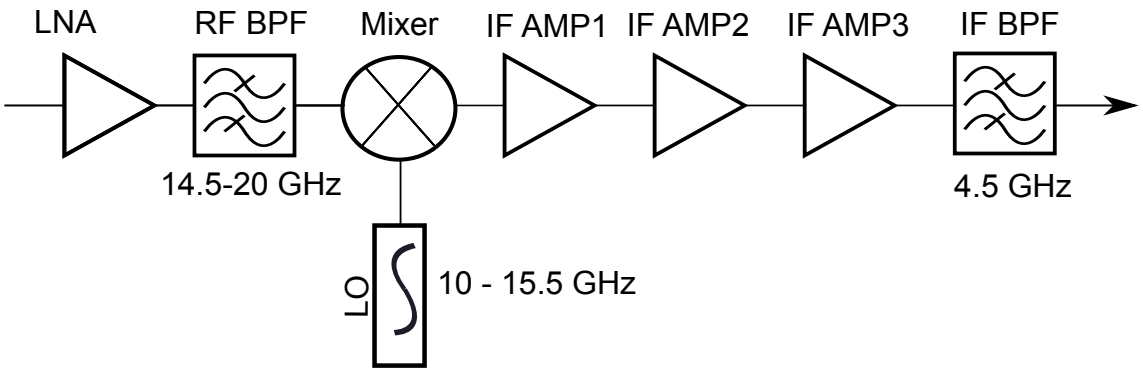

Fig. 5.13 Receiver block.

5.2.2 Frequency Plan

The single down-conversion scheme frequency plan for the receiver is illustrated in Fig. 5.14. A tuned LO is used to mix down the RF input to the 4.5 GHz IF using low-side tuning. The LO will be tuned 4.5 GHz below the desired RF input frequency.

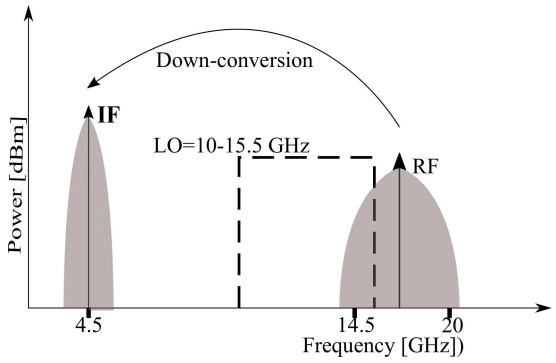

Fig. 5.14 Frequency plan for down-conversion.

5.2.3 Mixer Spurious Analysis

The mixing stage of the receiver was analysed for spurious threats for the RF and IF frequency range using AWR Visual System Simulator (VSS). As the mixer is a non-linear device, the output at the IF port includes intermodulated products of the LO and the RF input frequencies. The mixer output is mathematically represented as:

$$f_{IF} = nf_{LO} \pm mf_{RF}, \tag{5.13}$$

where m and n are integers, $m = 1$ and $n = 1$ is of course the desired second order mixer output. The different combinations can be easily viewed with the aid of spur chart for a particular input and output. The RF planning tool in AWR VSS was used for an initial assessment of threatening spurs for the 4.5 GHz IF and RF input of 14.5 to 20 GHz. Fig. 5.15 shows the spur chart plotted from AWR VSS. The red box indicates the IF frequency range of interest. The two diagonal lines marked with a square in the plot are the wanted IF ($m = 1, n = 1$). The lowest order spur (marked with a circle) that will be within the IF band is the ($m = 1, n = 2$) i.e $2f_{LO} - f_{RF}$ spur which will fall within the IF band. It was therefore critical to take note of the suppression of this spur during the mixer selection process. A double balanced mixer MM1-0626H [50] from Marki microwave was selected for the system. Double balanced mixers only have odd m and n products at the IF port [51]. They also have an advantage of excellent isolation between the LO and RF ports which will be critical in this application as the frequency range of the LO (10-15.5 GHz) and RF (14.5 to 20 GHz) intersect. The key specifications for the MM1-0626H mixer are shown in Table 5.2.

The mixer spurious performance was simulated using file based behavioural mixer model in AWR VSS shown in Fig. 5.16. The spur table in the mixer datasheet [50] is used as a file input in the model to calculate the expected suppression of the spurs. The LO was changed in steps of 0.5 GHz from 10 to 15.5 GHz to view the spur levels expected for the mixer in

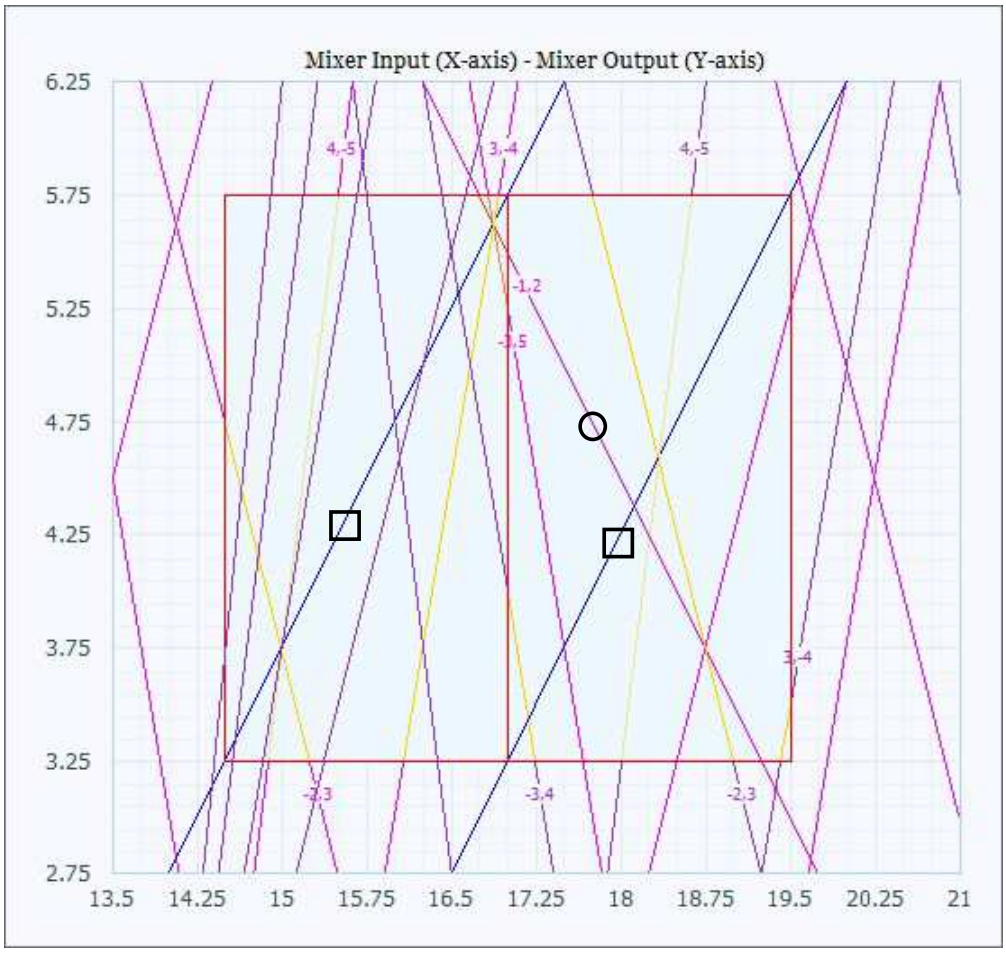

Fig. 5.15 Spur Chart: Axes are in GHz, lines with square box represent the desired IF, line marked with circle represents the third order output $2f_{LO} - f_{RF}$.

Table 5.2 MM1-0626H mixer specification.

Parameter	**Specification**
RF/LO range	6 - 26.5 GHz
IF range	DC- 9 GHz
Conversion Loss	7.5 dB
LO-RF Isolation	47 dB
LO-IF Isolation	34 dB
RF-IF Isolation	35 dB
Input 1 dB Compression	9 dBm
Third order intercept point	21 dBm

the whole tuning range. The simulated mixer output is shown in Fig. 5.17. It can be seen that for an RF input of -10 dBm and LO power of 15 dBm, the third order mixer products

$2f_{LO} - f_{RF}$ will be 31 dBc with reference to the IF power. The other mixer products are further suppressed and therefore should not be of concern. A test was also carried to assess the spurious performance when high side tuning is used instead. The LO was tuned from 18.5 to 24.5 GHz to obtain the output shown in Fig. 5.18. It is clear that the spurious performance improves for high side tuning. The only mixer spur that falls within the IF band is the 5th order spur $3f_{RF} - 2f_{LO}$. However, low side tuning was selected for this application to take advantage of the waveguide high pass response which attenuates the image frequency for the band. Furthermore, high side tuning would require a more expensive oscillator for the LO signal as it's at a much higher frequency.

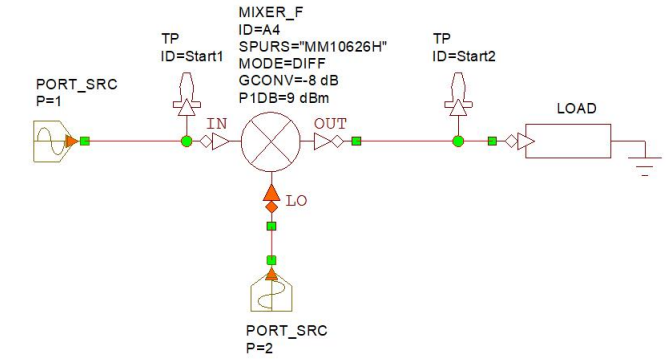

Fig. 5.16 AWR VSS model of Mixer.

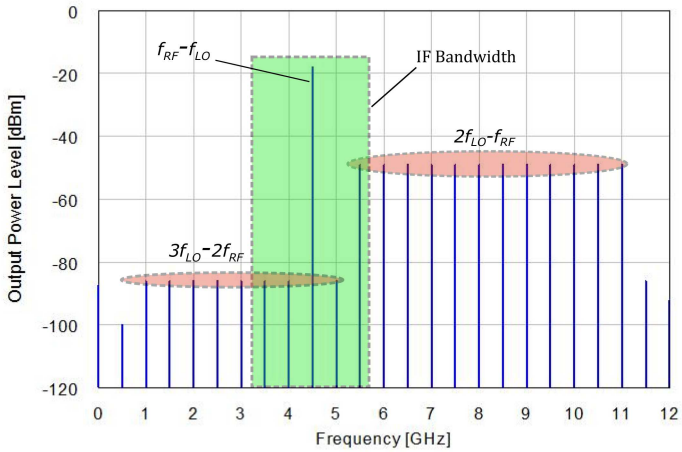

Fig. 5.17 Simulated mixer output with spur table for low side tuning.

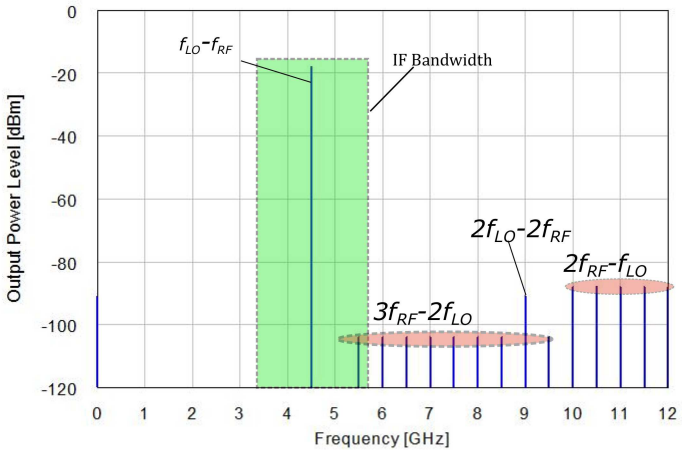

Fig. 5.18 Simulated mixer output with spur table for high side tuning.

5.2.4 Image Rejection Filter

As a discussed in Section 5.1.3, the image frequencies will pose a threat to the selectivity of the system. For low side tuning which will be used in this case, the image frequency range (f_{IM_L} to f_{IM_H}) can be calculated as:

$$\begin{aligned} f_{IM_H} &= f_{RF_{high}} - 2f_{IF_{centre}} + f_{IF_{BW}} \\ f_{IM_L} &= f_{RF_{low}} - 2f_{IF_{centre}} - f_{IF_{BW}}, \end{aligned} \tag{5.14}$$

where $f_{RF_{low}}$ to $f_{RF_{high}}$ is RF frequency range, $f_{IF_{centre}}$ is the centre frequency of the IF and $f_{IF_{BW}}$ is the IF bandwidth. Fig 5.19 shows the location of the image frequency with respect to the RF frequency range. The input bandpass filter will need to have a steep enough attenuation slope between 12.25 GHz and 14.5 GHz to reject the image band.

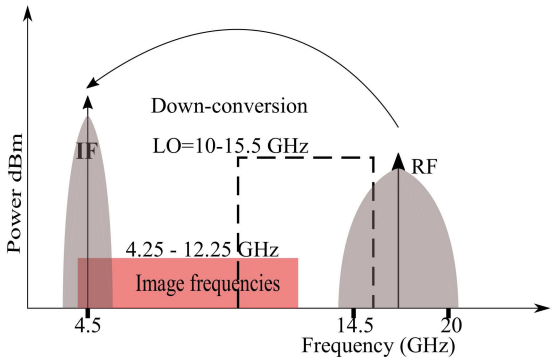

Fig. 5.19 Image frequency range for downconversion.

The image rejection filter requirements are shown in Table 5.3. Its main function are to attenuate the image band as discussed above as well as limit intermodulation products

as a result out of band RF inputs mixing with the LO frequency. For this high frequency, a waveguide filter is normally desired due to high dielectric losses but a planar microstrip filter was custom designed for this application for lower cost and a portable design. A distributed band-pass filter was designed for the system in [9] by Tauriq Latief for an undergraduate final-year project. The filter uses quarter-wavelength short circuit stubs with slots implemented to improve the return loss of the filter and suppress spurious signals in the stopband. The 6th order filter was designed on 0.211 mm Mercurywave 9350 low loss substrate [52], a photograph of the manufactured filter is shown in Fig. 5.20. The simulated and measured results for the filter are shown in Fig. 5.21. The filter had a minor frequency shift and the insertion loss of the filter was below the 2 dB specification. However, the filter achieves more than 40 dB image rejection and has a return loss better than 15 dB in most of the passband.

Table 5.3 Image reject filter specification.

Parameter	**Specification**
Passband	14.5-20 GHz
Insertion loss	$\leq$2 dB
Return loss	$\geq$ 10 dB
Image band	4.25 - 12.25 GHz
Image rejection	$\geq$ 30 dB

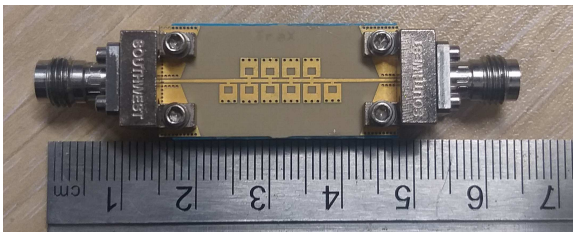

Fig. 5.20 Manufactured Image reject filter designed by Tauriq Latief [9].

5.2.5 Bandpass Sampling

For normal oversampling or baseband sampling of the 4.5 GHz IF frequency, the minimum sample rate that can be used without distortion due to aliasing is 11.5 GSPS i.e twice the maximum frequency if the Nyquist Theorem is to be met [53]. Sampling at this high frequency would be impractical and expensive, therefore bandpass sampling will be used for this system. The digital domain sampled signal replicates in intervals referred to as Nyquist zones as illustrated in Fig. 5.22. In bandpass sampling, the sampling rate is chosen such that the replicas do not overlap. In this case the minimum sampling rate used is twice the signal

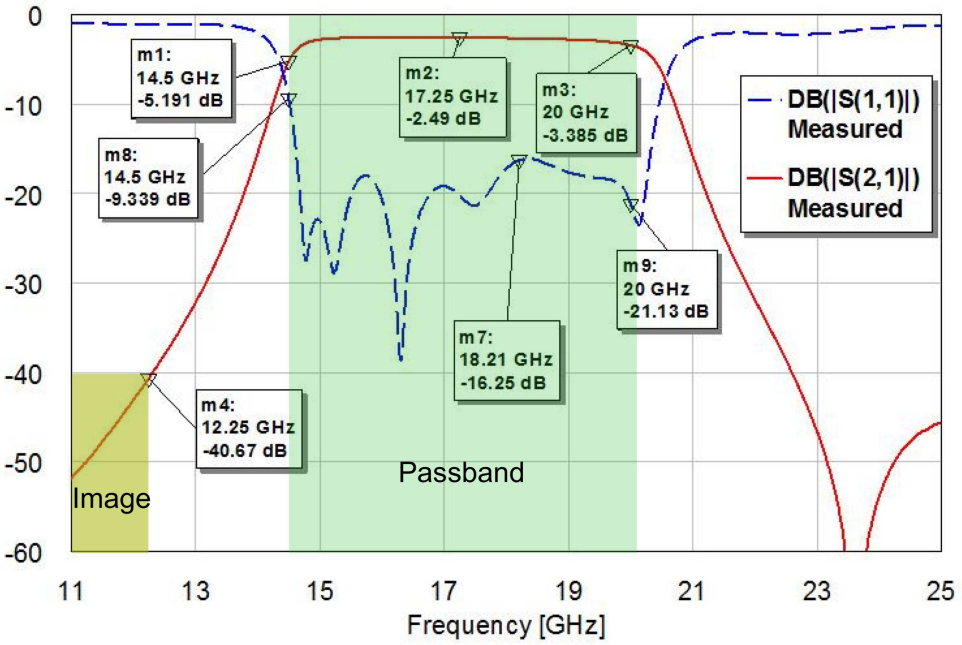

Fig. 5.21 Image reject filter Measured response.

bandwidth and the ADC acts as a down-converter as the RF signal is aliased down to the first Nyquist zone. Nyquist zones repeat at intervals of $f_s/2$ where f_s is the sampling frequency. For bandpass sampling, the aliasing effect is taken advantage of by recovering the replicated signal at a lower frequency without analogue mixing. It can therefore eliminate the need for an analogue downconversion stage in a receiver chain.

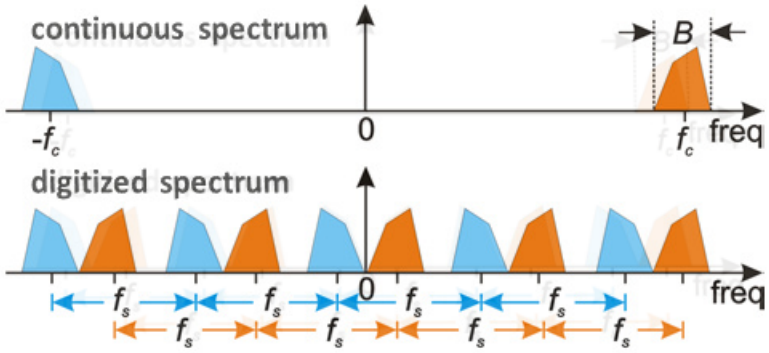

Fig. 5.22 Spectral replication in bandpass sampling [54].

For bandpass sampling a band limited signal (f_L,f_U) without overlap of aliased signals, the sampling rate is chosen such that [55]:

$$\frac{2f_U}{n} \leq f_s \leq \frac{2f_L}{n+1}, \tag{5.15}$$

where B is the signal bandwidth and n is a positive integer that represents the factor by which the signal is undersampled. The integer n is constrained by:

$$1 \leq n \leq \frac{f_U}{B} \tag{5.16}$$

(5.15) and (5.16) can be represented graphically by normalising using the bandwidth B as shown in Fig. 5.23. The allowable sampling regions are shown in white. For the 4.5 GHz IF where $B = 2.5$ GHz a sampling rate $f_s = 6$ GHz and $n = 2$ was selected such that the signal will be symmetrically centred in the middle of the second Nyquist zone at 4.5 GHz ($3f_s/4$). An ADC with sample rates 6.4 GSPS, ADC08DJ3200 [56] from Texas Instruments was identified. The sampling scheme used for the system is illustrated in Fig. 5.24 showing the wanted IF spectrum and interfering signals in the other Nyquist zones. Since the signal is in an even Nyquist zone, the aliased signal is inverted in the first Nyquist zone which can be recovered in the digital domain provided the signal has good spectral flatness within the band [57]. As all signals from the other Nyquist zones alias to the first, it's critical that the analogue signal is bandlimited and there are no signals in the other Nyquist zones. The filtering of the analogue signal is performed by the anti-aliasing bandpass filter which is discussed in the next section.

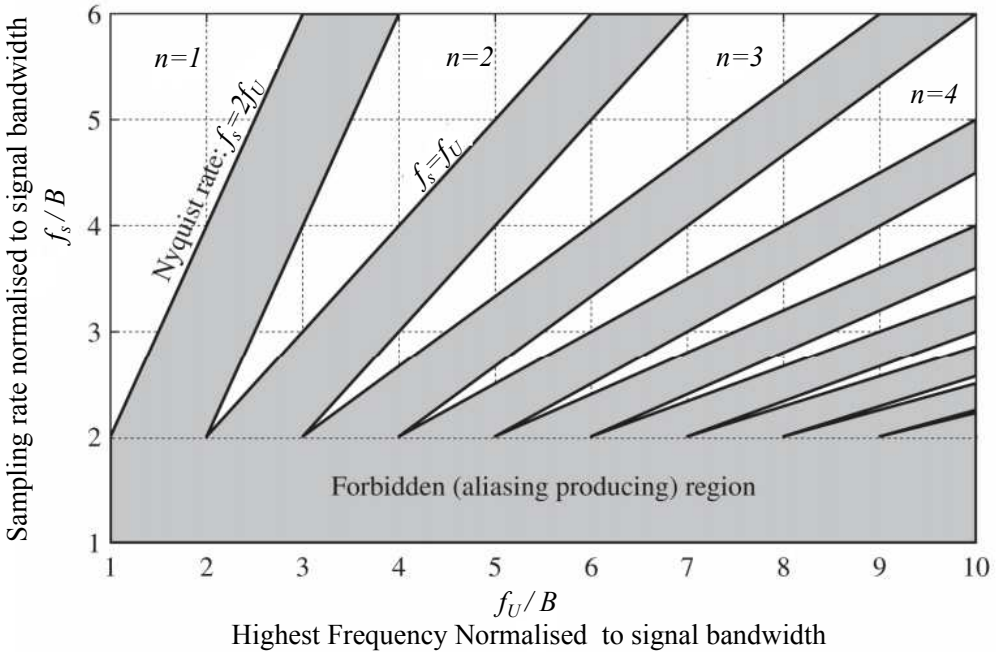

Fig. 5.23 Regions of accepted sampling for undersampling [58]

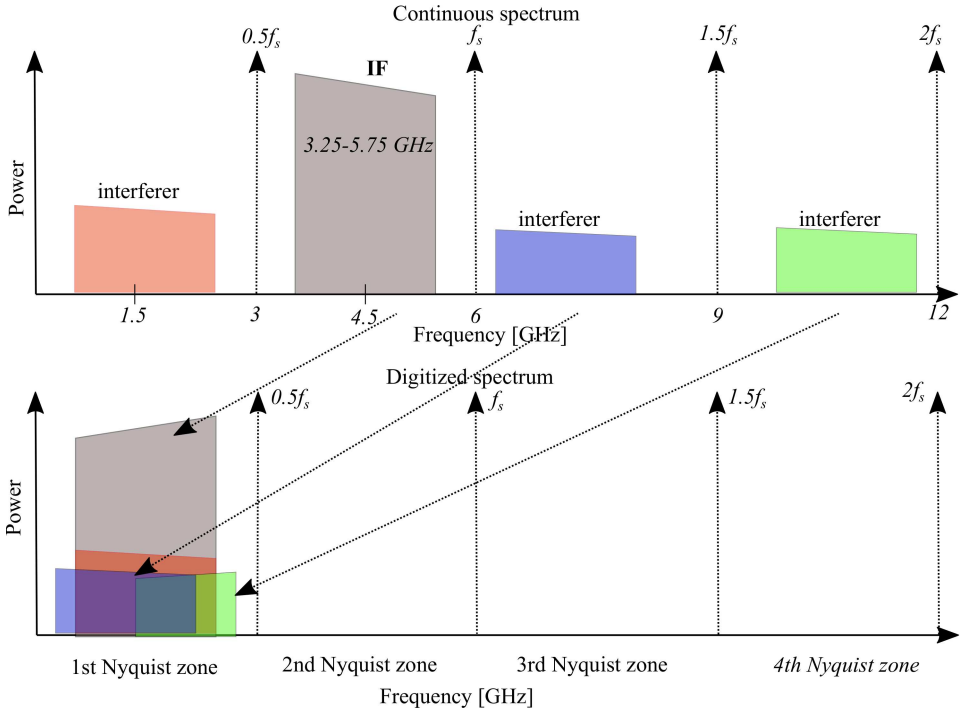

Fig. 5.24 Undersampling scheme at f_s =6 GHz showing interfering signals aliasing to the first Nyquist zone together with the wanted signal.

5.2.6 IF Anti-aliasing Filter Design

As discussed in the previous section, the anti-aliasing filter will be critical for undersampling of the IF signal. From Fig. 5.25 it can be seen that the lower ($f_{stop(L)}$) and upper ($f_{stop(U)}$) frequency where overlapping of aliases starts can be calculated as:

$$f_{stop(L)} = f_L - 2(f_L - 0.5f_s) \tag{5.17}$$

$$f_{stop(U)} = f_H + 2(f_s - f_U) \tag{5.18}$$

With $f_L = 3.25$ GHz and $f_U = 5.75$ GHz, the sampling frequency was selected to be $f_s = 6$ GHz which gives the stop band requirements as: $f_{stop(L)} = 2.75$ GHz and $f_{stop(U)} = 6.25$ GHz using (5.17) and (5.18). The anti-aliasing filter requirements can be summarized in Table 5.4. It is desired that the stopband of the filter is as large as possible as any spurious signals in the other Nyquist zones will also alias to the first Nyquist zone with the wanted signal thereby distorting it as illustrated in Fig. 5.24.

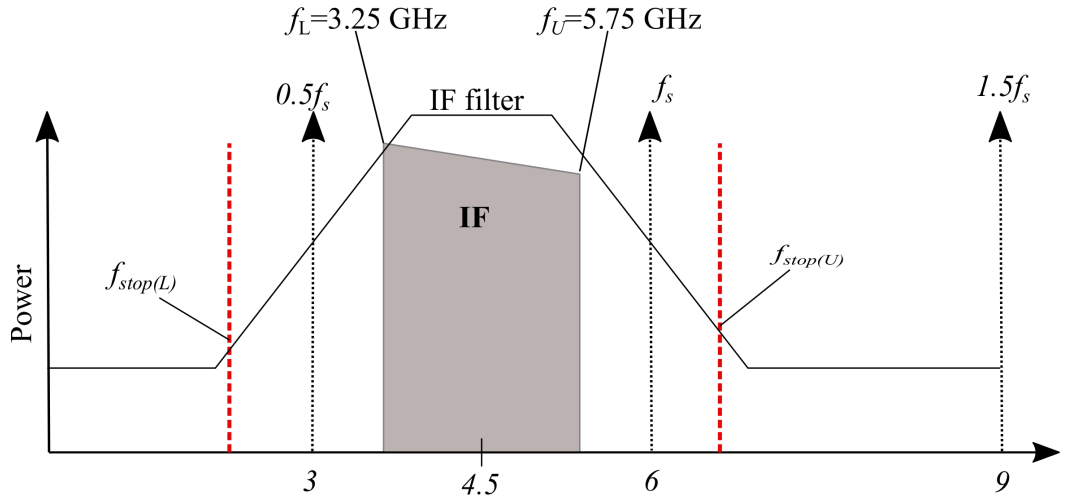

Fig. 5.25 Anti-aliasing filter specification.

Table 5.4 Anti-aliasing filter specification.

Parameter	**Specification**
Passband	3.25-5.75 GHz
Insertion loss	$\leq$2 dB
Fractional Bandwidth	55.6 %
Return loss	$\geq$-10 dB
Lower stop band $f_{stop(L)}$	2.75 GHz
Upper stop band $f_{stop(U)}$	6.25 GHz
Stop band attenuation	23 dB

The topology selected for the filter is a classic distributed bandpass filter consisting of quarter wavelength stubs based on design method published in [59]. The main advantage of the filter is the ultra-wideband performance (40-70 %) and wide stopband with its second passband occurring at three times the centre frequency ($3\omega_o$). The filter however suffers from a spurious response at twice the centre frequency ($2\omega_o$). The IFilter synthesis wizard in AWR Microwave Office was used to calculate the initial impedances and line lengths for an eighth order Chebyshev response with 0.01 dB ripple. The wizard automatically calculates the filter parameters using the design equations given in [59]. A microstrip model of the filter was created as shown in Fig. 5.26 for Mercurywave 9350 substrate [52] with a thickness of 0.211 mm. The software calculates the physical dimensions of the lines and takes into account dielectric effects and conductive losses of the circuit during simulation.

The simulated response of the model is shown in Fig. 5.27. The simulation results show poor attenuation at the lower stopband and a spurious response at 8.5 GHz. There's also a second passband at 13.5 GHz as expected from the filter topology. The dimensions obtained were then used to create a full EM model in CST to perform a simulation and optimize the dimensions of the filter. CST's Trust Region Framework optimization algorithm was used for the optimization. The CST model dimension parameters are shown in Fig. 5.29. The stubs were staggered to avoid coupling between them which would cause spurious responses. The final dimensions obtained for the filter are shown in Table 5.2.6, each stub is short circuited using a 0.15 mm radius via hole. The simulation results for the filter are shown in Fig. 5.28. The filter simulations met the passband specification after optimization. However, the 23 dB attenuation could not be met.

The filter was manufactured by Trax interconnect (Pty) LTD in Cape Town, a photograph of the filter is shown in Fig. 5.30. Fig. 5.31 shows measured results for the filter. The filter meets passband specifications defined in Table 5.4. The upper stopband attenuation is only 19 dB at 6.25 GHz and the spurious response at 8.9 GHz is -16.5 dB. This will not significantly degrade the system's spurious response as the amplitude levels of the mixer products in the stopband are relatively low as investigated in Section 5.2.3 and the gain of the IF amplifiers will be lower in the upper frequency range.

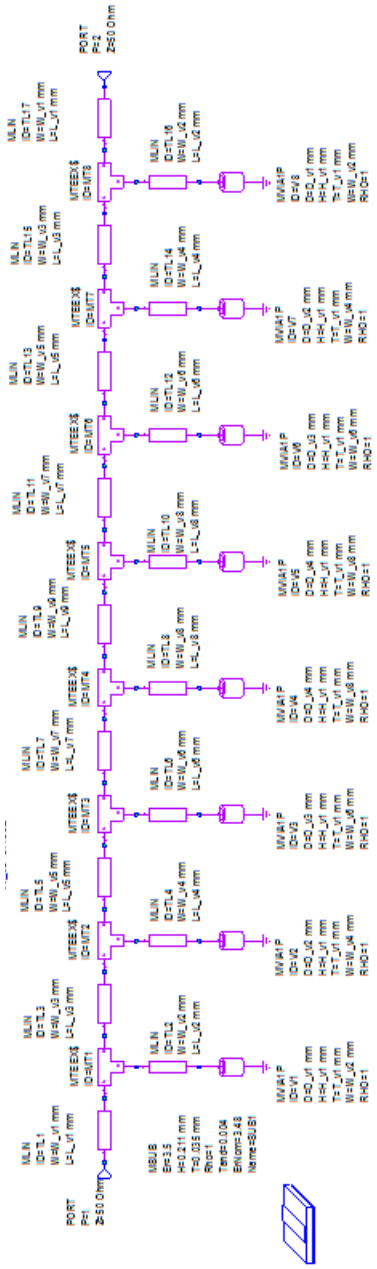

Fig. 5.26 AWR microstrip model for 8th order distributed bandpass filter.

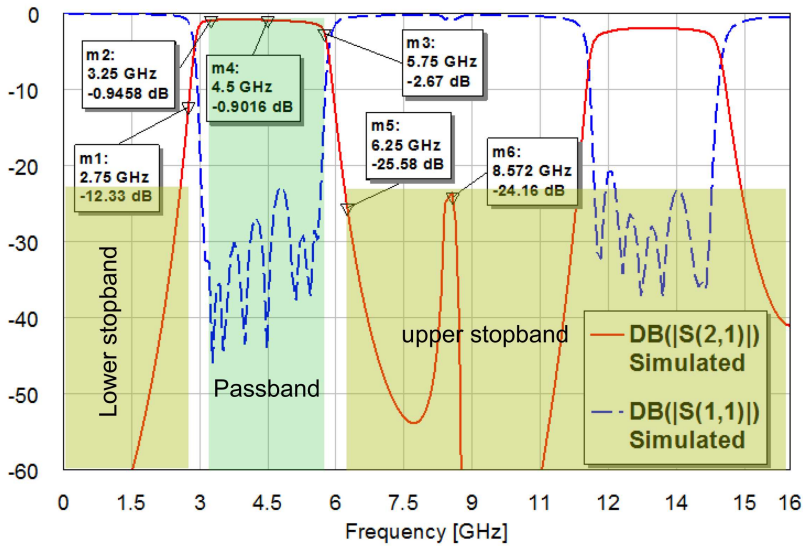

Fig. 5.27 AWR micorstrip model simulated s-paramaters for IF filter.

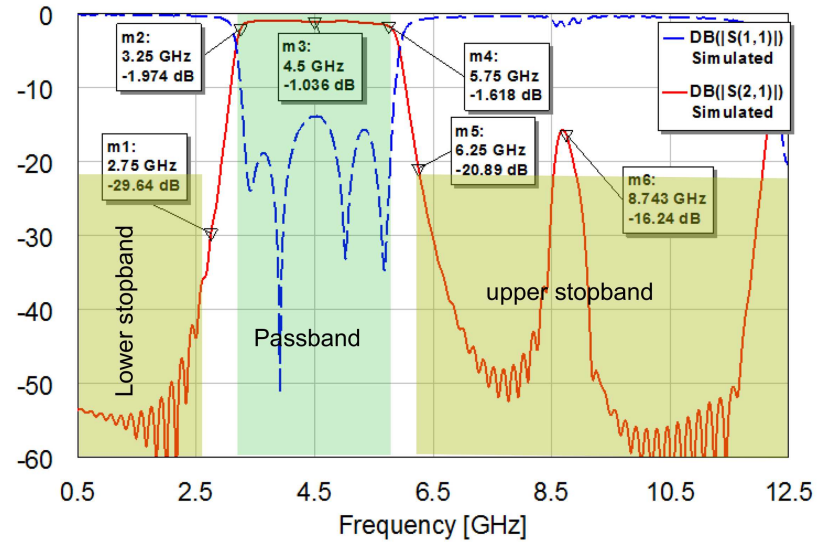

Fig. 5.28 EM simulated s-paramaters for IF filter .

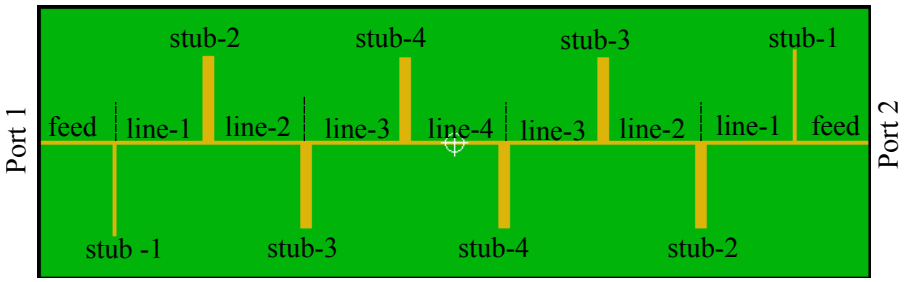

Fig. 5.29 Structure of IF anti-aliasing filter showing the different line sections of the filter.

Table 5.5 IF anti-aliasing filter dimensions.

Section	width (mm)	length (mm)
feed line	0.47	8
stub-1	0.45	9.5
stub-2	0.45	8.6
stub-3	1.3	8.6
stub-4	1.3	8.6
line-1	0.52	9.7
line-2	0.48	9.7
line-3	0.4	9.8
line-4	0.4	9.8

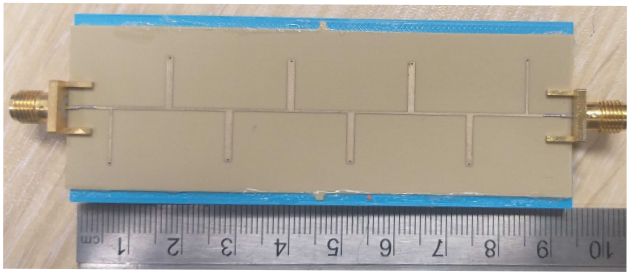

Fig. 5.30 Manufactured IF anti-aliasing filter.

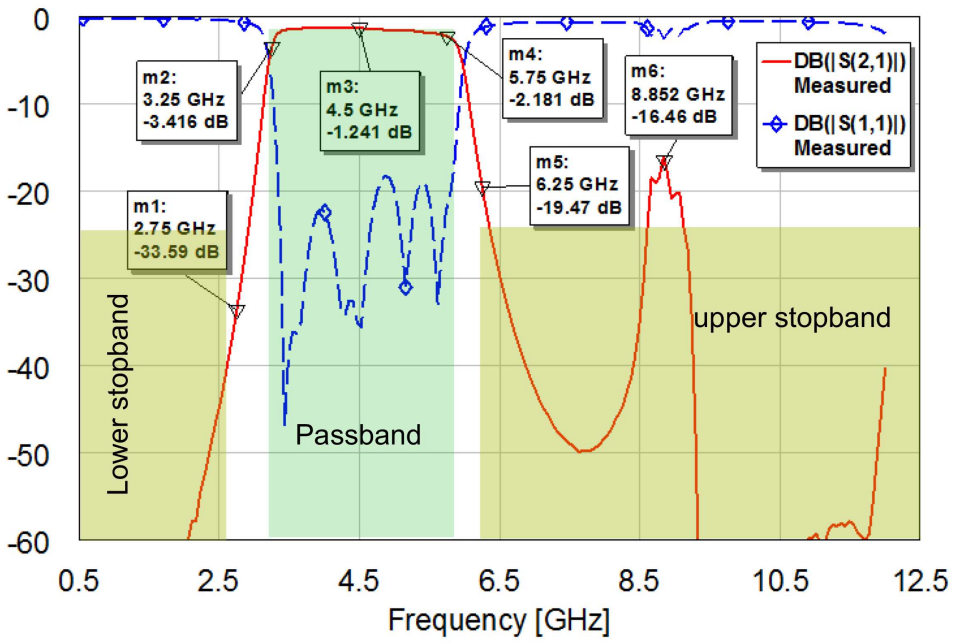

Fig. 5.31 Measured s-parameters for IF anti-aliasing filter.

5.2.7 Receiver Gain and Amplifier Selection

Gain Calculation

The gain of receiver is calculated such that the minimum integrated noise power into the LNA is amplified to the ADC nominal working point whilst the antenna is pointed at zenith (cold sky). The nominal input noise power into the receiver when pointed at zenith is calculated as:

$$P_{nom} = 10\log(kT_{prx}B \times 1000) \quad [\text{dBm}], \tag{5.19}$$

where T_{prx} is the noise temperature which the antenna sees whilst looking into the sky and B is the bandwidth of the feed input. T_{prx} was estimated to be in the region of 20 – 40 K for initial design purposes[2] and B is taken to be 10 GHz as the WR-51 adaptor is expected to have a wider bandwidth than the rated 15 to 22 GHz. The maximum gain of the receiver G_{rx} is then calculated using:

$$G_{rx} = P_{ADC} - P_{nom} \quad [\text{dB}], \tag{5.20}$$

where P_{ADC} is the ADC nominal working point which was specified to be the ADC's 12 dBFS (below Full Scale) level by internal SKA requirements. This power level ensures the optimum signal to noise ratio for this application. P_{ADC} is -12 dBm for an ADC full scale of 0 dBm. This gives a gain $G_{rx} \approx 70$ dB for the full receiver lineup.

Low Noise Amplifier

An ambient LNA **LNF-LNR10_30A** [61] operating from 10 GHz to 30 GHz from Low Noise Factory was selected for the system. The LNA is rated to have a typical Noise Figure of 1.4 dB and a Gain of 27 dB. Using (5.11) the equivalent temperature of the LNA is 110.3 K at an ambient temperature of 290 K. As this is the first stage in the receiver lineup, the cascaded noise temperature of the system is expected to be in this region. The key specifications of the LNA are summarized in Table 5.6.

[2] Sky temperature distribution graphs given in ITU Radio Noise Recommendation ITU-R P.372-7 [60] were used for initial design requirements

Table 5.6 LNF-LNR10_30A Specification [61].

Parameter	Specification
RF bandwidth	10-30 GHz
Noise Figure	1.4 dB
Gain	27 dB
Input Return Loss	-14 dB
Output Return Loss	-13 dB
Output P1dB	-8 dBm
OIP3	2 dBm

IF Gain

With a mixer conversion loss of 9 dB, filter and connector losses taken into account, an IF gain of over 50 dB was required for the system. Two gain amplifier types ZX60-5916MA+ [62] and ZRON-8G+ [63] from Mini-Circuits were selected for the IF gain amplifiers: IF AMP1, IF AMP2 and IF AMP3 (see Fig. 5.13 for reference). ZRON-8G+ amplifier is used for IF AMP2 and IF AMP3. The main considerations for the choice of amplifiers were gain flatness, return loss and gain compression of the amplifiers. Using one power amplifier to provide the required gain would be more convenient and avoid mismatch losses of cascading several amplifiers together but a cheaper and low power solution was preferred for the system. The key specifications of the amplifiers are summarized in Table 5.7.

Table 5.7 IF gain amplifier specifications.

Parameter	ZX60-5916MA+ [62]	ZRON-8G+ [63][3]
RF bandwidth	1.5 - 6 GHz	2 - 8 GHz
Noise Figure	6.6 dB	6 dB
Gain	15 dB	20 dB
Input VSWR	1.6	1.2
Output VSWR	1.3	1.2
Output P1dB	13 dBm	20 dBm
OIP3	Not specified	30 dBm

Mismatch loss and gain flatness is often of concern when cascading amplifiers in such a configuration. The cascaded s-parameters for the line-up were therefore simulated using

[3] Amplifier used in 12 V supply configuration. Can be used in 15 V configuration.

AWR Microwave office to obtain the S21, S11 and S22 response of the IF chain shown in Fig. 5.32. As can be seen from the response, a gain flatness of about 4 dB is achieved within the band. However, the return loss of the system is of concern as it it's below -10 dB in the higher range of the IF band. Mismatch is likely to cause some ripple in the system which is to be investigated further during system measurements.

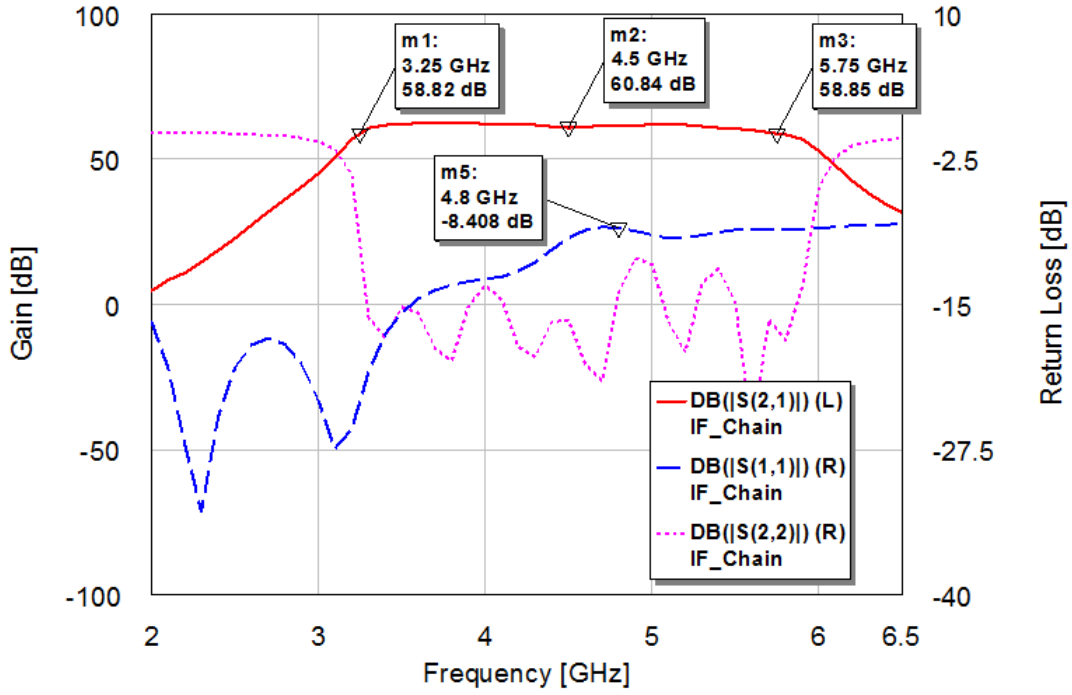

Fig. 5.32 Simulated IF chain s-parameters.

5.3 Receiver System Simulation

A system level analysis of the receiver was carried out using AWR VSS software [8] with the model shown in Fig. 5.33. The amplifiers in the model all use behavioural models of nonlinear amplifiers provided in VSS. The software uses a fifth-order polynomial to model the nonlinearity using the parameters provided from the datasheets. Measured results for both the IF and the Image reject filter were also used, exported s-parameter files from the Vector Network Analyser are imported in the model. A file based model is used for the mixer as discussed in section 5.2.3 to estimate the suppression of spurious signals.

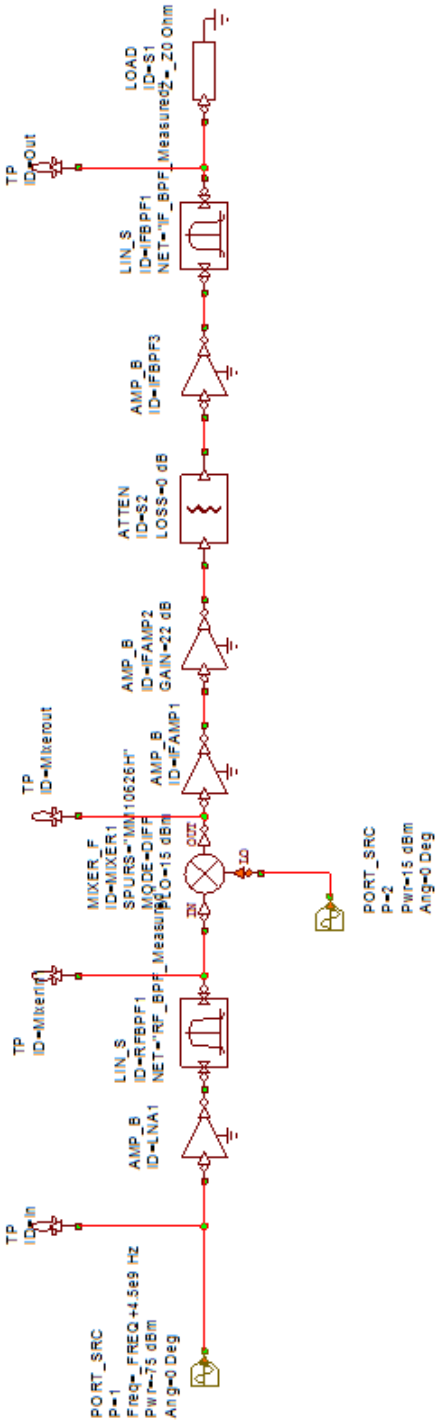

Fig. 5.33 VSS setup for system level simulations.

5.3.1 Receiver Budget

The cascaded Noise Figure, Gain, Input P1dB Compression and Input IP3 for the receiver were simulated. Fig. 5.34a shows the cascaded gain of the system showing a maximum gain of 75 dB. An attenuator was included in the model before the last IF amplifier stage in order to adjust the maximum gain of the chain. The cascaded Noise Figure is shown in Fig. 5.34b. As can been seen from the graph, the cascaded Noise Figure is 1.74 dB, it degrades slightly because of the filter's insertion loss and the mixer conversion loss. The Noise Figure can be improved by adding an amplifier directly after the LNA with an increase in cost as amplifiers at the RF frequency are much more expensive. The cascaded input P1dB and IP3 are shown in Fig. 5.34c and Fig. 5.34d at -50 dBm and -46 dBm respectively. It's important that the system remains linear even in the presence of RFI. The IF amplifiers with the higher input compression were selected to be at the end of the receiver chain to maximise the cascaded P1dB.

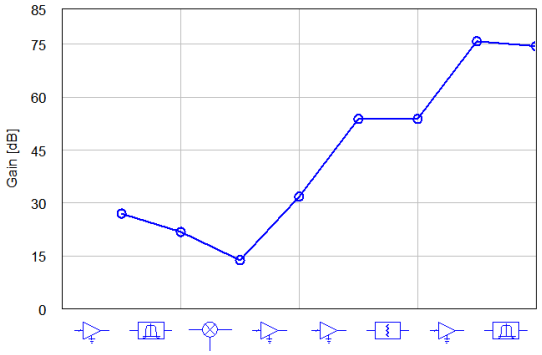

(a) Cascaded Gain.

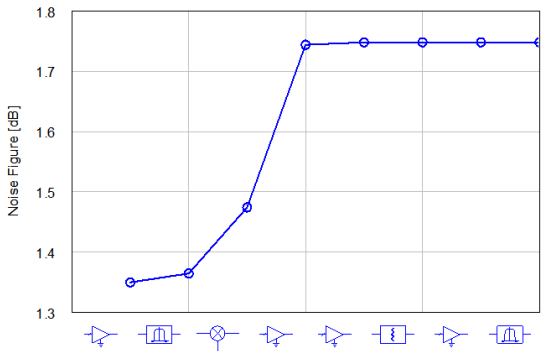

(b) Cascaded Noise Figure.

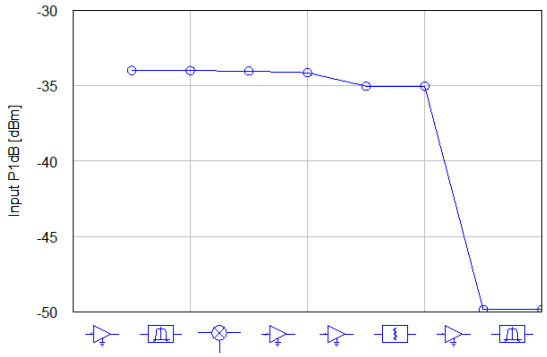

(c) Cascaded Input P1dB.

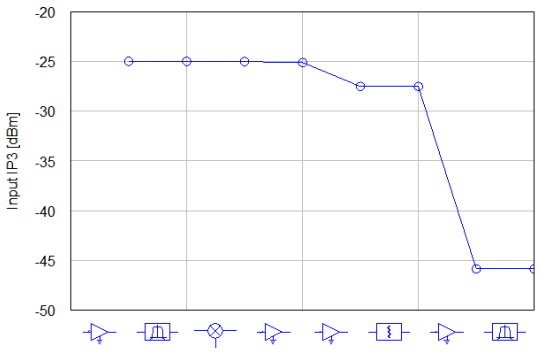

(d) Cascaded input IP3.

Fig. 5.34 Cascaded Receiver Budget Results

5.3.2 Selectivity and Image rejection

The selectivity of the system was simulated over the operational band of the receiver. The LO signal is swept from 10 to 15.5 GHz and the RF input tracks the LO (RF=LO+4.5 GHz) to maintain IF at 4.5 GHz. The output from the simulation is shown in Fig. 5.35. The blue lines show the output from the IF filter whilst the dotted pink lines show the output from the mixer port before amplification and filtering. The fundamental frequency at 4.5 GHz is 34 dB above the nearest spurious response which originates from $2f_{LO} - f_{RF}$. The response won't be attenuated by the IF filter as it falls within the bandwidth of the IF filter as can be seen from the graph. The system image rejection was also tested using a 20 GHz tone and a tone at 12.25 GHz at the edge of the image band where the worst image rejection is expected as discussed in Section 5.2.4. The system achieves an image rejection of about 40 dB as expected from the response of the image reject filter used as can be seen from the simulation results in Fig. 5.36.

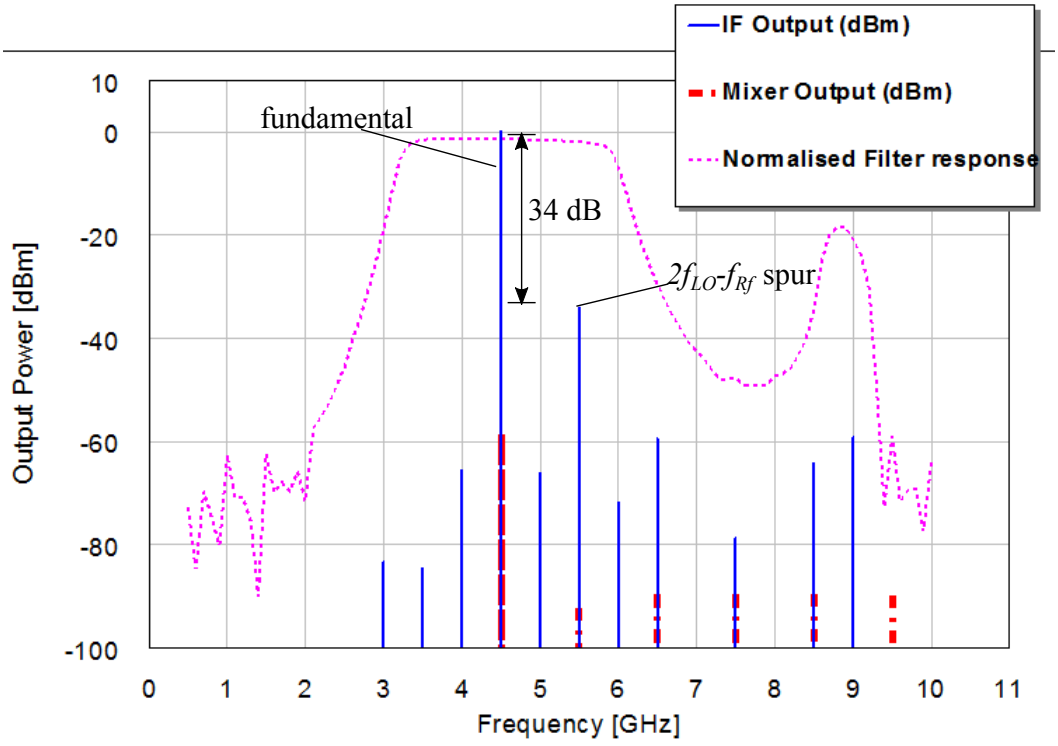

Fig. 5.35 Cascaded system spurious response.

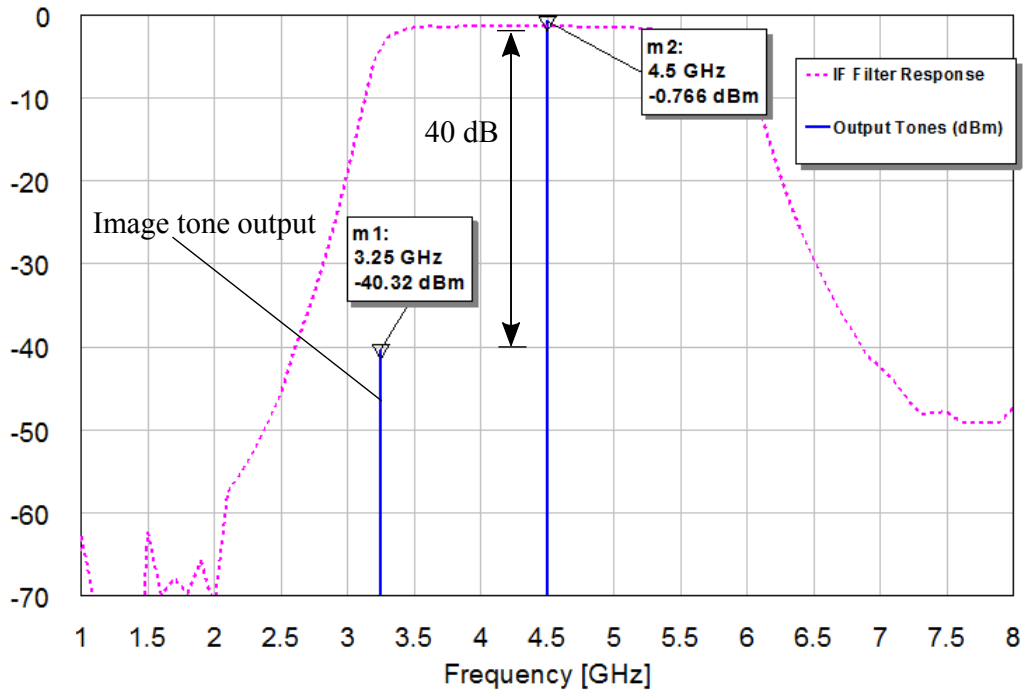

Fig. 5.36 Image rejection of 12.25 GHz image tone.

5.4 Conclusion

In this chapter the design of a front-end radio astronomy receiver operating from 14.5 to 20 GHz was discussed. The design consists of a single down-conversion stage to a 4.5 GHz IF with an instantaneous bandwidth of 2.5 GHz. Key receiver considerations: image rejection. receiver noise and choice of IF were discussed. Key filter requirements and the custom designed filters were presented. The filters achieve the required image rejection and IF selectivity for bandpass sampling required for the receiver. Off-the-shelf components used in the receiver are presented together with their main specifications and rationale for selection. The simulation results for the receiver shows a maximum gain of 75 dB and a noise figure of 1.74 dB. The simulated input $P1_{dB}$ and IP3 are -50 dBm and -46 dBm respectively. The simulated image rejection for the system is 40 dB. The spurious free dynamic range (SFDR) for the system is 34 dBc due to a third order mixer product within the IF bandwidth. The spurious suppression will be superior if high-side tuning is used for the downconversion.

Chapter 6

Front-end Receiver Measurement

This chapter discusses the measurement of the front-end receiver and verification of the components used in the system. Frequency response measurement and compression measurements for the amplifiers used in the system were carried out. The integrated receiver front-end without the antenna was characterized using singnal generator sinusoidal single tone signals. The gain characterization, spurious response and image rejection measurement results are presented. With characterization of the receiver performance from laboratory measurements, the full system sensitivity and selectivity can be estimated. The layout of modules in the receiver design is as presented in the previous chapter (see Fig. 5.13).

6.1 Amplifier Measurements

6.1.1 Low Noise Amplifier

S-Parameter Measurements

The LNA (LNF-LNR10_30A) [61] was measured for conformance with the specified parameters in the datasheet. A photograph of the LNA is shown in Fig. 6.1. It's a connectorized module with 2.92 mm connectors that are compatible with SMA connectors and 3.5 mm connectors. The LNA uses a 1.5 V supply with a 29 mA drain-source (I_{ds}) current, the DC operating point used for measurements are shown in Table 6.1. The measured S-Parameters are shown in Fig. 6.2. The LNA has an average gain of 25 dB and the return loss is below -10 dB over most of the band.

Table 6.1 LNA DC Operating point.

Parameter	Datasheet Value	Measured Value
V_{ds}	1.5 V	1.5 V
I_{ds}	29 mA	29 mA
V_{gs}	-3.43 V	-2.5 V

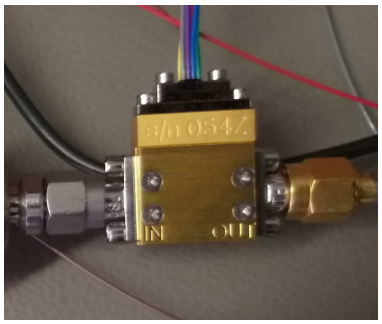

Fig. 6.1 Photograph of LNA (LNF-LNR10_30A) with SMA cables connected.

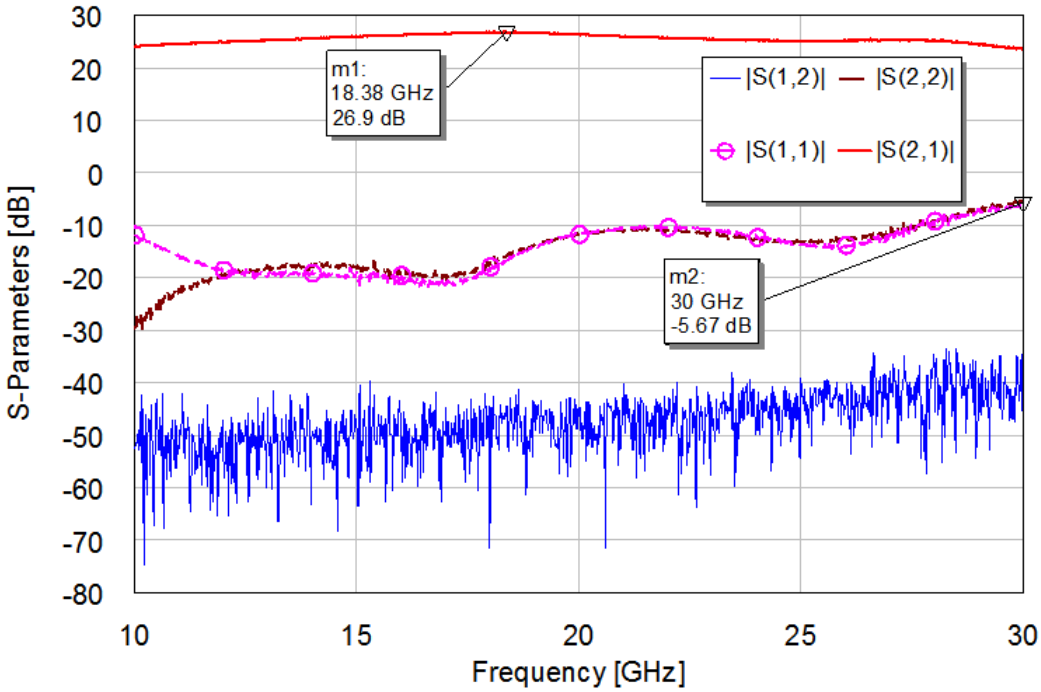

Fig. 6.2 Measured S-Parameters for LNA.

LNA Noise Figure

The noise figure of the LNA was measured using an Agilent N8975A Noise Figure Analyser. The fundamentals of noise figure and noise temperature are explained in the previous chapter. The concepts of how a Noise Figure Analyser measures noise figure using the Y-factor method are explained here as detailed in [64]. If a noise figure measurement of a Device Under Test (DUT) as shown in Fig. 6.3 is considered, the input into the device is switched between a cold source (T_{off}) and hot source (T_{on}). The ratio of the cold source power P_{off} and hot source power P_{on} at the output, the Y-factor is defined by (6.1).

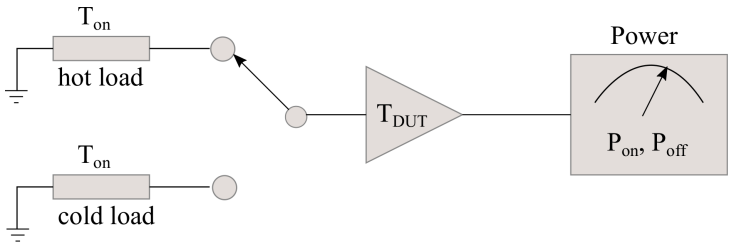

Fig. 6.3 Y-factor method for measuring equivalent noise temperature.

$$Y = \frac{P_{on}}{P_{off}} = \frac{T_{on} + T_{DUT}}{T_{off} + T_{DUT}}, \tag{6.1}$$

where T_{DUT} is the equivalent noise temperature of the DUT. By solving (6.1), the DUT noise temperature is calculated as:

$$T_{DUT} = \frac{T_{on} - YT_{off}}{Y - 1}. \tag{6.2}$$

When using the noise figure analyser, an excess noise ratio (ENR) is used to perform the hot and cold source switching. It has a pre-calibrated ENR which is calculated as:

$$ENR_{dB} = 10\log\left(\frac{T_{on} - T_{off}}{T_o}\right), \tag{6.3}$$

where T_o is the reference noise temperature (290 K). The noise figure measurement is carried out in two stages as illustrated in Fig. 6.4. In the first stage the analyser stores the values of the output powers $Pcal_{on}$ and $Pcal_{off}$ for T_{on} and T_{off} respectively and measures its internal noise temperature T_{cal}. The Y-factor measured during calibration Y_{cal} is calculated as:

$$Y_{cal} = \frac{Pcal_{on}}{Pcal_{off}} = \frac{T_{on} + T_{cal}}{T_{off} + T_{cal}}, \tag{6.4}$$

or

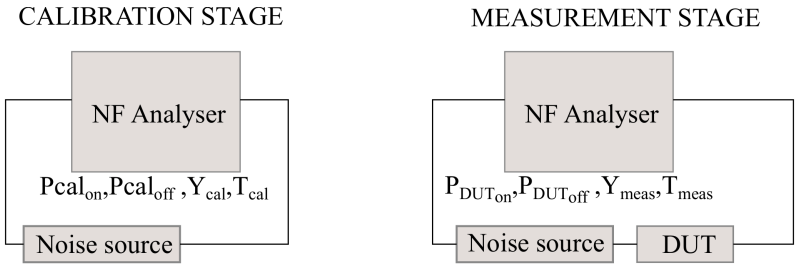

Fig. 6.4 Noise Measurement using a Noise Figure Analyser showing calibration stages.

$$T_{cal} = \frac{T_{on} + Y_{cal} T_{off}}{Y_{cal} - 1}, \tag{6.5}$$

T_{off} is the physical noise temperature of the noise source therefore T_{on} is calculated from (6.3). The analyser stores the measured values of $Pcal_{on}$ and $Pcal_{off}$, and the calculated values of Y_{cal} and T_{cal}. During the measurement of the DUT, the analyser then calculates the Y-factor Y_{DUT} from the source on $P_{DUT_{on}}$ and source off output power $P_{DUT_{off}}$ with the DUT connected as:

$$Y_{DUT} = \frac{P_{DUT_{on}}}{P_{DUT_{off}}}, \tag{6.6}$$

Using (6.2), the noise temperature of the DUT T_{meas} and analyser are given by:

$$T_{meas} = \frac{T_{on} + Y_{DUT} T_{off}}{Y_{DUT} - 1}. \tag{6.7}$$

The gain of the DUT G is then calculated as:

$$G = \frac{P_{DUT_{on}} - P_{DUT_{off}}}{Pcal_{on} - Pcal_{off}} \tag{6.8}$$

The analyser can now correct for its noise temperature and calculate the DUT noise temperature T_{DUT}:

$$T_{DUT} = T_{meas} - \frac{T_{cal}}{G} \tag{6.9}$$

The noise temperature is then converted to a noise figure using (5.11) in Section 5.1.8. The laboratory setup of the LNA noise figure measurement is shown in Fig. 6.5. An Agilent N4000A noise source rated from 10 MHz to 18 GHz and a 6 dB ENR was used. The measured noise figure is shown in Fig. 6.6. The measured noise figure at 10 GHz is 1.6 dB and 1.34 dB at 15 GHz, showing a flat measurement up to 17.6 GHz. The measurement

then rises to 4.8 dB at 20 GHz due to measurement error as the noise source used is only calibrated up to 18 GHz.

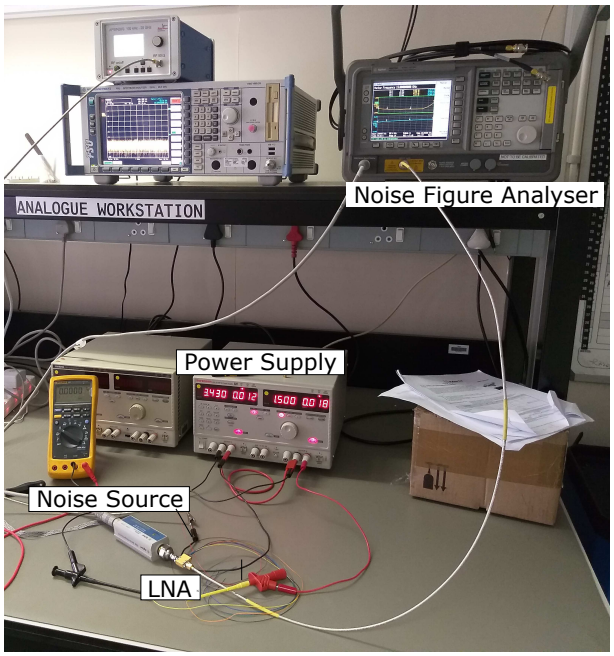

Fig. 6.5 Laboratory setup for LNA noise figure measurement.

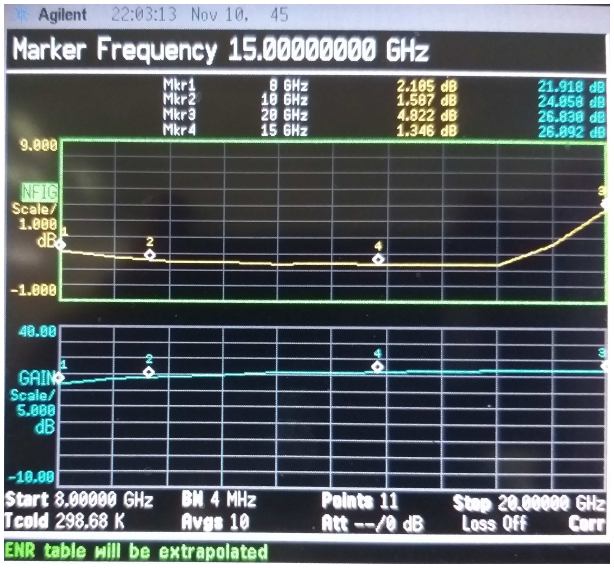

Fig. 6.6 Measurement results for LNA noise figure.

6.1.2 IF Amplifiers

The IF gain amplifiers used in the system as discussed in Section 5.2 are cascaded as illustrated in Fig. 6.7. The amplifiers will be referred to as IF AMP1, IF AMP2 and IF AMP3 in the rest of the chapter.

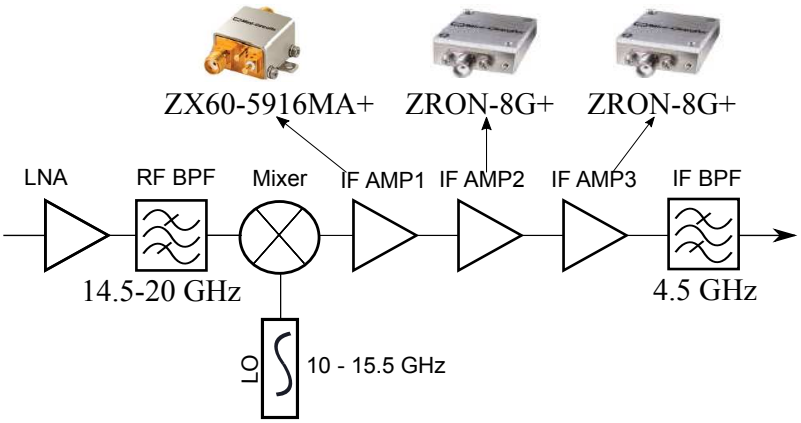

Fig. 6.7 IF gain amplifiers in the receiver.

S-Paramaters

The measured S-Parameters for the amplifiers are shown in Fig. 6.8, Fig. 6.9 and Fig. 6.10, for IF AMP1, IF AMP2 and IF AMP3 respectively. The measured S_{21} for IF AMP1 is as expected, showing a gain of about 14 dB within the band of interest. However, the amplifier has a poor return loss, with an S_{11} of more than -10 dB within the IF band (3.25 to 5.75 GHz). The effects of the mismatch on the cascaded response were investigated during the measurement of the full system. The measured results for IF AMP1 and IF AMP2 (see Fig. 6.9 and Fig. 6.10) show consistent results. Both amplifiers have a gain of about 23 dB within the IF band and the return loss is better than -10 dB. The gain flatness of the amplifiers was also investigated within the IF bandwidth by checking the minimum and maximum S_{21}. Fig. 6.1.2 shows the gain flatness response of the amplifiers. In Fig. 6.11a it can be seen that the gain flatness of IF AMP1 is 3.4 dB whilst in in Fig. 6.11b it can be seen that the gain flatness of IF AMP2 and IF AMP3 are 1.9 dB and 1.8 dB respectively.

Gain Compression

The gain compression point of the IF amplifiers was measured by calculating the $P1_{dB}$ point of each of the amplifiers using a signal generator and spectrum analyser. A single tone signal input is used and the power of the signal is measured using the spectrum analyser. Fig. 6.12,

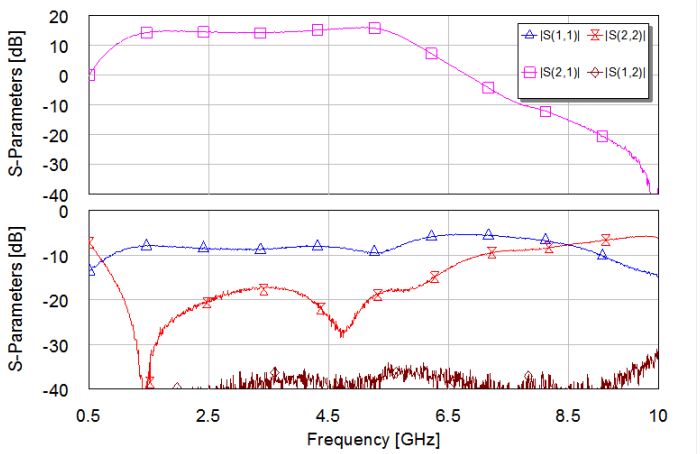

Fig. 6.8 IF AMP1 S-Parameter measurement.

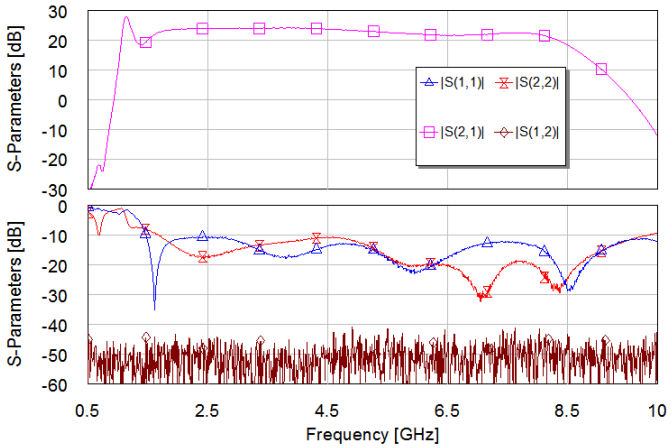

Fig. 6.9 IF AMP2 S-Parameter measurement.

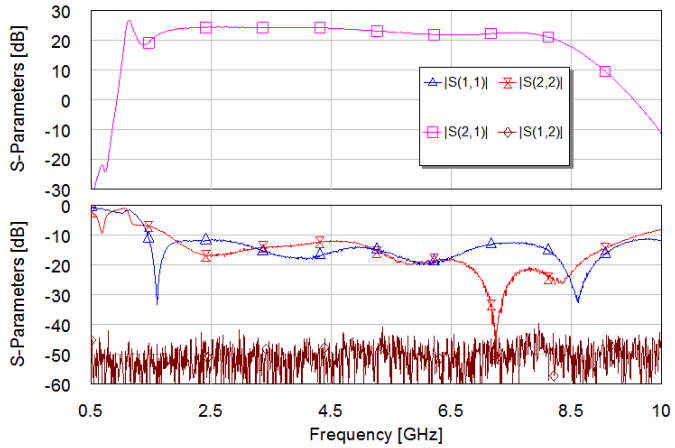

Fig. 6.10 IF AMP3 S-Parameter measurement.

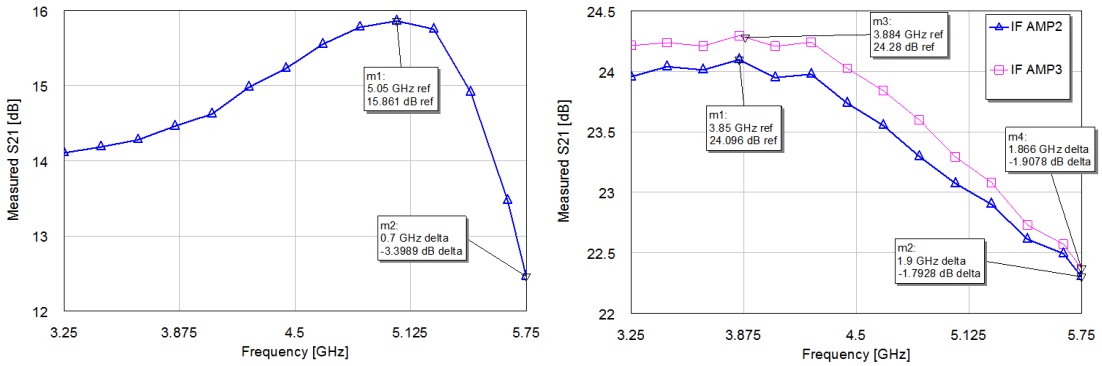

(a) IF AMP1. (b) IF AMP2 and IF AMP3.

Fig. 6.11 S-Parameter measurements showing gain flatness of IF amplifiers within IF band.

Fig. 6.13 and Fig. 6.14 show the input power against output power plots for IF AMP1, IF AMP2 and IF AMP3 respectively to model the $P1_{dB}$ point for the amplifiers at 4.5 GHz. The $P1_{dB}$ point is calculated by plotting a linear line of the input against output power shifted by -1 dB to get the intersection point with the measured input against output power plot as the $P1_{dB}$ point. IF AMP1 has an output $P1_{dB}$ of 12.5 dBm and IF AMP2 and IF AMP3 show a consistent response with a $P1_{dB}$ point at 20 dBm. Both measurements are within 2 dB of the datasheet values.

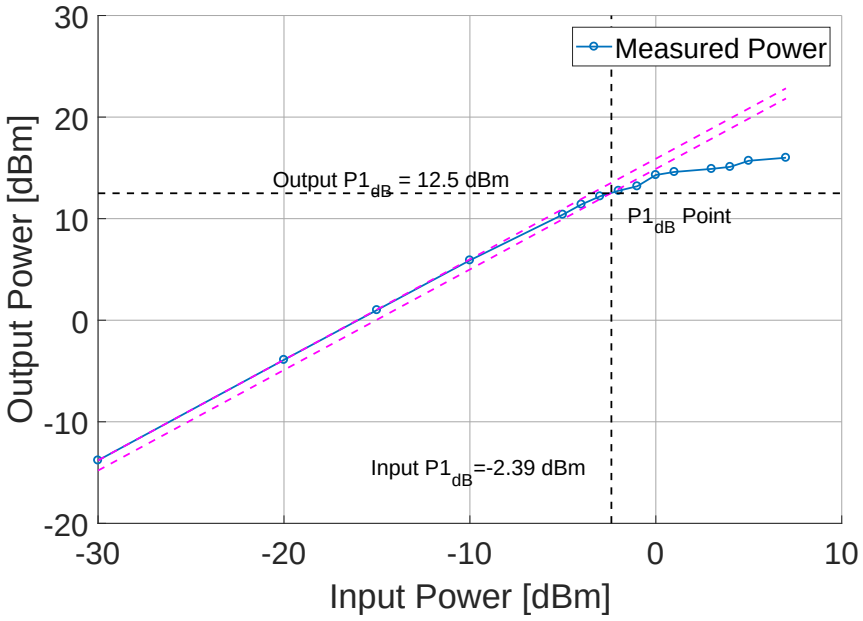

Fig. 6.12 IF AMP1 input power against output power at 4.5 GHz to calculate the $P1_{dB}$ point.

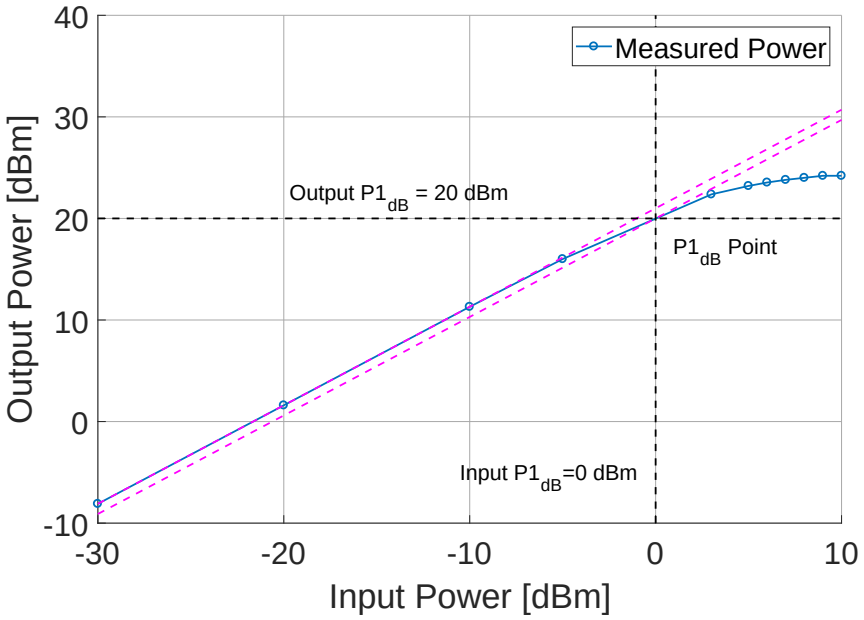

Fig. 6.13 IF AMP2 input power against output power at 4.5 GHz to calculate the $P1_{dB}$ point.

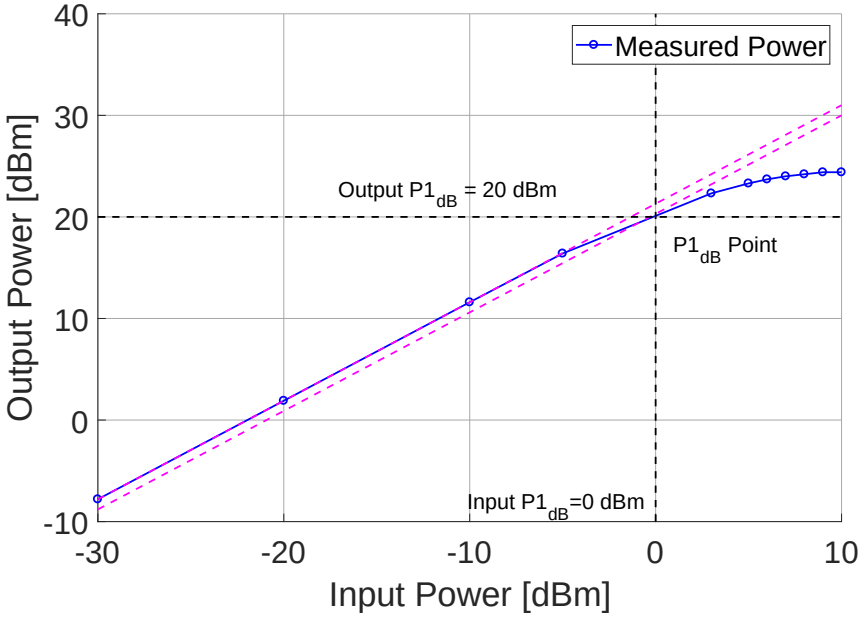

Fig. 6.14 IF AMP3 input power against output power at 4.5 GHz to calculate the $P1_{dB}$ point.

IF Amplifier Noise Figures

The three IF amplifier noise figures were verified using the noise figure analyser. As the components are further down the receiver chain, their noise figure will not impact the system

noise figure significantly. The frequency range for the measurement was set for the IF bandwidth: 3.25 to 5.75 GHz. The measured noise figures are shown in Fig. 6.15 and Fig. 6.16 for IF AMP1 and IF AMP2/AMP3 respectively. IF AMP1 has a noise figure of 3.8 dB whilst IF AMP2/AMP3 have a noise figure of 3.2 dB.

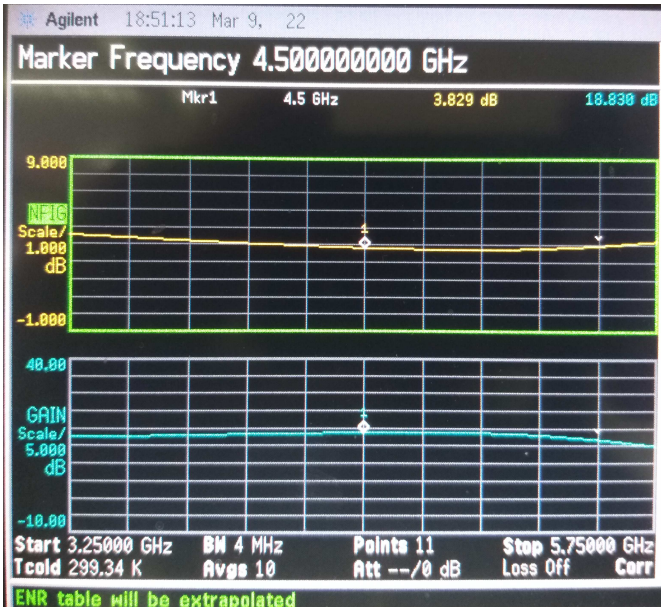

Fig. 6.15 IF AMP1 measured noise figure. Noise figure reading is 3.83 dB at 4.5 GHz.

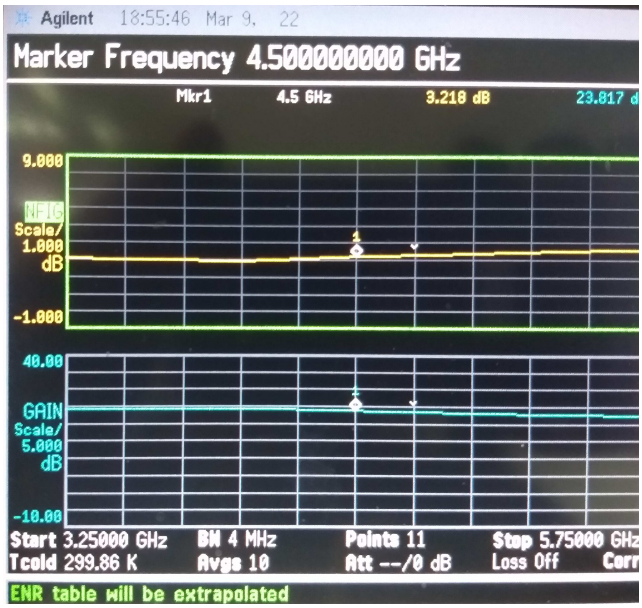

Fig. 6.16 IF AMP2/AMP3 measured noise figure. Noise figure reading is 3.22 dB at 4.5 GHz

6.2 Receiver System Measurement and Integration

The combined receiver system was measured with a signal generator input. The Laboratory setup of the combined system is shown in Fig. 6.17.

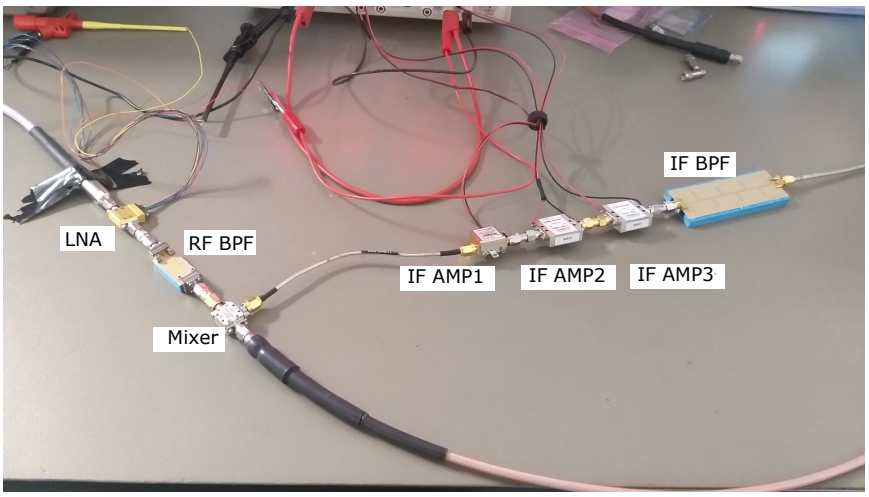

Fig. 6.17 Measurement setup of the combined receiver.

6.2.1 Linear Gain and Compression

The gain response of the system was tested using an input signal at 14.5 GHz, 17.25 GHz and 20 GHz with the LO signal respectively set to 10 GHz, 12.75 GHz and 15.5 GHz to maintain the IF output centred at 4.5 GHz for the three frequencies. The output power of the receiver was measured using a spectrum analyser. The input against output power of the receiver at 14.5 GHz, 17.25 GHz and 20 GHz are shown in Fig. 6.18, Fig. 6.19 and Fig. 6.20 respectively. The $P1_{dB}$ points calculated from the graphs are -49.6 dBm, -54.29 dBm and -49.35 dBm at 14.5 GHz, 17.25 GHz and 20 GHz respectively. The input $P1_{dB}$ is lower than the simulated value (50 dB) in Section 5.3.1, caution should be taken that there are no strong signals that will drive the receiver into compression. The gain response of at the 14.5 GHz, 17.25 GHz and 20 GHz for different input powers is shown in Fig. 6.21. The gain for a -75 dBm input signal is 76.6 dB, 70.3 dB and 70 dB at 14.5 GHz, 17.25 GHz and 20 GHz respectively.

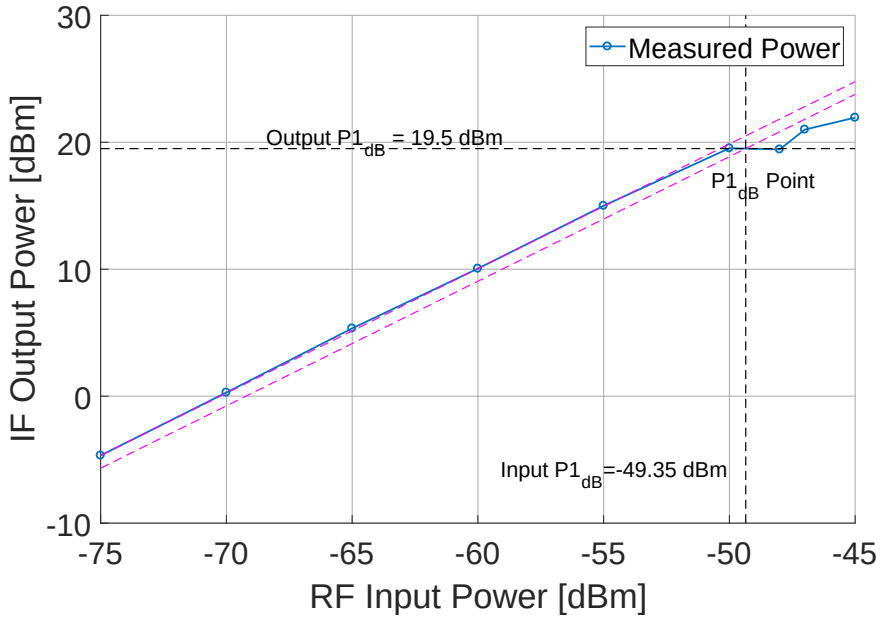

Fig. 6.18 Receiver input power against output power at 14.5 GHz to calculate the $P1_{dB}$ point.

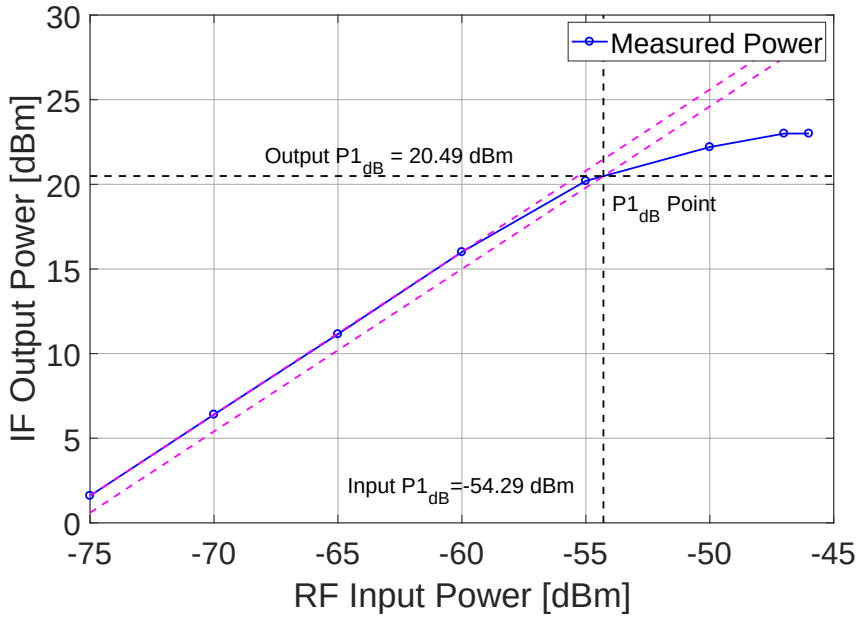

Fig. 6.19 Receiver input power against output power at 17.25 GHz to calculate the $P1_{dB}$ point.

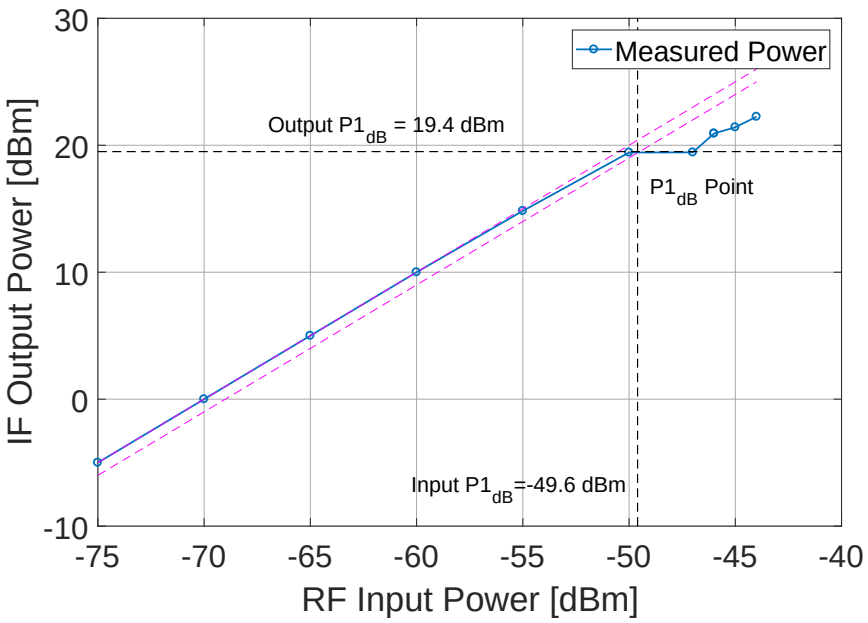

Fig. 6.20 Receiver input power against output power at 20 GHz to calculate the $P1_{dB}$ point.

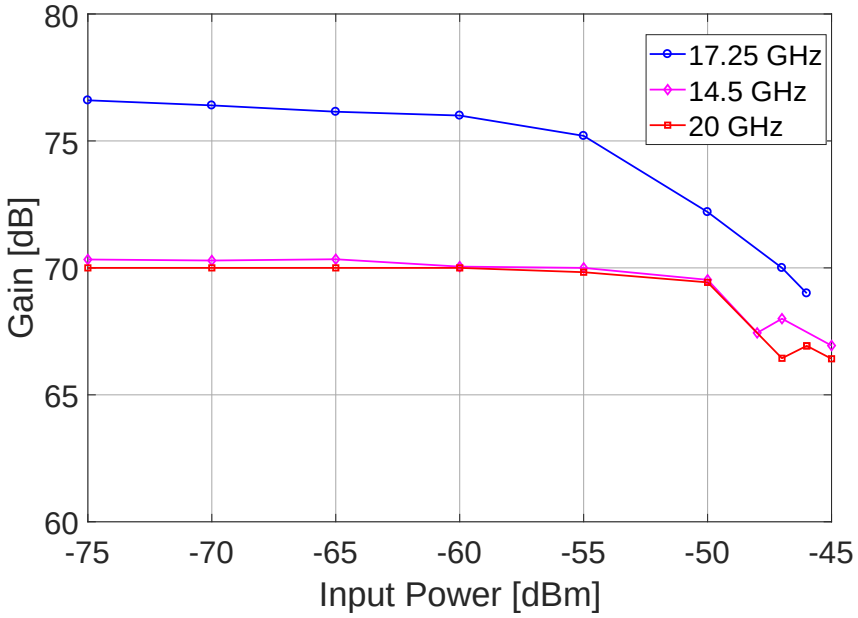

Fig. 6.21 Receiver input power against gain at 14.5 GHz, 17.25 GHz and 20 GHz.

6.2.2 Spurious Analysis

The receiver was tested for spurious outputs at the three input frequency points of 14.5 GHz, 17.25 GHz and 20 GHz with the input power set to -75 dBm. As in the gain measurements, the LO tracks the RF input to maintain the IF at 4.5 GHz. The spectrum analyser was set to measure a span of 9 GHz with a resolution bandwidth of 30 MHz. Fig .6.22 shows the measured output for a 14.5 GHz input signal, a spurious signal is observed at 5.5 GHz as expected from the $2f_{LO} - f_{RF}$ mixer product. The spurious signal is 27.34 dB below the IF signal power, the simulated SFDR in Section 5.3.2 is 34 dBc. Fig. 6.22 and Fig. 6.24 show the outputs at 17.25 GHz and 20 GHz respectively. Both frequencies show no spurious signals as they are attenuated in the stop-band of the IF anti-aliasing filter.

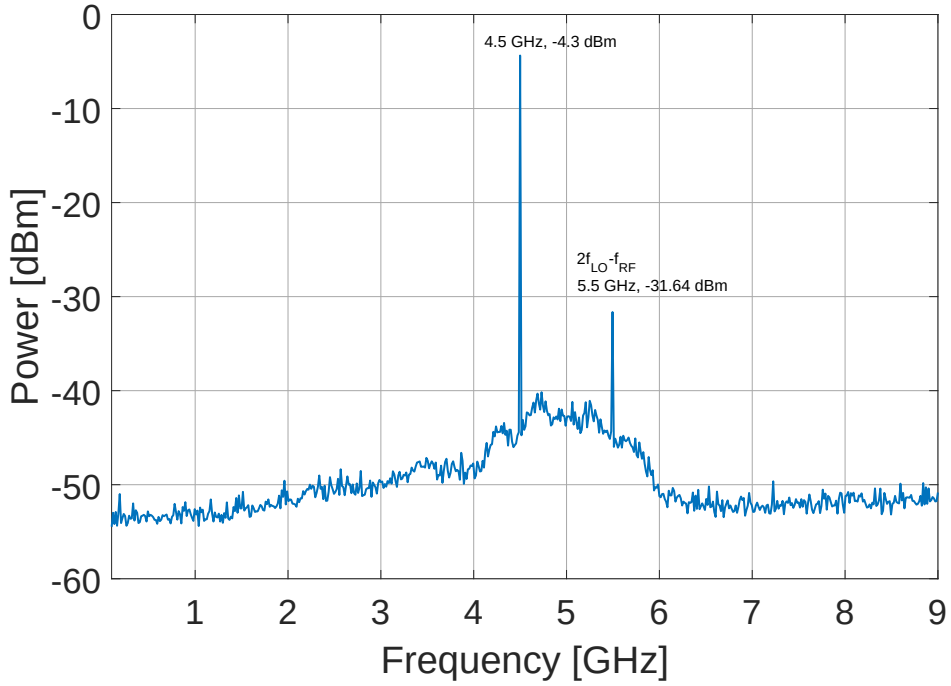

Fig. 6.22 Receiver output for 14.5 GHz RF input and 10 GHz LO input.

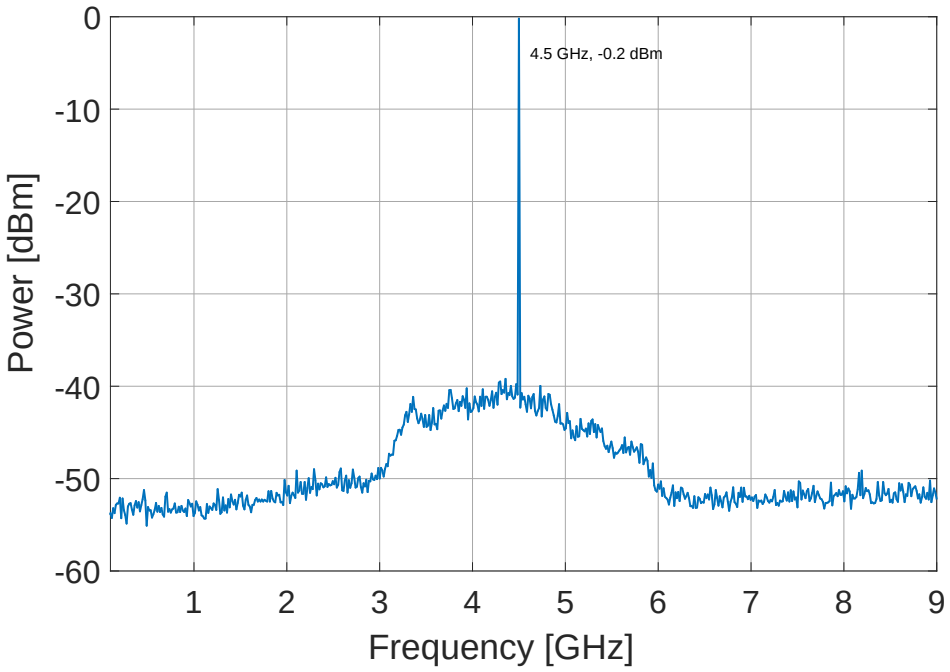

Fig. 6.23 Receiver output for 17.25 GHz RF input and 12.75 GHz LO input.

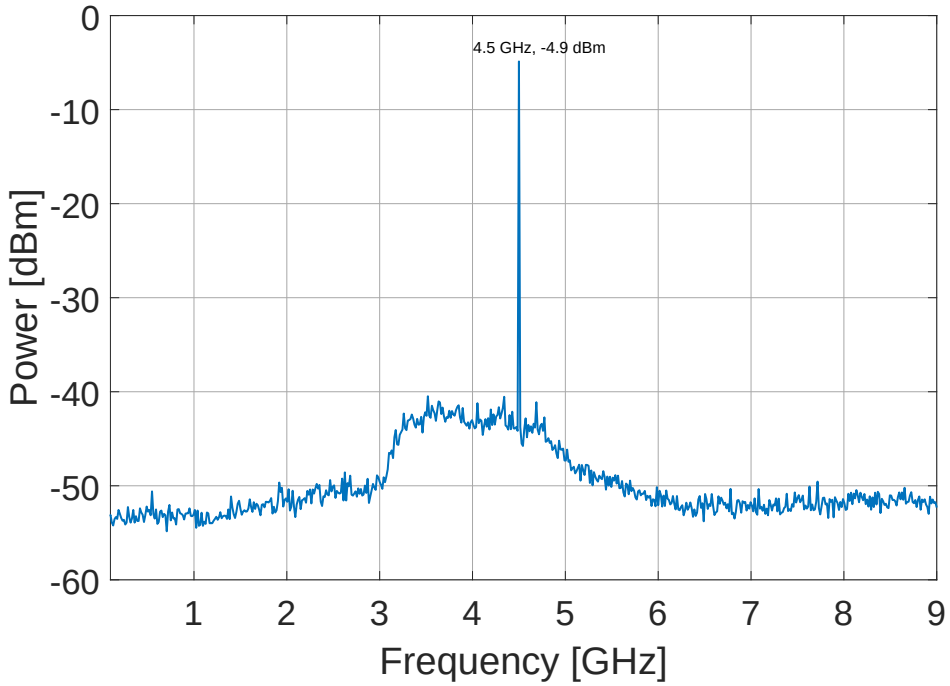

Fig. 6.24 Receiver output for 20 GHz RF input and 15.5 GHz LO input.

6.2.3 IF Response

The IF response was measured by sweeping the input RF signal and keeping LO signal constant, essentially sweeping through the IF. The RF input signal was setup to sweep with centre frequency at 15.75 GHz, 17.25 GHz and 18.75 GHz with a spacing of 48 MHz and span of 5 GHz. The LO signal is selected as $LO = RF - 4.5$ GHz. Table 6.2 summarizes the three sweep measurements carried out:

Table 6.2 RF sweep settings for IF response measurement.

Setting	Sweep 1	Sweep 2	Sweep 3
RF centre frequency	15.75 GHz	17.25 GHz	18.75 GHz
RF sweep step	48 MHz	48 MHz	48 MHz
RF sweep span	5 GHz	5 GHz	5 GHz
LO centre frequency	11.25 GHz	12.75 GHz	14.25 GHz

The measured responses for the sweep inputs described in Table 6.2 are shown in Fig. 6.25, Fig. 6.26 and Fig. 6.27 for sweep 1, sweep 2 and sweep 3 respectively. All three responses show gain ripple and a poor gain flatness due to the poor performance of IF AMP1.

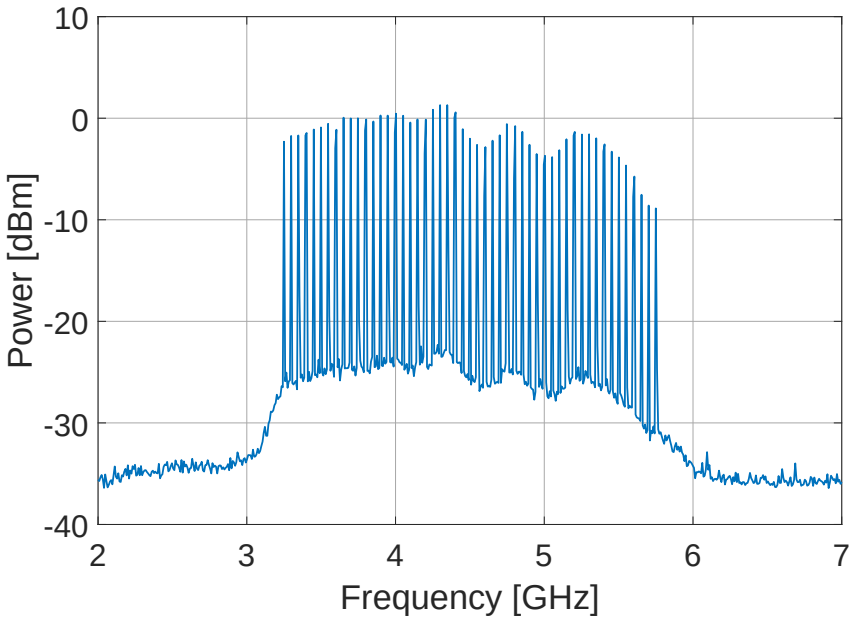

Fig. 6.25 IF response of sweep 1. RF input is centred at 15.75 GHz and swept with a 5 GHz span. LO signal is at 11.25 GHz

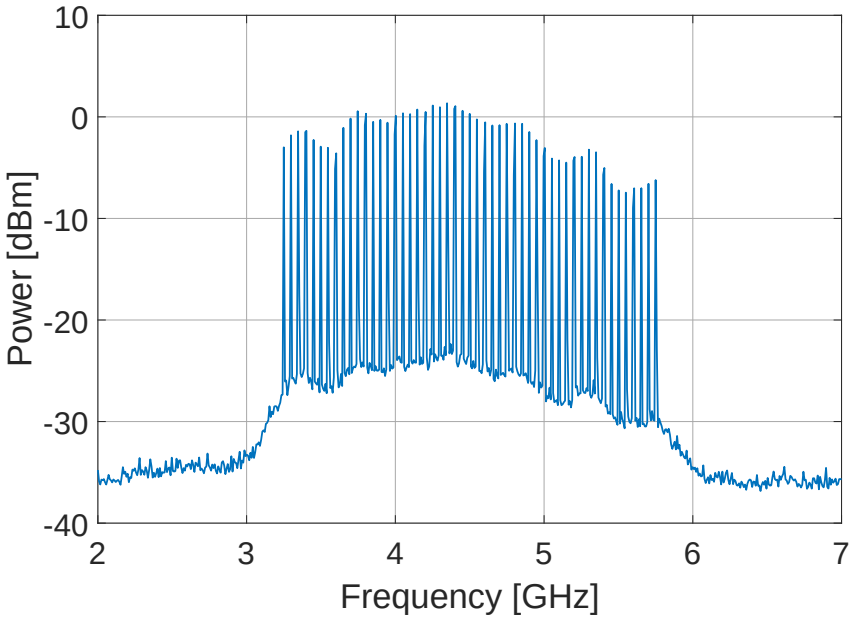

Fig. 6.26 IF response of sweep 2. RF input is centred at 17.25 GHz and swept with a 5 GHz span. LO signal is at 12.75 GHz.

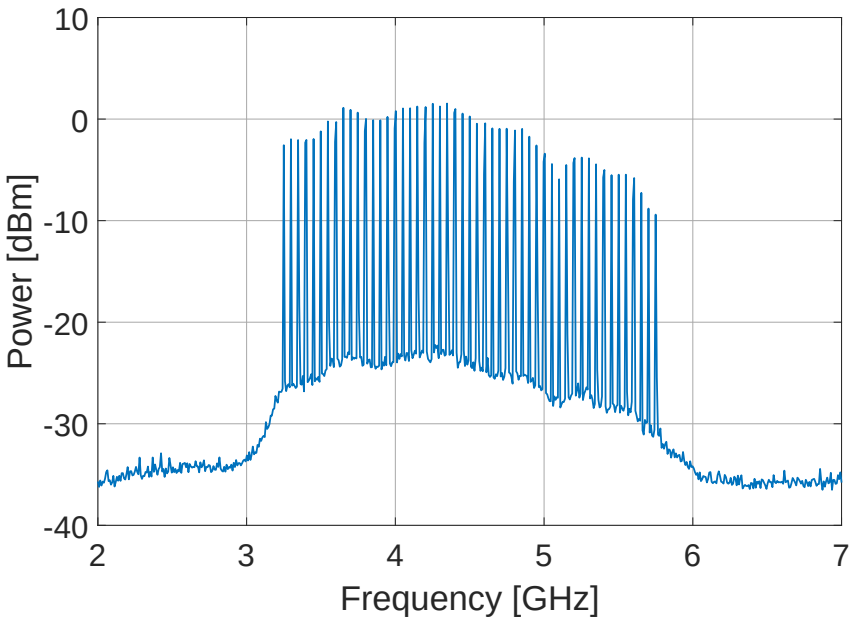

Fig. 6.27 IF response of sweep 3. RF input is centred at 18.75 GHz and swept with a 5 GHz span. LO signal is at 14.25 GHz.

6.2.4 Image Rejection

The image rejection of the receiver was measured using an RF input tone at the edge of the image band where image rejection is expected to be worst. The band edge of the image band is at 12.25 GHz as calculated in Section 5.2.4. The 12.25 GHz signal is compared to a desired RF input to the receiver set to 18.75 GHz to obtain an IF at 3.25 GHz at the lower edge of the IF bandwidth, LO is set to 15.5 GHz for both. Fig. 6.28 shows the measured output using the spectrum analyzer for the two input signals with power set to -75 dBm for both. An image rejection of 40 dB is achieved as expected from the image reject filer response.

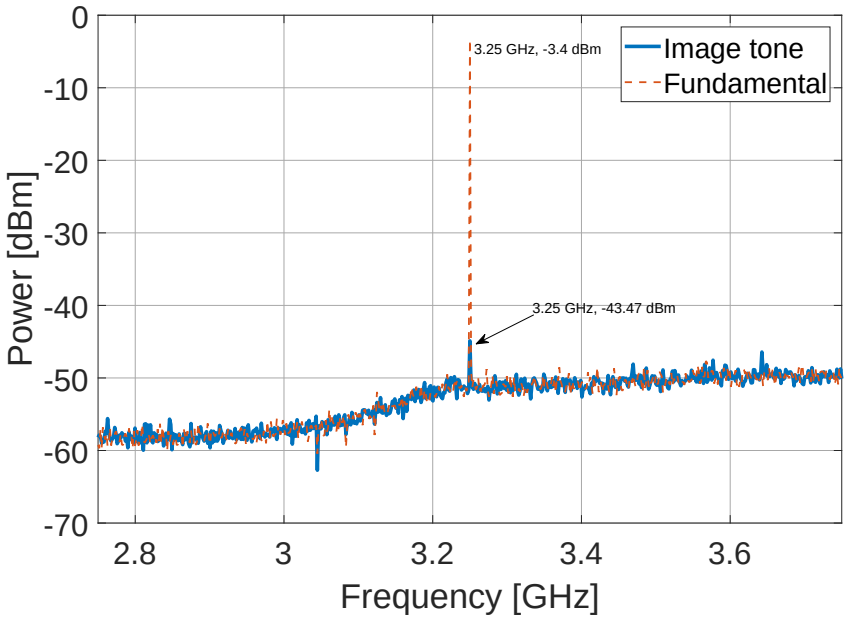

Fig. 6.28 Image frequency rejection of receiver. LO set to 15.5 GHz for 18.75 GHz (fundamental) and 12.25 GHz (image) signals.

6.2.5 Full System Sensitivity Estimation

As discussed in Section 2.2, the minimum signal that can be detected by the receiver will be determined by the system temperature T_{sys}. The system noise temperature is calculated by considering both the noise temperature of the receiver T_{RX} and the noise received by the antenna T_{ant} as illustrated in Fig. 6.29. The system temperature is referenced at the transmission line connecting the antenna to the receiver, therefore ohmic losses need to be taken into account. The receiver noise temperature referenced at the input is given by [48]:

$$T_{sys} = \frac{T_{ant}}{L} + \frac{T_o}{L}(L-1) + T_{RX}, \tag{6.10}$$

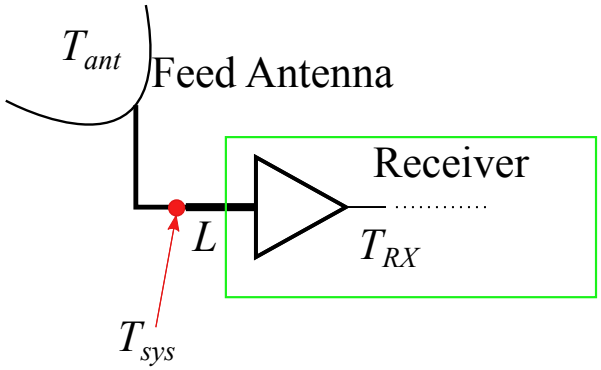

Fig. 6.29 Antenna and receiver noise analysis.

where L is the loss of the transmission line connecting the LNA to the antenna in linear scale and T_o is the physical temperature of the antenna. T_{ant} is the brightness temperature seen by the antenna's main beam including spillover temperature from the ground. In this work the antenna temperature is taken to be 40 K for the estimation of the sensitivity of the system from brightness temperature estimations discussed in Appendix B.1. This is a reasonable estimate as T_{sys} temperature for a similar telescope Green Bank is less than 40 K at 20 GHz [65] with cooled receivers. The system sensitivity is this case is dominated by the front-end electronics as the LNA is uncooled. For calculation of antenna temperature, guidelines in SKA Memo 95 [66] should be followed.

A low loss coaxial connector from mini-circuits (086 KM Model Series) [67] has been identified for the connection between the antenna and the LNA with an insertion loss of 0.3 dB. A total feed ohmic loss of 0.5 dB was assumed for the calculation. Using (6.10) with $T_o = 290$ K, T_{sys} is calculated to be 210 K. The telescope figure of merit; effective area to system temperature (A_e/T_{sys}) can be estimated using the aperture efficiency (η_{ap}) calculated as discussed in Section 3.3.6:

$$Sensitivity = \frac{A_e}{T_{sys}} = \frac{\eta_{ap} A_{phy}}{T_{sys}}, \tag{6.11}$$

The physical area A_{phy} of the MeerKAT main reflector is calculated as 143.1 m^2. Fig. 6.30 shows the calculated sensitivity from 14.5 to 20 GHz. The RMS flux sensitivity of the system can also be calculated using the integration time τ and the instantaneous bandwidth $\Delta\nu$:

$$S_{\nu_{rms}} = \frac{2kT_{sys}}{A_e\sqrt{\tau\Delta\nu}} \times 10^{26} \quad [\text{Jy}], \tag{6.12}$$

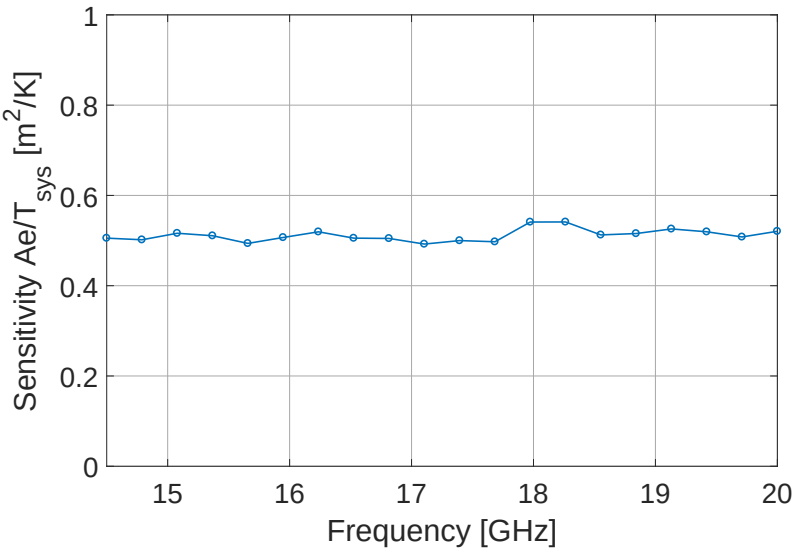

Fig. 6.30 Calculated Sensitivity for $T_{ant} = 40$ K over frequency with antenna pointed at Zenith.

An integration time of 1 second was planned after implementation of the system back-end and Δv is 2.5 GHz. Fig. 6.31 shows the calculated sensitivity in Jansky. The estimated sensitivity of the system is 110 mJy for the frequency band. The system is sensitive enough to detect common bright radio sources such as Taurus A and Orion A, Appendix B.2 shows some common bright radio sources and their flux density.

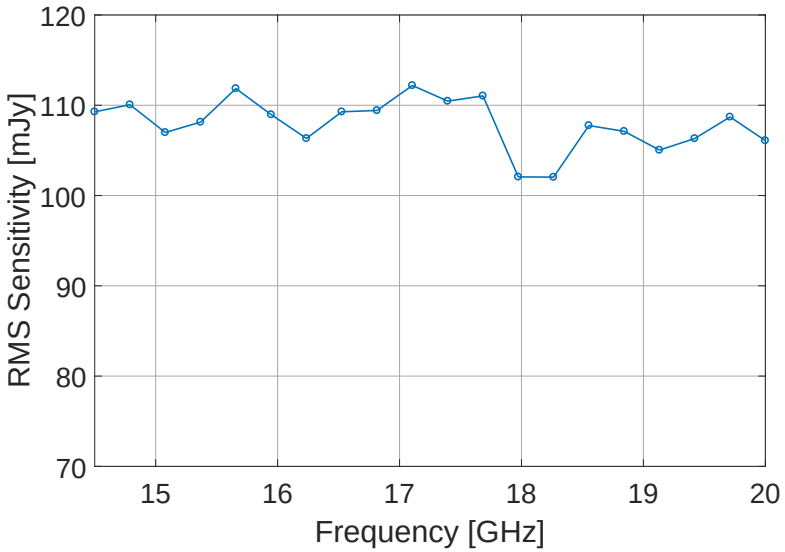

Fig. 6.31 RMS sensitivity for 1 second integration time with antenna pointed at Zenith.

6.3 Conclusion

The system components were measured and integrated for full receiver system measurements. The gain amplifier (IF AMP1) has a poor measured return loss and gain flatness and therefore affects the system performance considerably. The measured noise figure of the LNA which will predominantly affect the system noise figure is between 1.3 dB to 1.6 dB from 14.5 to 18 GHz. Accurate readings after 18 GHz could not be obtained as the noise source available is rated up to 18 GHz. The receiver achieves a maximum gain of 76 dB measured at 17.25 GHz. The minimum input $P1_{dB}$ power measured for the system is -54 dBm measured at 17.25 GHz. The spurious signals from the receiver were also measured, the worst spur using a frequency span of 9 GHz was at 5.5 GHz which is within the IF bandwidth at 27.34 dBc relative to the IF. A wideband response of the receiver was measured using a swept RF input whilst the LO is fixed. The IF output of the receiver shows a poor gain flatness of ± 7 dB. The gain flatness can be improved by replacing IF AMP1 with a better performing amplifier. The noise figure of the system was not measured due to non-availability of measurement capability with down-conversion. As the measured LNA noise figure is within the value used for simulation, the system is expected to have an estimated noise figure of 1.74 dB as simulated in the previous chapter. The full system is able to achieve zenith sensitivity in the region of 110 mJy with an antenna noise temperature of 40 K.

Chapter 7

Conclusions and Recommendations

7.1 Conclusions

A receiver system consisting of a wide axially conical corrugated horn and a front-end receiver operating from 14.5 to 20 GHz was designed as concept demonstrator for the MeerKAT. The horn antenna was designed with a single polarization by using a tapered circular to rectangular waveguide transition to standard WR-51 waveguide. Measured results for the wide axially corrugated horn showed a good return loss over the operational band (better than -15 dB), good E- and H-plane beam symmetry and the edge taper is within 2 dB of the targeted -12 dB at the edge of the sub-reflector. The aperture efficiency of the full system with surface accuracy factored was calculated using an offset-Gregorian model in FEKO. An aperture efficiency of 60% was simulated for the antenna.

A front-end downconversion receiver was designed using custom made filters and off-the-shelf connectorized modules. A single mixing stage was used to down-convert the 14.5 to 20 GHz RF input signal to an IF of 4.5 GHz and instantaneous bandwidth of 2.5 GHz. The system was designed for bandpass sampling in the second Nyquist zone at 6 GSPS. The custom designed bandpass filters were implemented for RF image rejection and anti-aliasing using distributed bandpass microstrip filters. The measurement results for the receiver show a maximum gain of 76 dB. The receiver achieved an image rejection of 40 dB and an SFDR of 27.34 dBc. The gain flatness of the receiver was $\pm$7 dB due to a poor performing IF amplifier used in the receiver chain. The measured LNA noise figure was 1.6 dB from 14.5 to 18 GHz. As the system is uncooled, sensitivity of the system will will be dominated by the front-end electronics rather than antenna noise temperature. Sensitivity calculations for the full system were estimated assuming a worst case antenna noise temperature of 40 K. With a 1 second integration time, the receiver can achieve an rms flux sensitivity of 110 mJy.

7.2 Recommendations and Future Work

Primary objectives of this thesis have been met, however, some of the recommendations and future work identified for the system are:

- The antenna design in Chapter 3 was designed for single polarization and a specific edge taper for a maximum aperture efficiency. A dual-polarization can be implemented to the antenna by designing an orthomode transducer (OMT) for the antenna. A full optimization of the gain to noise temperature (A_e/T_{sys}) of the antenna will also be critical in the system as spillover sky noise will be significant at the operational frequency range. A challenge in computing the noise temperature of the antenna system in the electrical size of the antenna at high frequency which would require an extremely fine integration grid of the antenna pattern of the reflector antenna.

- The measurement results of the receiver in Chapter 6 showed a poor gain flatness due to one of the amplifier modules used in the system. The gain flatness of this system can be improved by using better performing IF amplifiers and avoiding mismatch effects due to cascades.

- Full system integration of the receiver was pending implementation of a back-end digital signal processing board at the time of writing this thesis. Verification of the system was planned on the MeerKAT antenna using a drift-scan of a bright radio source. The receiver housing to be used for mounting of the feed antenna and front-end electronics is shown in Appendix D.

References

[1] Square Kilometre Array. https://www.skatelescope.org/. Accessed: 2018-09-25.

[2] A. R. Thompson, J. M. Moran, and G.W. Swenson Jr. *Interferometry and Synthesis in Radio Astronomy*. Springer International Publishing, third edition, 2017.

[3] SKA SA Square Kilometre Array radio telescope (SKA) South Africa. http://www.ska.ac.za//. Accessed: 2018-08-21.

[4] J. C. James and M. R. Scott. *Essential Radio Astronomy (Princeton Series in Modern Observational Astronomy)*. Princeton University Press, 2016.

[5] J. Ruze. Antenna tolerance theory;a review. *Proceedings of the IEEE*, 54(4):633–640, April 1966.

[6] SKAO Science Team. Ska1 observing bands: Scientific context. Technical Report SKA-SCI-SPF-001, SKA, 2015.

[7] FEKO Version 2017.2, Ailtair Hyperworks. https://altairhyperworks.com/product/FEKO.

[8] AWR Design Environment, National Instruments. https://www.awrcorp.com/products/ni-awr-design-environment/visual-system-simulator-software.

[9] L. Tauriq. *New Filter Topology for an Extension of the MeerKAT Radio Astronomy Receiver: 14.5 - 20 GHz Image Reject Filter*. Dissertation, University of Cape Town, 2018.

[10] CST 2018, Dassault Systems. https://www.cst.com/2018.

[11] Committee on Radio Astronomy Frequencies. IAU list of important spectral lines. https://www.craf.eu/iau-list-of-important-spectral-lines/. Accessed: 2018-01-10.

[12] M. Garret. Radio Astronomy Lecture 5. https://www.astron.nl/astrowiki/lib/exe/fetch.php?media=ra_uva:ra_uva_lecture5.pdf, 2015. Accessed: 2019-05-09.

[13] D. L. Simms. Archimedes and the burning mirrors of syracuse. *Technology and Culture*, 18(1):1–24, 1977.

[14] P.S. Kildal. *Foundations of Antenna Engineering: A Unified Approach for Line-of-sight and Multipath*. Artech House, 2015.

[15] C.A. Balanis. *Antenna Theory: Analysis and Design*. John Wiley & Sons, 2005.

[16] T.A. Milligan. *Modern Antenna Design*. Wiley, 2005.

[17] Y. Mizugutch, M. Akagawa, and H. Yokoi. Offset dual reflector antenna. In *1976 Antennas and Propagation Society International Symposium*, volume 14, pages 2–5, Oct 1976.

[18] C. Granet. Designing classical offset cassegrain or gregorian dual-reflector antennas from combinations of prescribed geometric parameters. *IEEE Antennas and Propagation Magazine*, 44(3):114–123, June 2002.

[19] I. P. Theron, R. Lehmensiek, and D. I. L. de Villiers. The design of the meerkat dish optics. In *2012 International Conference on Electromagnetics in Advanced Applications*, pages 539–542, Sep. 2012.

[20] GRASP Student Edition 10.3.0. http://www.ticra.com/products/software/grasp.

[21] P. S. Kildal. Factorization of the feed efficiency of paraboloids and cassegrain antennas. *IEEE Transactions on Antennas and Propagation*, 33(8):903–908, Aug 1985.

[22] P. S. Kildal. Asymptotic transition region theory for edge diffraction. ii. calculation of diffraction losses in multireflector antennas. *IEEE Transactions on Antennas and Propagation*, 38(9):1359–1365, Sep 1990.

[23] D. I. L. de Villiers. Offset dual-reflector antenna system efficiency predictions including subreflector diffraction. *IEEE Antennas and Wireless Propagation Letters*, 10:947–950, 2011.

[24] P. S. Kildal and J. J. Stamnes. Asymptotic transition region theory for edge diffraction. i. tracing transition regions via reflectors. *IEEE Transactions on Antennas and Propagation*, 38(9):1350–1358, Sep 1990.

[25] A.F. Kay. Wide angle horn feed closely spaced to main reflector, September 20 1966. US Patent 3,274,603.

[26] P.J.B. Clarricoats and A.D. Olver. *Corrugated Horns for Microwave Antennas*. Electromagnetics and Radar Series. IET, 1984.

[27] A. Ludwig. The definition of cross polarization. *IEEE Transactions on Antennas and Propagation*, 21(1):116–119, January 1973.

[28] C.A. Balanis. *Advanced Engineering Electromagnetics*. CourseSmart Series. Wiley, 2012.

[29] P.A.G. Soares, P. Pedro, and C.A. Wuensche. High performance corrugated horn antennas for cosmogal satellite. *Procedia Technology*, 17:667 – 673, 2014. Conference on Electronics, Telecommunications and Computers – CETC 2013.

[30] L. WAN-CHUN. *Studies of the Eleven Antenna Feed in Axi-Symmetric Reflector Systems For the Next Generation Radio Telescope*. Masters thesis, Chalmers University of Technology, 2012.

[31] SETI Institute. Allen telescope array. https://www.seti.org/ata. Accessed: 2018-12-05.

[32] G. Engargiola. Non-planar log-periodic antenna feed for integration with a cryogenic microwave amplifier. In *IEEE Antennas and Propagation Society International Symposium (IEEE Cat. No.02CH37313)*, volume 4, pages 140–143 vol.4, June 2002.

[33] W. A. Imbriale, G. Cortes-Medellin, and L. Baker. Update on the ska offset optics design for the u.s. technology development project. In *2011 Aerospace Conference*, pages 1–10, March 2011.

[34] R. Olsson, P. Kildal, and S. Weinreb. The eleven antenna: a compact low-profile decade bandwidth dual polarized feed for reflector antennas. *IEEE Transactions on Antennas and Propagation*, 54(2):368–375, Feb 2006.

[35] J. Yang, X. Chen, N. Wadefalk, and P. Kildal. Design and realization of a linearly polarized eleven feed for 1-10 ghz. *IEEE Antennas and Wireless Propagation Letters*, 8:64–68, 2009.

[36] L. Xiel, B. Du, Y. Wu, Y. Jiaol, and Y. Shi. Design and optimization of a quadruple-ridged flared (qrfh) feed for ska. In *2018 IEEE Asia-Pacific Conference on Antennas and Propagation (APCAP)*, pages 194–197, Aug 2018.

[37] N. Mutonkole. *Study of a Wideband Sinuous Feeed for Reflector Antenna Applications*. Masters thesis, University of Stellenbosch, 2013.

[38] D. I. L. de Villiers. Initial study of a pyramidal sinuous antenna as a feed for the ska reflector system in band-1. In *2017 IEEE International Symposium on Antennas and Propagation USNC/URSI National Radio Science Meeting*, pages 555–556, July 2017.

[39] A. H. Akgiray. *New Technologies Driving Decade-Bandwidth Radio Astronomy: Quad-ridged Flared Horn and Compound-Semiconductor LNAs*. PhD dissertation, California Institute of Technology, 2013.

[40] National Science Foundation. Allen telescope array. https://www.nsf.gov. Accessed: 2018-11-05.

[41] J. Yang, M. Pantaleev, P. Kildal, B. Klein, Y. Karandikar, L. Helldner, N. Wadefalk, and C. Beaudoin. Cryogenic 2–13 ghz eleven feed for reflector antennas in future wideband radio telescopes. *IEEE Transactions on Antennas and Propagation*, 59(6):1918–1934, June 2011.

[42] R. Gawande and R. Bradley. Towards an ultra wideband low noise active sinuous feed for next generation radio telescopes. *IEEE Transactions on Antennas and Propagation*, 59(6):1945–1953, June 2011.

[43] C. Granet and G. L. James. Design of corrugated horns: a primer. *IEEE Antennas and Propagation Magazine*, 47(2):76–84, April 2005.

[44] Altair Connect. https://connect.altair.com/CP/kb-view.html?kb=187200. Accessed: 2018-02-04.

[45] SOLIDWORKS 2017, Dassault Systems. https://www.solidworks.com/.

[46] IEEE standard test procedures for antennas. *ANSI/IEEE Std 149-1979*, 1979.

[47] Analogue Devices. *12-Bit, 10.25 GSPS, JESD204B, RF Analog-to-Digital Converter datasheet*, 2018.

[48] D.M. Pozar. *Microwave Engineering*. Wiley, 2004.

[49] SKAO Science Team. Ska1 level 0 science requirements. Requirements Document SKA-TEL-SKO-0000007, SKA, 2015.

[50] Marki Microwave. *MM1-0626H GaAs MMIC Double Balanced Mixer datasheet*, 2017.

[51] F. Marki and C. Marki. Mixer basics primer: A tutorial for rf and microwave mixers. 2010.

[52] Park Electrochemical Corp. *Mecurywave 9350 datasheet*.

[53] C. E. Shannon. Communication in the presence of noise. *Proceedings of the IRE*, 37(1):10–21, Jan 1949.

[54] P. Bakopoulos, S. Dris, B. Schrenk, I. Lazarou, and H. Avramopoulos. Bandpass sampling in heterodyne receivers for coherent optical access networks. *Optical Society of America*, 20(28), December 2012.

[55] R. G. Vaughan, N. L. Scott, and D. R. White. The theory of bandpass sampling. *IEEE Transactions on Signal Processing*, 39(9):1973–1984, Sep. 1991.

[56] Texas Instruments. *ADC08DJ3200 RF-Sampling Analog-to-Digital Converter (ADC) datasheet*.

[57] P. Purnachandar. Why oversampling when undersampling can do the job. Application Report SLAA594A, Texas Instruments, 2013.

[58] J. G. Proakis and D. K. Manolakis. *Digital Signal Processing (4th Edition)*. Prentice Hall, 2006.

[59] G. Matthaei, L. Young, and E. M. T. Jones. *Microwave filters, impedance- matching networks, and coupling structures*. Artech House, 1980.

[60] ITU. *RECOMMENDATION ITU-R P.372-13 Radio Noise*, 2016.

[61] Low Noise Factory. *LNF-LNR10_30A 10-30 GHz Low Noise Amplifier datasheet*.

[62] Mini-Circuits. *ZX60-5916MA+ Coaxial Amplifier datasheet*.

[63] Mini-Circuits. *ZRON-8G+ Coaxial Amplifier datasheet*.

[64] Keysight Technologies. Noise figure measurement accuracy: The y-factor method. Application note, Keysight Technologies, 2018.

[65] NRAO. The performance of the GBT. http://www.gb.nrao.edu/~rmaddale/GBT/ReceiverPerformance/PlaningObservations.htm. Accessed: 2019-01-25.

[66] G. C. Medellín. Memo 95 antenna noise temperature calculation. Technical Report Memo 95, SKA, 2007.

[67] Mini-Circuits. *Coaxial Cable: 086 KM Model Series datasheet*.

[68] Radio2space. Cassiopea A recorded with SPIDER radio telescope. https://www.radio2space.com/cassiopea-a-recorded-with-spider-radio-telescope/. Accessed: 2019-01-10.

[69] J. Dijk, H. Groothius, and E. Maanders. Some improvements in antenna noise temperature calculation. *IEEE Transactions on Antennas and Propagation*, 18(5):690–692, Sep. 1970.

[70] B. Pietro, P. Federico, M. Stelio, and P. Giuseppe. IRA Technical Report 377/05: Description of a rigorous procedure to evaluate the antenna temperature and its application to BEST-1. Technical report, 2005.

[71] MATLAB 2017, MathWorks. https://www.mathworks.com/products/matlab.html.

Appendix A

Design Curves for Corrugated Horns

A.1 -10 dB half Beamwidth against normalised semi-flare angle

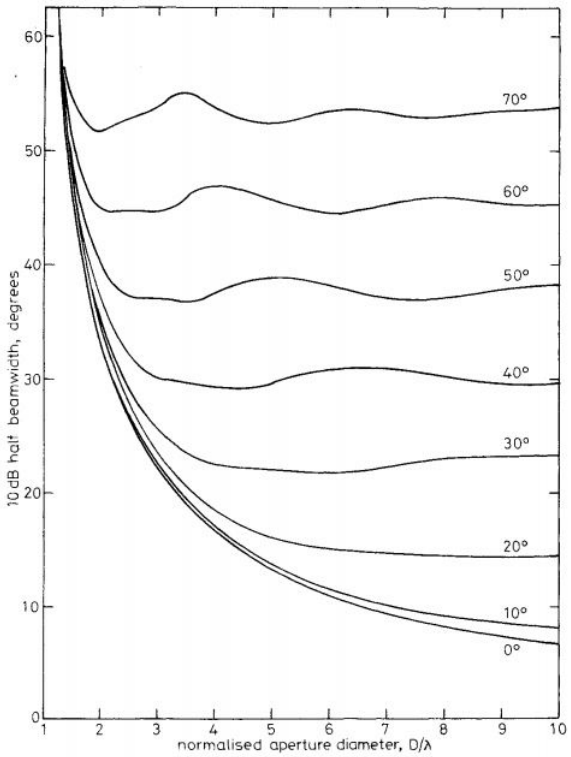

Fig. A.1 -10 dB half beamwidth against normalised aperture diameter for different flare angles.

A.2 Directivity against aperture diameter for different flare angles

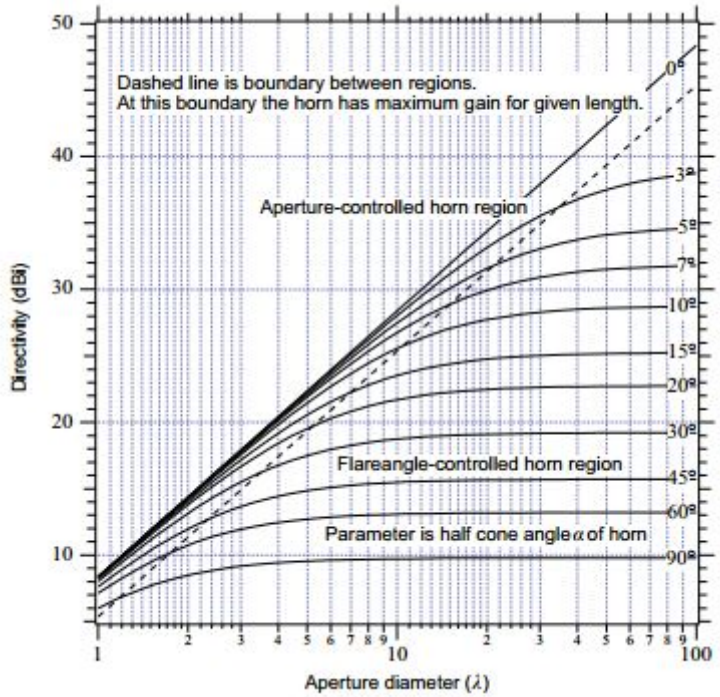

Fig. A.2 Directivity as a function of aperture diameter for different flare angles [14].

Appendix B

Brightness Temperature

B.1 ITU Recommendation for Radio Noise

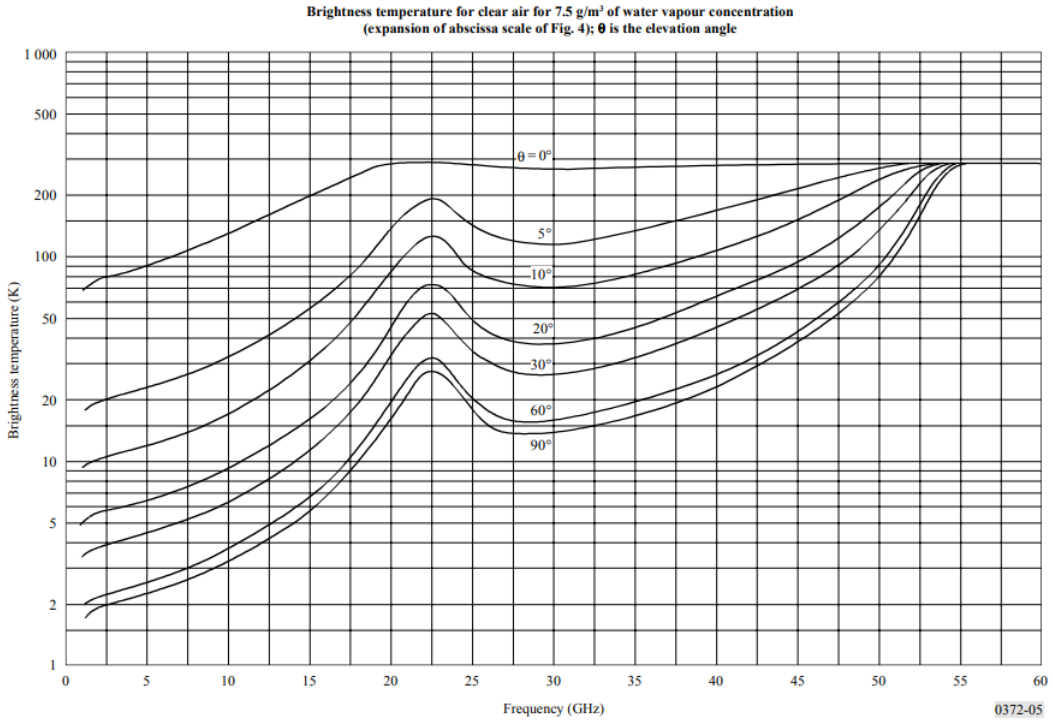

Fig. B.1 Brightness temperature (clear air) for 7.5 g/m3 water vapour concentration [60].

B.2 Flux Density of Some Bright Radio Sources

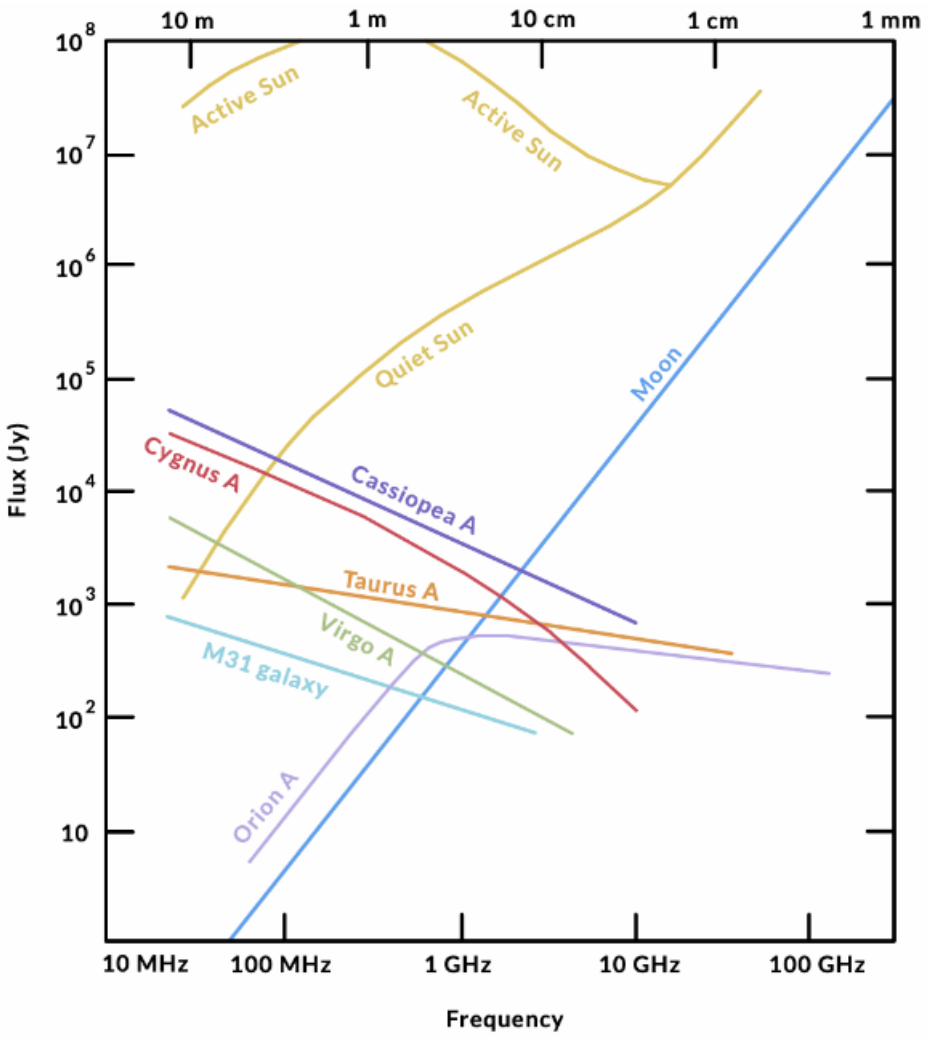

Fig. B.2 Flux density of some common bright radio sources [68].

Appendix C

Antenna Noise Temperature Considerations

The calculation of the antenna noise temperature requires the the knowledge of both the antenna pattern and the noise distribution surrounding the antenna.

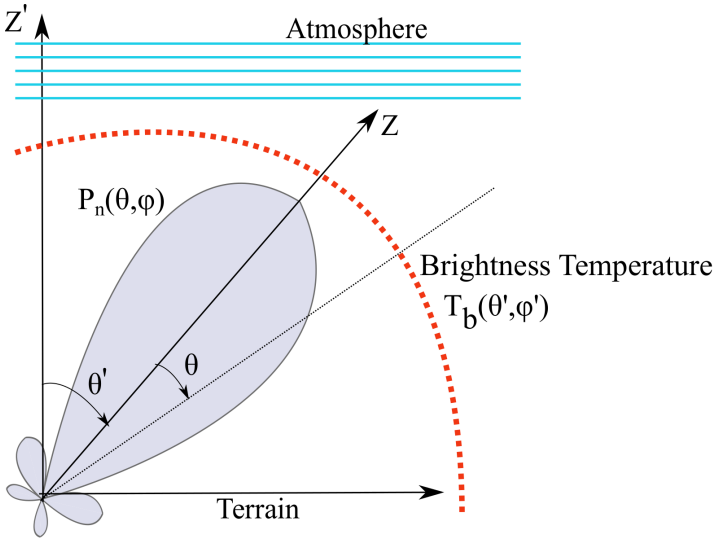

Fig. C.1 Observed scene of antenna radiation pattern.

If Fig. C.1 is considered, the noise temperature seen by the antenna at frequency f is given by [69]:

$$T_a(f;\Theta_0,\Phi_0,\Delta_0) = \frac{\iint_{4\pi} P_n(f;\theta,\phi)\, T_b(f;\theta',\phi') \sin\theta \, d\theta d\phi}{\iint_{4\pi} P_n(f;\theta,\phi) \sin\theta \, d\theta d\phi}, \tag{C.1}$$

where:

$$\begin{aligned}\theta' &= \theta'(\theta,\phi,\Theta_0,\Phi_0,\Delta_0)\\ \phi' &= \phi'(\theta,\phi,\Theta_0,\Phi_0,\Delta_0).\end{aligned} \tag{C.2}$$

$P_n(f;\theta,\phi)$ is total radiation pattern of the antenna referenced to the cartesian coordinates x-y-z and $T_b(v;\theta',\phi')$ is the brightness temperature distribution referenced to the cartesian coordinates x'-y'z'. $(\Theta_0,\Phi_0,\Delta_0)$ are the pointing directions of the antenna as detailed in [69]. Θ_0 is the co-elevation angle, Θ_0 is the azimuth angle of the antenna and Δ_0 is the rotation of the antenna system around its main axis. The angles are defined with respect to the x'-y'-z' coordinate system. For computation of (C.1), the same reference coordinate system needs to be used. From [69], the brightness temperature coordinate system is transformed into that of the antenna using:

$$\begin{aligned}\theta' &= arcos[\sin\Theta_0\sin\theta\sin(\phi+\Delta_0)+\cos\Theta_0 cos\theta]\\ \phi' &= arctan\left[\frac{\sin\Phi_0\sin\theta\sin(\phi+\Delta_0)+\cos\Phi_0\cos\Theta_0\sin\theta\sin(\phi+\Delta_0)-cos\Phi_0\sin\Theta_0\cos\theta}{cos\Phi_0\sin\theta\cos(\phi+\Delta_0)-\sin\Phi_0\cos\Theta_0\sin\theta\sin(\phi+\Delta_0)+\sin\Phi_0\sin\Theta_0\cos\theta}\right].\end{aligned} \tag{C.3}$$

Using (C.3), θ',ϕ' is found for every θ,ϕ value. The brightness temperature distribution is assumed to be rotationally symmetric therefore ϕ' is not computed [70], the brightness temperature is simply represented as $T_b(f;\theta')$.

C.0.1 Brightness Temperature Calculation

The brightness temperature T_b is separated into the sky contribution T_b^{sky} $(0^\circ \le \theta' \le 90^\circ)$ and the ground contribution T_b^{gnd} $(90^\circ < \theta' \le 180^\circ)$. For ground based observations, the sky brightness temperature is calculated using [66]:

$$T_b^{sky}(f;\theta') = T_{bo}(f)e^{-\tau_{f,\theta'}(0,h_a)} + \int_0^{h_a}\frac{k_a(f;z')T_{atm}(z')e^{-\tau_{f,\theta'}(0,z')}}{\sqrt{1-(sin\theta'/(1+(z'/r_e)))^2}}dz', \tag{C.4}$$

where $T_{atm}(z')$ is the physical temperature of the atmosphere and $K_a(f;z')$ is the absorption coefficient of the atmosphere at a height above the ground z' which includes water vapour and oxygen coefficients:

$$k_a(f;z') = k_{H_2O}(v;z') + k_{O_2}(f;z'), \tag{C.5}$$

T_{bo} is the background brightness temperature due to cosmic emission from cosmic microwave background (CMB) T_{CMB} and galactic emission T_{go}:

$$T_{bo}(f) = T_{CMB} + T_{go}(f_0/f)^{\beta}, \tag{C.6}$$

where $T_{CMB} = 2.73$, $T_{go} = 20$K, $f_0 = 0.408$ GHz and spectral index $\beta = 2.75$ are average values that are suggested for an estimation of galactic noise contribution for $f \geq 0.01$ GHz [66]. $\tau_{f,\theta'}$ is the zenith opacity of the atmosphere calculated as:

$$\tau_{f,\theta'}(0,h_a) = \int_0^{h_a} \frac{k_a(f;z')}{\sqrt{1-(sin\theta'/(1+(z'/r_e)))^2}} dz', \tag{C.7}$$

r_e is the radius of the earth and h_a is the height of the atmosphere which is proposed to be 100 Km. Tabulated values of the sky temperature from the numerical integration of (C.4) were presented in [70]. To speed up calculations, a MATLAB [71] script was used to interpolate for frequency points and zenith angles. The tabulated values for the frequency range of interest (14.5 to 20 GHz) are shown in Table C.0.1. Values for frequencies between 14 and 22 GHz using MATLAB's polynomial curve fitting function. The interpolated and tabulated values used for the interpolation are shown in Fig. C.2. An interpolation of elevation angle points was then obtained. Linear interpolation is used for the region where the elevation angle $\theta' \leq 60^{\circ}$ and an exponential function is used for the region $60^{\circ} \leq \theta' \leq 90^{\circ}$. The interpolated values are shown in Fig. C.3. Using the interpolation functions, given any elevation angle $\leq 90^{\circ}$ and frequency from 14 to 22 GHz, the sky temperature can be estimated.

Table C.1 Tabulated sky noise from [70].

Frequency [GHz]	$T_b^{sky}(0^{\circ})$ [K] [K]	$T_b^{sky}(60^{\circ})$ [K]	$T_b^{sky}(85^{\circ})$ [K]	$T_b^{sky}(90^{\circ})$ [K]
14	7.17	11.5	47.3	179
16	8.71	14.5	61.5	217
18	11.8	20.5	87.6	259
20	19.2	34.6	1.39	288
21	25.6	46.6	174	293
22	31.4	57	197	294

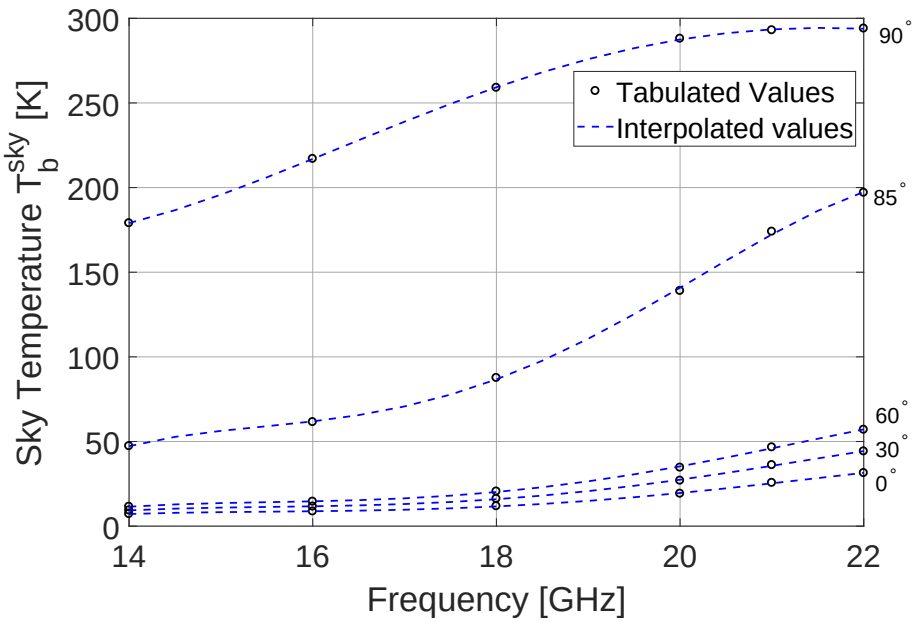

Fig. C.2 Interpolation of tabulated sky temperature over frequency. Values are plotted for different values of elevation angles shown on the right.

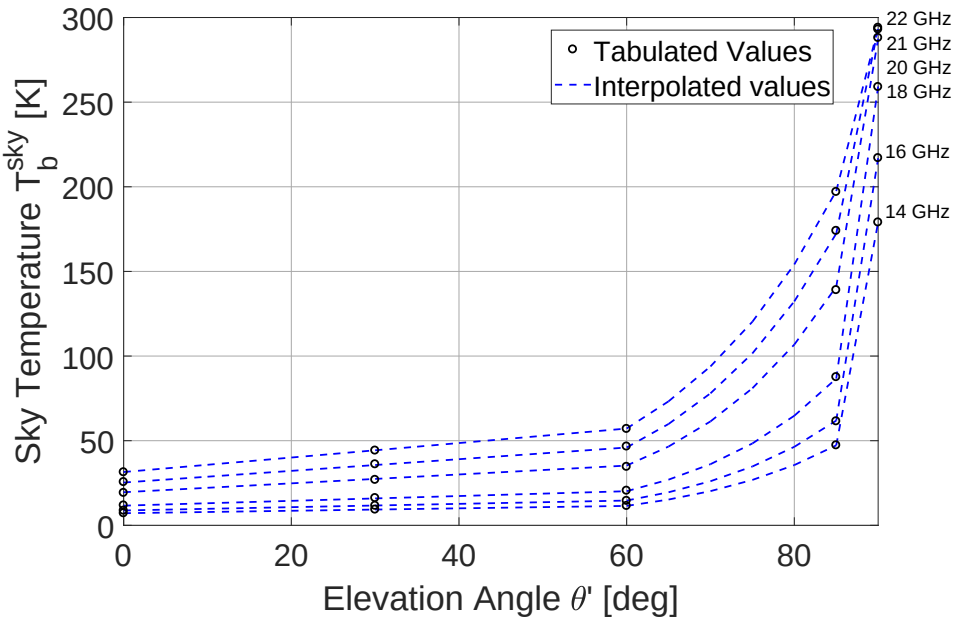

Fig. C.3 Interpolation of tabulated sky temperature over elevation angle. Values are plotted for different values of frequency shown on the right.

C.0.2 Ground Region Contribution

The emission and scattering from the ground should be included for more accurate noise calculations. The simplified formula [66] was adopted for this work where ground emission and scattering is included into (C.1). First, polarization dependant reflection coefficient of the ground air interface for vertical and horizontal polarization is calculated as:

$$\begin{aligned} \Gamma_{\parallel}(\theta_1) &= \left| \frac{\cos\theta_1 - \sqrt{\varepsilon_2 - sin^2\theta_1}}{\cos\theta_1 + \sqrt{\varepsilon_2 - sin^2\theta_1}} \right|^2 \\ \Gamma_{\perp}(\theta_1) &= \left| \frac{\varepsilon_2\cos\theta_1 - \sqrt{\varepsilon_2 - sin^2\theta_1}}{\varepsilon_2\cos\theta_1 + \sqrt{\varepsilon_2 - sin^2\theta_1}} \right|^2, \end{aligned} \tag{C.8}$$

ε_2 is the relative permittivity of the ground (3.5 for dry land) and $\theta_1 = \pi - \theta'$. The antenna pattern and sky temperature product in (C.1) is then expanded as

$$P_n(f;\theta,\phi)T_b(f;\theta',\phi) = \begin{cases} P_n(f;\theta,\phi)T_b^{sky}(f;\theta') & 0^\circ \le \theta' \le 90^\circ \\ P_n(f;\theta,\phi)[(1-\overline{\Gamma}(\theta_1))T_{gnd} + \overline{\Gamma}(\theta_1)T_b^{sky}(\theta_1)] & 90^\circ < \theta' \le 180^\circ, \end{cases} \tag{C.9}$$

where T_{gnd} is the the ground temperature (270 K) and $\overline{\Gamma}(\theta_1)$ is the average reflection coefficient of the ground:

$$\overline{\Gamma}(\theta_1) = \frac{\Gamma_{\parallel}(\theta_1) + \Gamma_{\perp}(\theta_1)}{2} \tag{C.10}$$

The antenna noise temperature can then be calculated using the numerical integration of (C.1). The calculation of the antenna noise temperature will require an enormous amount of computing resource as a very fine integration grid of the antenna pattern needs to be used due to the high directivity at this frequency range.

Appendix D

Receiver Housing Photograph

Fig. D.1 Receiver housing to be mounted on MeerKAT during system testing. Housing designed by Luyanda Boyana (SARAO).